



Dissertation

Fabrício Borges de Oliveira

Multi-Material Acceptance Testing for Computed Tomography-Based Coordinate Measurement Systems



ISSN 0179-0609
ISBN 978-3-95606-562-0

Physikalisch-Technische Bundesanstalt

Fertigungsmesstechnik

PTB-F-66

Braunschweig, Januar 2021

Fabrício Borges de Oliveira

Multi-Material Acceptance Testing for Computed Tomography-Based Coordinate Measurement Systems

Herausgeber:

Physikalisch-Technische Bundesanstalt

ISNI: 0000 0001 2186 1887

Presse und Öffentlichkeitsarbeit

Bundesallee 100

38116 Braunschweig

Telefon: (05 31) 592-93 21

Telefax: (05 31) 592-92 92

www.ptb.de

Multi-Material Acceptance Testing for Computed Tomography-Based Coordinate Measurement Systems

Von der Fakultät für Maschinenbau
der Technischen Universität Carolo-Wilhelmina zu Braunschweig

zur Erlangung der Würde

eines Doktor-Ingenieurs (Dr.-Ing.)

genehmigte Dissertation

Von: Fabrício Borges de Oliveira

aus: Lages, Brasilien

eingereicht am: 06.02.2020

mündliche Prüfung am: 27.08.2020

Gutachter: Prof. Dr.-Ing. Rainer Tutsch

Prof. Dr.-Ing. Jochen Hiller

Dr.-Ing. habil. Ulrich Neuschaefer-Rube

Abstract

X-ray computed tomography (CT) is regarded by many as the third revolution in coordinate metrology. This may be explained by the holistic approach of CT, which scans workpieces completely and allows a great variety of measurements. With a single scan, it is possible to make for example, dimensional, form or wall thickness measurements, or even to compare the entire workpiece with e.g. its nominal geometry, and more. The same holistic approach also greatly facilitates the quality control of multi-material (MuMat) objects, even in their assembled state.

However, the lack of international standards describing specifications and technical guidelines for the application of CT as a coordinate measurement system (CMS) hinders the trust in this X-ray-based technology. As yet, no published international standard for CT as a CMS exists, but such a standard is already under development in the international standardisation committee ISO TC213 WG10 “coordinate measuring machines”. This under-development standard will only cover mono-material measurements, although the demand for a systematic and traceable approach for evaluating the performance of CT systems while measuring multi-material workpieces is growing.

Therefore, this thesis has as its primary objective the development of an acceptance test to evaluate the performance of CT-based CMSs for multi-material measurements. Existing principles and concepts from the ISO 10360 series of international standards were applied or adapted to the proposed multi-material test. New test principles and concepts, considering the specifics of multi-material measurements with CT, were developed as well.

A widely accepted concept for the evaluation of the system performance (based on the ISO 10360) is the assessment of the probing error (P) and length measurement error (E). These systems characteristics are assessed based on test measurements carried out with appropriate reference standards.

Thus, to evaluate the multi-material performance of CT systems based on P - and E -tests, and to verify the developed proposal, novel multi-material spheres and hole cube standards were designed, manufactured, calibrated and measured with CT at the *Physikalisch-Technische Bundesanstalt* (PTB). In addition, CT simulations were carried out as well. In total twelve standards featuring different multi-material combinations were created and tested during this thesis. Several experimental investigations for different multi-material parameters were carried out on the developed multi-material standards.

The results evidenced the multi-material influence on both P - and E -test measurements. The proposed multi-material acceptance test proved to be a suitable approach for the performance verification of CT-based CMS for multi-material measurements.

Kurzfassung

Die Röntgen-Computertomographie (CT) wird oft als die dritte Revolution in der Koordinatenmesstechnik bezeichnet. Dies erklärt sich dadurch, dass CT das gesamte Bauteil erfasst und eine Vielzahl an Messmöglichkeiten eröffnet wird. Mit nur einem Scan können beispielsweise Messungen von Dimensionen, Form oder Wanddicke durchgeführt werden und die gesamte Geometrie, die von CT erfasst wurde, kann mit z.B. der Nominalgeometrie des Bauteils verglichen werden. Dieser holistische Ansatz der CT erleichtert die Qualitätskontrolle insbesondere von montierten Multimaterial-Objekten erheblich.

Allerdings verhindert das Fehlen von internationalen Normen, die die Spezifikationen und technische Richtlinien für die Anwendung von CT als Koordinatenmesssystem (KMS) beschreiben, das Vertrauen in diese röntgenbasierte Messtechnologie. Bis heute wurde keine internationale Norm für die Prüfung von CT als KMS veröffentlicht. Jedoch bereitet der internationale Normenausschuss ISO TC213 WG10 „Coordinate measuring machines“ eine solche Norm vor. Diese Norm wird allerdings nur Monomaterialmessungen umfassen, obwohl ein großer Bedarf seitens der Industrie, CT-Anwendern und Herstellern an einer systematischen und rückführbaren Methode für die Bestimmung der Leistungsfähigkeit von CT -basierten KMS auch für Multimaterialmessungen besteht.

Darum verfolgt diese Dissertation das Hauptziel, eine Annahmeprüfung zu entwickeln, die diese Forderung erfüllt. Dafür wurden bekannte Prinzipien und Konzepte der internationalen Normenreihe ISO 10360 in dieser Multimaterialprüfung benutzt und, wo es erforderlich war, an die spezifischen Anforderungen angepasst.

Ein allgemein anerkanntes, auch hier angewandtes Konzept für die Evaluierung der Systemleistungsfähigkeit (nach ISO 10360) ist die Bewertung der Antastabweichung (P) und der Längenmessabweichung (E). Diese Leistungsmerkmale werden auf Basis von Testmessungen geeigneter Prüfkörper bewertet. Dafür wurden an der Physikalisch-Technischen Bundesanstalt (PTB) neuartige Multimaterialkugeln und Multimaterialwürfel konstruiert, kalibriert und mit CT gemessen. Dadurch konnte die Leistungsfähigkeit von CT für Multimaterialmessungen basierend auf P - und E -Prüfungen bestimmt werden. Darüber hinaus wurden Simulationen von CT-Messungen der neuartigen Prüfkörperdesigns durchgeführt, um die realen Messergebnisse zu unterstützen. Insgesamt wurden zwölf Prüfkörper in verschiedenen Multimaterialkombinationen gefertigt, die im Zuge dieser Dissertation geprüft wurden.

Die Ergebnisse weisen einen Multimaterialeinfluss auf P - und E -Messungen nach. Die hier vorgestellte Multimaterial-Annahmeprüfung bewährte sich als geeigneter Ansatz für die Evaluierung der Leistungsfähigkeit von CT als KMS für Multimaterialmessungen.

Contents

Chapter 1: Introduction	1
1.1 Motivation.....	1
1.2 Objectives	3
1.3 Structure of the thesis	4
Chapter 2: CT measurements, relevant influencing factors and performance verification	5
2.1 Workflow of dimensional measurements with CT-based CMS.....	5
2.1.1 Data acquisition	6
2.1.2 Data processing	12
2.2 Influencing factors and effects of multi-material measurements by CT	18
2.2.1 Relevant influencing factors	19
2.2.2 Relevant effects.....	25
2.3 Performance verification of CT-based CMS	33
2.3.1 Acceptance and reverification testing for (CT-based) CMS	34
2.3.2 Decision-making and attributed uncertainty	41
2.4 Summary and conclusions of the chapter	42
Chapter 3: Proposal for a multi-material acceptance test for X-ray CT systems	45
3.1 Multi-material acceptance test requirements.....	45
3.2 Proposal for a multi-material acceptance test.....	47
3.2.1 General multi-material acceptance testing concepts	47
3.2.2 Specification requirements related to multi-material measurements	51
3.2.3 Multi-material probing error test.....	55
3.2.4 Multi-material length measurement error test.....	61
3.3 Verification concept	67
3.3.1 Requirements of the verification concept.....	67
3.3.2 Implementation of the multi-material <i>P</i> -test.....	69
3.3.3 Implementation of a multi-material <i>E</i> -test.....	78
3.3.4 Experimental application of the multi-material acceptance test.....	88
3.4 Summary and conclusion of the chapter.....	101
Chapter 4: Results	103
4.1 Results of multi-material sphere measurements (<i>P</i> -test)	103
4.1.1 Results of experiment <i>P0</i> : Local multi-material performance of the CT-based CMS	103
4.1.2 Results of experiment <i>P1</i> : Necessity of the multi-material <i>P</i> -test	105

4.1.3 Results of experiment <i>P2</i> : Beam hardening influence on the multi-material <i>P</i> -test.....	106
4.1.4 Results of experiment <i>P3</i> : Simulation of the more difficult multi-material combination for the <i>P</i> -test	108
4.2 Results of multi-material <i>E</i> -test measurements	110
4.2.1 Results of the experiment <i>E0</i> : Multi-material influence on the length measurement error test.....	110
4.2.2 Results of experiment <i>E1</i> : Necessity of the multi-material length measurement error test.....	118
4.2.3 Results of experiment <i>E2</i> : Sensibility verification of the test for the multi-material effects	121
4.2.4 Results of experiment <i>E3</i> : Simulation of the more difficult multi-material combination for the <i>E</i> -test.....	123
4.3 Summary of the chapter	126
Chapter 5: Conclusions, discussions and outlook.....	129
5.1 Summary and conclusions.....	129
5.2 Discussions and outlook.....	132
5.2.1 Improvements related to the multi-material standards	132
5.2.2 Potential improvements related to the multi-material test proposal	133
5.2.3 Potential improvements related to multi-material effects	133
5.2.4 Future standardisation developments	134
5.2.5 Future technological developments.....	134
List of figures	i
List of tables.....	v
References	vii
Acronyms	xvii
List of symbols	xix
Acknowledgements.....	xxi

Chapter 1: Introduction

1.1 Motivation

The fundamental tools for X-ray computed tomography (CT) — i.e. X-ray radiation and mathematical algorithm for image reconstruction — were published in 1895 by Wilhelm Röntgen [1]; and in 1917 by Johann Radon [2]. In spite of this, the first CT systems for medical imaging were only developed in the late 1960s. Less than ten years later, the first non-medical applications of CT already started to emerge in Germany [3]. In the second half of the 1980s, the concept of CT was widened to be used as a tool for dimensional control. However, back then, there were no dedicated CT system to metrology applications. Dedicated CT systems for metrology first started to appear mid-2000s [4].

Computed tomography as coordinate measurement system (CMS) represents a revolutionary advancement for industry and dimensional metrology. Together with the introduction of the tactile- and optical-based CMS in the 1970's and 1980's, CT as CMS is considered to be among the three most important developments in coordinate metrology [5]. This revolutionary status can be explained with the ability of this X-ray-based technology to acquire the entire three-dimensional (3D) representation — of inner and outer structures — of measured objects. On top of this, diverse measurement tasks (e.g. actual/nominal comparison, dimensional, wall thickness measurements, etc.) and non-destructive testing (e.g. defect analysis) are enabled by CT in a reasonable measurement time, due to its holistic approach [4]. Also, the measurement of assemblies and multi-material (MuMat) objects, even in their mounted state, was greatly facilitated by this non-destructive measurement technique. While the conventional CMS technologies are limited by accessible features, for CT the only limitation is the density of the workpiece to be measured.

However, the use of CT in the field of dimensional metrology creates new challenges rarely encountered in conventional coordinate metrology (i.e. in tactile and optical CMSs). For instance, the data acquisition by CT occurs as a result of physical interactions between X-ray radiation and the object material.

Since CT started to be applied as a CMS to a larger extent, the technology is under continuous development, aimed at improving its measurement capabilities, in order to enable more precise and reliable measurements. Improvement of the stability of the X-ray sources,

more precise manipulator systems, fast CT scans, optimisation of scanning parameters as well as development of correction methods are among the topics which have been studied by researchers and manufacturers.

Despite many enhancements, CT has not yet reached the same level of confidence as the conventional CMS technologies. Traceability, for example, is still an important unsolved issue for CT. This is due to the interplay of a large number of factors influencing a measurement, which complicates the task of uncertainty evaluation. Another important obstacle to a broader acceptance of CT as an established CMS, is the absence of international standards and technical guidelines providing specifications for the application of CT specifically as a measurement technology, since standardisation serves to create trust in a measurement technology.

International standards for CT (e.g. ISO 15708) and national guidelines (e.g. ASTM E 1451, ASTM E 1672, ASTM E 1665, etc.) focused on non-destructive testing (NDT) applications, have been established to guide users to perform workpiece examination, selection of CT system, evaluate the system performance, etc. Because of the different requirements of characteristics to be analysed for metrology and NDT applications, the existing abovementioned standards and guidelines are not directly applicable to metrology applications. For example, the location of interface/surface between material and air is of vital importance for metrology applications, while often of less importance for NDT applications.

Thus, in 2009, the Association of German Engineers (VDI/VDE) published the first national guideline dedicated to the application of CT as a CMS (VDI/VDE 2630 Blatt 1.1 [6]). At the international level, standardisation began in 2010, where the concepts of acceptance and reverification tests — being part of the scope of the ISO 10360 series of standards for testing CMS — are now being adapted and extended to CT-based CMS [7]. Although these activities represent significant progress towards a wider acceptance of CT as a CMS, up to date these on-going activities are not yet published. Furthermore, they are limited to the task of mono-material (MoMat) measurements and do not consider multi-material measurements.

The number of multi-material objects encountered in industry is ever increasing, thanks in part to the drive for weight and cost reductions and improved mechanical properties. The need for quality control with tight geometrical tolerances for such complex multi-material objects is, in some cases, crucial. For example, with safety-critical parts such as car door latch system or electrical connector, where a failure could result in a life-threatening situation. From an economic perspective, quality assurance also plays an important role, by reducing costs of losses in the quality control chain of products and/or processes [8,9].

The quality control of complex multi-material objects could, in principle, be carried out by CT-based CMS measurements [4,10]. However, a lack of knowledge regarding the metrological behaviour of CT when performing complex multi-material measurements, hampers the wider acceptance of CT for quality control of multi-material objects.

Current research into dimensional multi-material measurements is (still) limited, even as the demand in industry is growing. Furthermore, of yet the topic is still outside the scope of standardisation developments, which implies further reliability issues.

The concepts of acceptance and reverification testing offer a systematic approach to check the performance and stability of CMSs. Such tests can verify the entire performance of the CMS, be it during the initial purchase of the system or in regular time intervals. The concepts enable systematic checking and record-keeping of the CMS performance over time at limited costs.

These advantages make acceptance and reverification tests for CT very attractive from both the technical and economic perspectives. Therefore, industry, CT users and manufacturers have shown great interest in a traceable and systematic way to verify the performance of CT-based CMS for the case of multi-material measurements.

This thesis suggests extending and adapting the principles of acceptance and reverification tests to multi-material measurements using CT-based CMS. The aim is to achieve greater acceptance of CT for the quality control of multi-material objects, and to answer research questions such as:

- i. Are there relevant multi-material effects influencing dimensional and geometrical measurements by CT?
- ii. Are there systematic approaches for the performance evaluation of CT-based CMS for multi-material measurements?
- iii. Is the proposed test suitable for evaluating the performance verification of CT-based CMSs for multi-material measurements?
- iv. Should standardisation bodies consider the multi-material-induced effects in the further development of standards for CT-based CMS?

These are the starting points for the objectives of this thesis.

1.2 Objectives

This thesis has as its main objective to create an acceptance test for testing CT-based CMSs for the task of multi-material measurements, aiming to:

- Integrate the existing knowledge to better understand the influence of the multi-material effects on dimensional CT measurements;
- Produce evidence of relevant multi-material effects on the measurements;
- Propose a traceable and systematic method of performance verification for CT-based CMSs applicable to multi-material measurements;
- Encourage standardisation bodies to consider the effects observed, if applicable.

1.3 Structure of the thesis

The proposed approach of a multi-material acceptance testing for dimensional computed tomography is presented as follows:

The complete workflow of dimensional measurements with CT — from the acquisition of X-ray images at different angular positions of the workpiece to the evaluation of a quantity — is presented in Chapter 2. Still in Chapter 2, each process occurring throughout the measurement chain is explained in detail. Additionally, beam hardening, scattering effects and their influence as well as the multi-material influence on the dimensional measurement by CT are presented. The basic principles of acceptance testing are presented at the end of Chapter 2. The concepts of the length measurement error test and probing error test are presented, as well as concepts of decision-making based on the attributed test value uncertainty.

The proposal for the multi-material acceptance testing is presented in the Chapter 3. This chapter is divided in three main topics: (3.1) test requirements; (3.2) multi-material acceptance testing and (3.3) verification concepts. In (3.1) the general design criteria for the new test, based on metrological, industrial and economic aspects are presented. The test requirements are the starting point of the creation of the multi-material acceptance test proposal. In (3.2) existing concepts are applied or adapted to the multi-material test proposal. Also, novel test concepts, considering the specifics of multi-material CT measurements are created. The main objective of (3.3) is to verify if the multi-material test proposal developed in (3.2) fulfils the test requirements presented in (3.1). To reach this goal, the test proposal is implemented and tested based on several experiments, where multi-material reference standards are designed, manufactured, calibrated and measured with CT. In addition, simulation-based studies are also carried out to support the real measurements. Different multi-material parameters (e.g. to evidence the necessity of the multi-material test, beam hardening influence on the multi-material measurements, etc.) were experimentally tested in this thesis. The results of these experimental investigations are presented and discussed in Chapter 4.

Finally, a summary of the whole thesis, conclusion and outlook is presented in Chapter 5.

Chapter 2: CT measurements, relevant influencing factors and performance verification

The rapid growth of CT as a coordinate measurement technology led to changes in the data acquisition and data analysis workflow of CT measurements, when compared e.g. with the workflow used in NDT applications. Therefore, a detailed description of the complete workflow of CT measurements — from the data acquisition to the evaluation of a **dimensional measurement** — is given in § 2.1.

The complex interactions between radiation and matter in a multi-material CT measurement result in new effects and/or the combination of several effects. To integrate the existing knowledge about CT for multi-material measurements and to get a better understanding of the impact of multi-materials on CT measurements, a detailed description of **material-related effects** is provided in § 2.2.

Existing acceptance and reverification tests offer a systematic approach to verify the performance of coordinate measurement systems. They are widely accepted and usually described in international standards or national guidelines. These normative documents are to guide CMS users and manufacturers to specify, perform tests, evaluate and interpret the test results. The principles of **acceptance and reverification testing** are presented in § 2.3, as they serve as a basis for the development of the multi-material acceptance testing proposed in this work.

2.1 Workflow of dimensional measurements with CT-based CMS

The basic principle of CT measurements relies on the X-ray attenuation resulting from the interaction between radiation and matter. The attenuation information is recorded by an X-ray detector. After the scan, the data is presented as a three-dimensional (3D) matrix. This matrix is obtained from the reconstruction of a set of two-dimensional (2D) X-ray images. These 2D X-ray images, also called projections or radiographies, are acquired at different angular positions of the measurement workpiece. Each element of the 3D matrix, also called voxel matrix¹, represents the local X-ray attenuation of the workpiece material expressed in grey levels. Dimensional evaluations, e.g. length, form error measurements, nominal/actual

¹ Voxel is an acronym of volumetric pixel

comparisons, are carried out on a virtual surface of the CT dataset. This virtual object surface is estimated by specialised algorithms based on the grey levels of the dataset.

A typical CT measurement consists of several non-trivial steps, see Fig. 2.1, each having a significant impact on the measurement result. Here, the workflow of CT measurements is divided into steps carried out by the CT hardware (data acquisition) and the computer-aided steps of data processing.

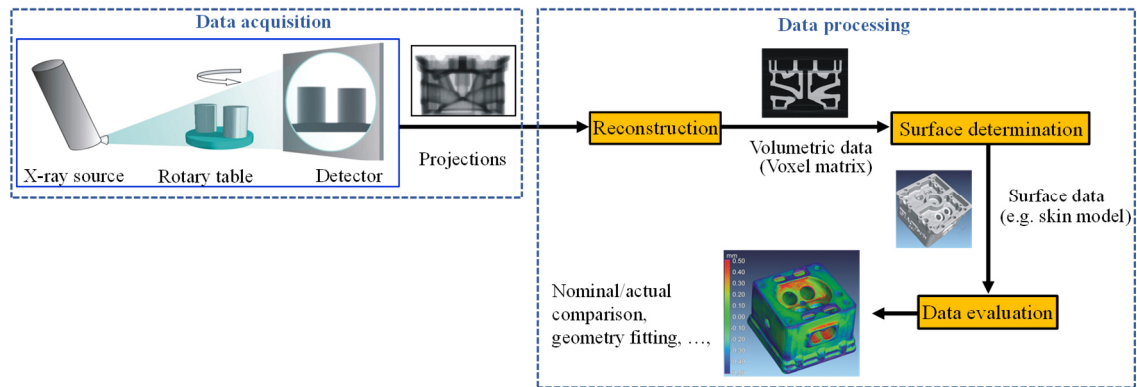


Fig. 2.1. Typical workflow of a CT measurement (source: [11]).

2.1.1 Data acquisition

Essentially, the CT data acquisition consists of acquiring several X-ray radiographies at different angular positions of the measurement workpiece. Although this is only the first step and represents a small part of the workflow, see Fig. 2.1, it has great impact on the measurement. Deviations from the expected information — e.g. a change of the X-ray spectrum caused by the workpiece material — present in the data acquisition phase will be, to a large extent, transferred to the reconstructed volume and consequently to the measurement result. The four fundamental processes and components part of the CT data acquisition process — i.e. system geometry/manipulation system, X-ray generation, X-ray - matter interaction and X-ray detection — are described following.

System geometry / Manipulation system

For the acquisition of several X-ray images from different orientations of the workpiece, CT-based CMSs are commonly equipped with high precision manipulator systems, cone-beam X-ray tubes and flat panel detectors. These components are often assembled inside of a temperature-controlled and an X-ray shielded cabin, lined with e.g. lead. The manipulator system typically features one rotary table and three linear translation stages — for the rotation and translation of the workpiece in the CT machine. They are constructed with mechanically stable materials and high precision mechanical guides, mounted in a stable metallic frame or on a high-quality granite base equipped with ball or air bearings.

For cone-beam CT-based CMSs, a circular trajectory is normally used, where during the scan, the rotary table rotates the workpiece while the translational stages remain stationary. The rotational movement is carried out with well-known angular increments and well-known static relative position between rotary axis, X-ray source and detector, see Fig. 2.2. Special scanning trajectories are becoming popular, as they may deliver better datasets than scans using standard circular trajectory. For example, a helical scanning trajectory delivers reconstructed volumes free from the so-called Feldkamp artefacts, an image artefact caused by mathematical approximations made in the standard reconstruction algorithm for cone-beam systems with circular trajectory [12,13]. However, the demand for requirements of high mechanical precision and the increased effort of determining the geometric parameters at every position of the scan, limits a broader use of these types of scanning trajectories. Considering that, the rotary and linear translational stages move simultaneously during the scan. Besides this, specialised algorithms are necessary for the data reconstruction of scans with such special scanning trajectories.

Knowledge of the geometrical relations between the CT components — i.e. source-rotary axis distance (SRD), source-detector distance (SDD) and the relative orientations — is of major importance to dimensional measurements with cone-beam systems. The incorrect consideration of the geometrical relations causes measurement errors and distortions in the reconstructed volume [14,15].

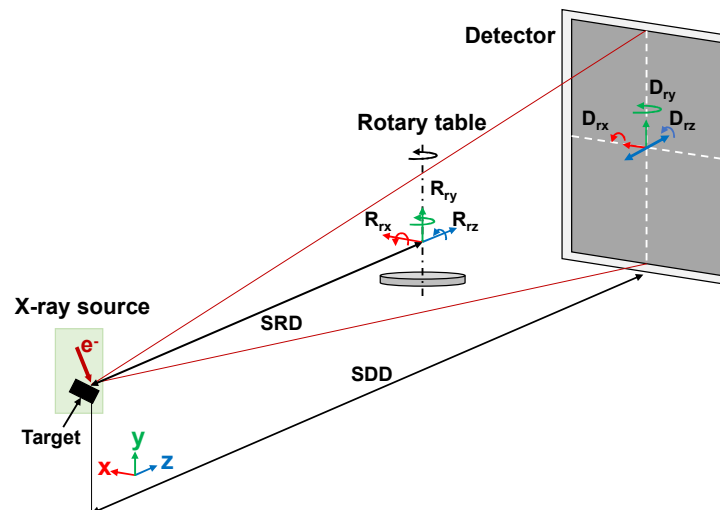


Fig. 2.2. Cone-beam CT system geometry with flat panel detector. Also shown are the distances source-detector (SDD) and source-rotary axis (SRD) as well as detector and rotary axis orientation.

X-ray generation

Comparable to visible light, microwaves, radio-waves and THz waves, X-ray radiation is of electromagnetic nature, with wavelengths ranging from few picometres to few nanometres.

In X-ray tubes commonly found in the CT-based CMSs, the radiation is created by the abrupt deceleration of high-speed electrons hitting and interacting with a solid material. The solid material is called anode or target. Materials with high atomic number and a high melting point, e.g. tungsten, molybdenum or copper, are preferred target materials. The generation of X-ray radiation by this phenomenon is widely known under its German term “*Bremsstrahlung*”.

Electrons — from an electric current — flowing in the filament or cathode of an X-ray tube are ejected from the cathode due to a combination of thermal effects and the large potential difference between cathode and anode. The ejected electrons are accelerated and focused — by electric and magnetic fields created by coils in the X-ray tube — towards a point on the target surface, hitting it with high speed. Due to physical limitations, e.g. the melting point of the target material, the focal point is spread to a small region of the anode. This small region is commonly called focal spot. When striking the anode, the high-speed electrons collide with the atoms of the target material and different types of interactions occur. Since most of the interactions involve low energy level transfers, causing the ionisation of the atoms, almost all of these collisions do not produce X-rays (typically for X-ray tubes, 99% of the input energy is converted into heat) [12]. However, there are three types of collisions which lead to creation of X-ray radiation:

(a) When high-speed electrons travel close to the nucleus of an atom, they are decelerated by the attraction between the nucleus and the electrons of the atom. This sudden deceleration of the high-speed electrons produces X-ray radiation, the so-called *Bremsstrahlung*, see Fig. 2.3-a.

(b) When the high-speed electrons hit one of the inner shell electrons of the target atom. The atomic electron is ejected and liberates an inner shell of the atom. When an atomic electron from an outer shell fills the vacant inner shell, X-ray radiation called characteristic radiation is produced, see Fig. 2.3-b.

(c) When a high-speed electron collides directly with the atomic nucleus, its kinematic energy is converted into *Bremsstrahlung*, see Fig. 2.3-c.

As a high-speed electron penetrates the anode material, it suffers multiple decelerations as it interacts with several atoms of the target material, therefore, a continuous distribution of energies — i.e. an X-ray polychromatic spectrum — is obtained by *Bremsstrahlung*, see bottom of Fig. 2.3.

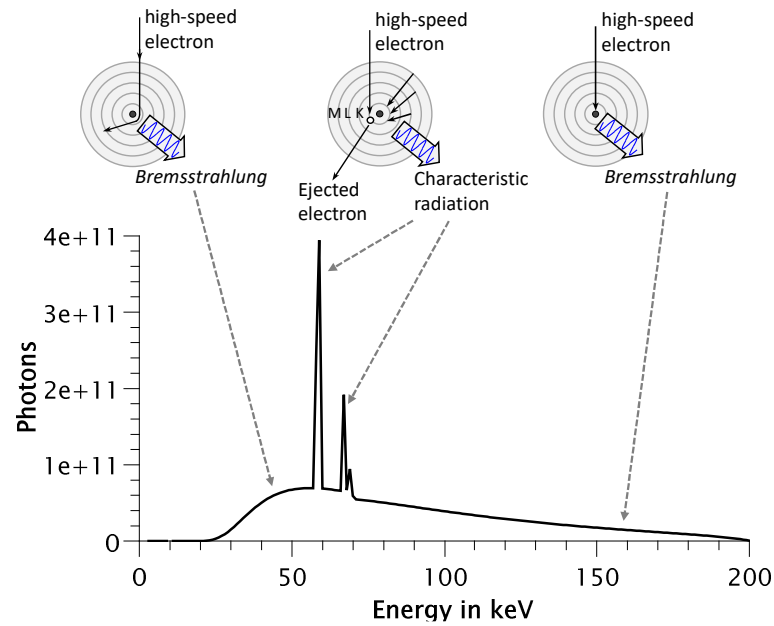


Fig. 2.3. Creation of X-rays, types of physical interactions between electrons and target atoms and their contribution for the X-ray spectrum: (a) part of the high-speed electron energy is converted into *Bremsstrahlung*; (b) characteristic radiation; and (c) entire high-speed electron energy is converted into *Bremsstrahlung* (source: [16]).

X-ray-matter interaction

Current standard CT systems use absorption contrast to measure the geometry of workpieces. Thus, the basic quantity for CT measurements is the local attenuation of X-rays by the object material.

As X-ray photons — emitted by the X-ray source — penetrate the workpiece material, several types of interactions between the X-ray photons and the atoms of the object material take place. There are four main physical interactions occurring between X-rays and material, which lead to the X-ray attenuation: (1) Photoelectric absorption, (2) Compton or incoherent scattering, (3) Rayleigh or Thompson or coherent scattering and (4) pair productions. For the level of energy used for most of industrial and CT-based CMSs (i.e. up to 600 keV), pair production is physically not possible. Therefore, a brief description of three X-ray photon-matter interaction mechanisms relevant for the energy levels used by CT-based CMSs is given. For more details on the radiation-matter interaction, see [12] and [16].

1. Photoelectric absorption occurs when an X-ray photon — with larger energy than the binding energy atomic electron of an inner shell — hit this electron. The entire energy of the X-ray photon is used to free the inner shell electron. The free electron is often called photoelectron. Characteristic radiation is created when an outer shell electron fills the gap left by the photoelectron.
2. In the Compton interaction or incoherent scattering process, an incident X-ray photon — with significantly higher energy than the binding energy of an atomic

electron — is deflected or scattered by giving up part of its energy to free this atomic electron.

3. The oscillating electric field of an electromagnetic wave sets an atomic electron into momentum vibration. The oscillation of the electron emits radiation with the same wavelength as the electromagnetic wave. This is called Rayleigh or coherent scattering.

The contribution of the described attenuation phenomena — for energies up to 250 keV — using aluminium (Al) and iron (Fe), as examples, is presented in Fig. 2.4. From the curves it becomes clear that the attenuation depends on both the material and X-ray energy.

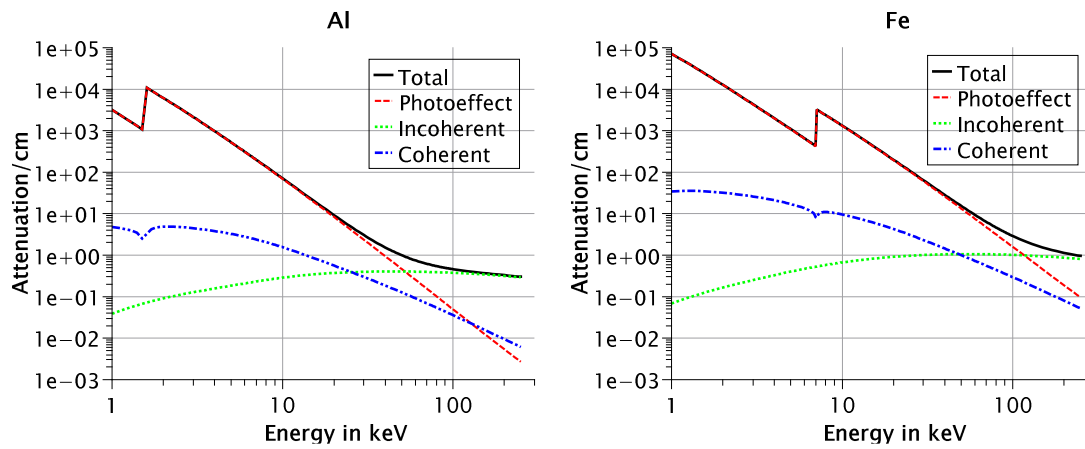


Fig. 2.4. Attenuation coefficient *vs* photon energy for (left) aluminium (Al) and (right) iron (Fe) (source: [17]).

The X-ray radiation is exponentially attenuated as it is absorbed and/or scattered while traveling through the workpiece material, see black full line in Fig. 2.4. The exponential attenuation of X-rays traveling through a homogeneous material — for a monochromatic X-ray beam — can be expressed by the Lambert-Beer's law of attenuation given by:

$$I = I_0 e^{-\mu x} \quad (2.1)$$

where I_0 is the incident and I the transmitted X-ray intensity, x the material thickness and μ the linear attenuation coefficient of the material, where μ depends on the X-ray energy and on the object material. From Eq. (2.1) it becomes clear that materials with a higher attenuation coefficient value attenuate the X-ray radiation more than materials with lower μ values.

However, if a multi-material object — made of n materials with different attenuation coefficients — is scanned the attenuation law for mono-energetic beam has to be extended by:

$$I = I_0 e^{-\mu_1 x_1} e^{-\mu_2 x_2} \dots e^{-\mu_n x_n} \quad (2.2)$$

where, μ_1 and x_1 , μ_2 and x_2 and μ_n and x_n are attenuation coefficients and penetration lengths of materials 1, 2 and n, respectively.

Material inhomogeneity is a second important characteristic neglected in the Lambert-Beer's law. Thus, the intensity of a mono-chromatic beam after running a single inhomogeneous material with total length x can be described as follows:

$$I = I_0 e^{-\int_0^x \mu(\eta) d\eta} \quad (2.3)$$

η being the term representing a small length of the spatially varying attenuation of non-homogeneous materials.

However, the Lambert-Beer's law of attenuation — described in Eq. (2.1) — including its extensions for multi-material objects and material inhomogeneities — described in Eq. (2.2) and (2.3), respectively — are valid only for a mono-energetic X-ray beam. This means, it assumes that all the photons of the beam have the same energy. For the “real case” of polychromatic beam, present in CT-based CMSs, the spectrum energy is spread over a broad range of energies, cf. Fig. 2.3. Therefore, for polychromatic X-rays, one must integrate over all spectrum energies, and the Lambert-Beer's law must be extended as follows:

$$I = \int_0^{E_{max}} I_0(E) e^{-\mu(E)x} dE \quad (2.4)$$

Therefore, for the “real case” of polychromatic beam scanning a multi-material object made of inhomogeneous materials, the solution for the transmitted intensity I can be described as follows:

$$I = \int_0^{E_{max}} I_0(E) e^{-\left(\int_0^{x_1} \mu_1(E,\eta) d\eta + \int_0^{x_2} \mu_2(E,\eta) d\eta + \dots + \int_0^{x_n} \mu_n(E,\eta) d\eta\right)} dE \quad (2.5)$$

where I_0 is the incident intensity, E_{max} is the maximum energy of a polychromatic spectrum, η is the term representing a small length of the spatially varying attenuation of non-homogeneous materials, x_1 , x_2 and x_n , μ_1 , μ_2 and μ_n are different material lengths of a multi-material object and their respective attenuation coefficients. Eq. (2.5) offers a better approximation than the simplified multi-material model presented in e.g. Eq. (2.1), however important material effects, such as scattered radiation, are still not considered in Eq. (2.5).

X-ray detection

The detector is responsible for detecting and transforming the radiation signal, scattered and attenuated by the object material, into a digital signal.

A common type of detector found in CT-based CMSs is a flat panel detector constituted of an array of detection elements. Typically, each detection element consists of a photodiode and a thin-film transistor. The photodiode array is coated with X-ray sensitive layer — modern CT systems tend to use solid-state scintillator crystals e.g. caesium iodide (CsI) or gadolinium oxysulphide (Gd_2O_2S) — which detect high energy signals (i.e. X-ray waves) and transform into low energy signals, namely visible light.

The signal workflow — arriving at and moving through the detector — is shown in Fig. 2.5. When the X-ray photons arrive in the detector, the scintillator material atoms are excited by photoelectric effect taking place through physical interactions, see § *X-ray-matter interaction*. As soon as the excitation in the atoms stops, characteristic radiation, with wavelengths ranging from visible light to ultraviolet, is produced by the scintillator. The long waves are absorbed, and an electric charge proportional to the radiation intensity, is produced by the photodiodes. During the detector exposure, the electric signal is integrated and stored in the detection element, which is working as a capacitor. The signal acquisition is activated by a signal acquisition system, which triggers the thin-film transistor. The signal acquisition system amplifies the signal and converts the analogue into a digital signal.

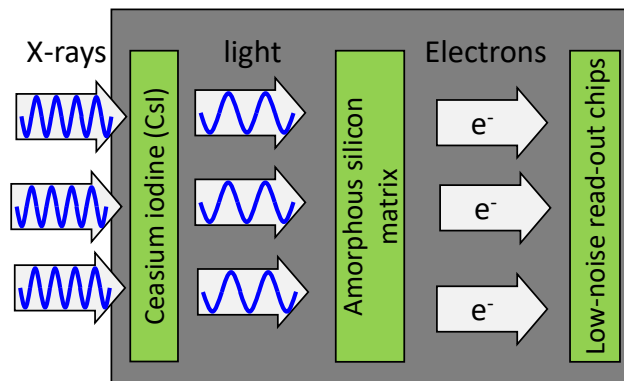


Fig. 2.5. Signal workflow in a detection element of a detector, using CsI as a scintillator material as example (source: [12]).

2.1.2 Data processing

The computer-aided data processing steps include image reconstruction, surface determination and data analysis (dimensional measurements, actual/nominal comparisons, etc.).

Reconstruction

Image reconstruction means estimating the best representation of the local density of an object, from a finite number of X-ray images taken from a finite number of angles of the object. Each X-ray projection represents the sum of the X-ray attenuation along the beam path — when being attenuated by the matter — at a single angular position. The result of the image reconstruction is a 3D voxel matrix, where each volumetric pixel represents the local attenuation of the object, as expressed by a grey level value.

For cone-beam CT using a circular trajectory and flat panel detector, the most commonly reconstruction algorithm was published in 1984 by Feldkamp, Davis and Kress (FDK) [18]. The FDK is an approximation algorithm based on the filtered back projection algorithm (FBP). Both reconstruction algorithms — FDK and FBP — rely implicitly on the mathematical solution published by Radon in 1917 [2].

The FBP algorithm is a reconstruction solution for fan-beam geometry and it is based on the Fourier slice theorem. The theorem states that the unidimensional Fourier transform of each projection is a bidimensional Fourier transform of the object. Performing the unidimensional Fourier transform of all projections, the 2D image of the object is reconstructed in the frequency domain.

However, the bigger the frequency components of the image, the bigger will be the error due to the interpolation. This results in a blurred, reconstructed image. This blur is mainly caused by the limited number of projections. A way to overcome the image blurring problem is applying a weight or reconstruction filter into the projections. Examples of commonly used filters in CT-based CMS are: Shepp-Logan, Ramp, Hanning, etc. More information of different reconstruction filters and their characteristics can be found in [19,20]. The filtered projection images are then reconstructed with the back-projection algorithm. An example reconstruction workflow based on the FBP method is presented in Fig. 2.6.

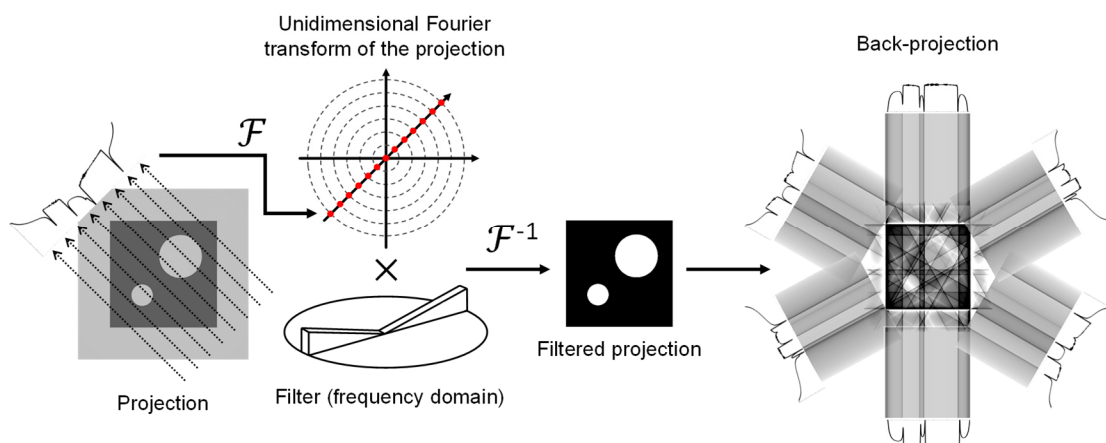


Fig. 2.6. Reconstruction example based on the FBP reconstruction algorithm (adapted from [12,21,22]).

Alternative reconstruction techniques such as iterative methods based on algebraic reconstruction techniques (ART) exist. Although these reconstruction methods can deliver comparable or even better results than FDK-based algorithms [23], the extensive computational demands — due to multiple iterative matrix operations — have limited the use of the ART-based algorithms in the industrial scenario or even in the medical field [16]. However, with the quick development of computational capabilities, the use of ART-based algorithms is becoming applicable to CT-based CMSs [23].

Surface determination

In coordinate metrology, quality control entails measuring geometrical or dimensional characteristics of an object, e.g. centre-to-centre distances between holes, form error of a sphere, *et cetera*, based on points probed (or acquired) on the object surface. Since for CT, the image reconstruction process yields a grey level-based 3D matrix (without a defined surface), geometrical or dimensional measurements can only be carried out after the virtual object surface or skin model has been estimated. Hence, the surface determination is an essential step to enable dimensional measurements.

Two widely used surface determination methods in CT-based CMS are the global threshold (or ISO-50%) and local-based (or advanced threshold) methods.

The global method was the first surface determination algorithm implemented for CT-based CMS and is based on a static threshold value (e.g. ISO-50%) used in the entire dataset. The method works on the overall grey value distribution of the CT reconstructed volume. The threshold value is usually defined as the mean value (i.e. 50%) between the background peak (i.e. air) and the material peak (i.e. workpiece) in the distribution of the grey levels (histogram). However, the quality of the dataset condition limits expressly the use of the global threshold method. Image artefacts² derived from e.g. beam hardening³, scattering effects⁴ and image noise, etc. result in a non-constant grey value over the dataset, which can introduce local surface offsets or distortions. Additionally, the optimal surface determination settings can vary over the workpiece or for a multi-material case, where the optimal settings vary for different materials. The implication is that the global-based surface determination is often not sufficient for segmenting a 3D mono- and multi-material dataset properly [25].

² Image artefacts in the CT context are artificial structures in the reconstructed image, which do not correspond to the real structure of the scanned object [24].

³ Beam hardening is well-known physical phenomenon of polychromatic X-ray spectrum, where the absorption of the low-energy photons causes non-linearities in the image, more information in § 2.2.2.

⁴ Scattering refers to incoherent scatter radiation, a X-ray-matter interaction as discussed in § 2.1.1. For more information about the effects of scattered radiation see § 2.2.2.

Consequently, more sophisticated approaches with sub-voxel precision — called local or advanced surface determination methods — have been developed. These methods estimate the surface considering the local grey level behaviour of a CT dataset, providing reliable information even in an artefact-corrupted dataset. The algorithms select a threshold value based on a small group of voxels, while taking into consideration their intensity and contrast within a set distance (grey value profile). The profiles are created based on a preliminary contour defined by the algorithm [26,27]. This preliminary contour is frequently obtained using a global threshold method. The final surface is presumably defined on the inflection point of each profile, as illustrated in Fig. 2.7. Under optimal conditions, assuming a mono-material (scenario), the accuracy of local thresholding may lie within less than one-tenth of the voxel size, as reported in [28]. An example workflow of the local gradient-based surface determination method is shown in Fig. 2.7.

A common problem of commercial software of CT data evaluation is that the detailed algorithm used for determining the surface is usually not disclosed, i.e. the exact procedure of surface determination is not published.

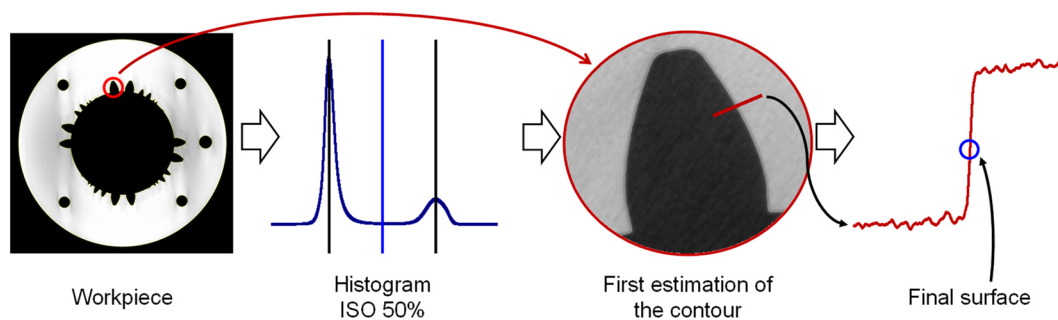


Fig. 2.7. Example workflow of a local gradient-based surface determination method. Starting from the voxel matrix, an initial contour based on the global threshold value is obtained. Normal to the initial contour, grey value profiles are considered for the determination of the surface. Presumably, the point of inflection (represented by the blue circle in the figure) of the profile curve is defined as the final surface.

Dimensional analysis

The main attraction of CT stems from the possibility to scan a large variety of materials and/or objects with high degree of complexity, and the holistic approach enabling the complete acquisition of inner and outer geometry with high information density. This allows a very fast analysis of the complete workpiece geometry by e.g. comparing two measurements obtained with other measurement devices (e.g. optical or tactile CMSs) or with a nominal model (e.g. CAD), the so-called nominal/actual comparison, see Fig. 2.8-b. This kind of analysis tool is very useful when complete information about the workpiece are required quickly, e.g. to evaluate key manufacturing processes such as additive manufacturing [29,30].

CT has established itself as a classic method and is widely used as a non-destructive technique to qualitatively detect flaws inside workpieces [31]. In the last two decades, CT has

spread towards quantitative analysis. Even areas of non-destructive testing application with the primary goal of obtaining qualitative information, have started to benefit from the quantitative results of CT [32,33]. Furthermore, procedures and reference standards to evaluate the CT performance for measurement tasks that, in the past, were mainly for qualitative analysis (e.g. porosity) — have been developed [34]. The associated measurement uncertainty of such porosity measurement have been estimated [35]. More recent developments towards measurements of fibre-orientation and -length — in carbon fibre reinforced polymers (CFRP), have expanded the measurement possibilities of CT systems even further [36]. This new field of application was facilitated by developments in metrological applications, where more precise systems with better resolution are required.

In production metrology, a common way of evaluating a workpiece is based on its functionality, which in many cases can be determined based on the object's geometry and/or dimensions. The specific measurement (e.g. distances, size, angle, form error and position), is then compared with the specified dimensions and its tolerance and normally a decision — based on the measurement result and its uncertainty — of conformance or no conformance is taken.

Classic dimensional and geometrical evaluations with a CT-based CMS are performed analogously to tactile- and some optical-based CMS measurements. The measurement is based on feature extraction based in turn on point acquired on the objects surface. In tactile systems for example, the surface of the workpiece is physically probed by the probing element (normally a sphere). The point's cartesian coordinates, i.e. “ x ”, “ y ” and “ z ”, are recorded with an unit vector (m_x , m_y and m_z), which represents the orientation of the surface normal. The latter is used mainly for mathematical operations, e.g. probe sphere radius correction. For CT, however, the points are probed in a virtual surface (see § *surface determination*) in the reconstructed 3D image and the cartesian coordinates are recorded; no further morphological operation is necessary, e.g. probe correction. The point coordinates are normally used for the extraction of features e.g. by fitting geometrical elements for dimensional and/or geometrical analyses, see Fig. 2.8-a.

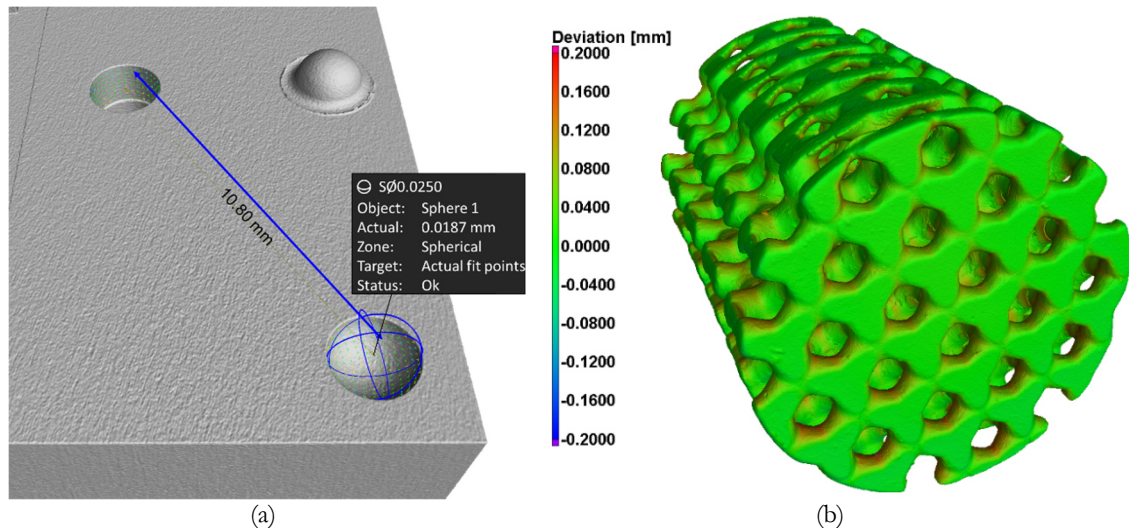


Fig. 2.8. Examples of data analysis with CT: (a) length measurement between two fitted geometrical elements based on points probed on the “virtual surface” and form error analysis in a geometrical element; (b) deviation map from a nominal/actual comparison of the CT data (surface) with the nominal model, (CAD).

Uncertainty evaluation

The demand for reliable and traceable results is increasing as CT-based CMS is gradually being established as an important measurement tool for quality control in several branches of industry.

As briefly discussed in Chapter 1; CT as measurement coordinate technology still is on its way to achieve complete and stand-alone traceability. The main cause for this lack of traceability is the difficulty of estimating and expressing the uncertainty of CT measurements. The rather large number of influencing factors and — to a certain extent — the unknown way they influence the measurement result are the main difficulties that have yet to be overcome.

The classic approach to uncertainty estimation is based on the guide to expression of uncertainty in measurement (GUM) [37]. In the GUM method, the measurement is modelled considering all (relevant) factors influencing the measurement result. However, the complex measurement chain of CT-based CMS limits the applicability of the GUM method. The description of the influencing factors is already partially covered in the German guideline for CT-based CMS VDI/VDE 2630-1.2 [38]. However, issues such as an incomplete or unsatisfactory description of the influence quantities (i.e. not all factors are covered) limits the applicability of the GUM to CT.

The ISO 15530-3:2011-10 [39] standard offers a potential way for the uncertainty estimation of CT-based CMS measurements. Its approach relies on techniques using calibrated workpieces or standards. An important characteristic of this uncertainty estimation technique is the principle of similarity. This means, the uncertainty estimation of a measurement of an arbitrary workpiece, using a calibrated reference standard, can only be

carried out if certain similarity conditions are fulfilled (e.g. measurement strategy, dimensional or/and geometrical characteristics, etc.). The current version of the ISO standard describes a general approach for uncertainty estimation of tactile CMS measurements, and it does not address the specifics of CT measurements. Hence, an adaptation, requiring significant changes, of the ISO 15530-3 standard for CMSs using a CT sensor is necessary. Nevertheless, some authors have studied the applicability of this method to CT-based CMS measurements, e.g. [40].

The German guideline VDI/VDE 2630-2.1 [41] already addresses the specifics of CT-based CMSs for the measurement uncertainty estimation. With a focus on the determined measurement uncertainty and on the tolerance to be met, a procedure to assess a test process using CT-based CMS in terms of the derived characteristic test process suitability is described. This characteristic serves to evaluate the measurement and production process.

Interest in alternative methods of measurement uncertainty estimation based on computational simulation is increasing. This concept is part of the scope of the ISO/TS 15530-4 [42] standard for uncertainty evaluation for CMSs based on computation simulation. The standard specifies requirements for the application of the uncertainty evaluating software to measurements made with CMSs. It also describes testing methods for verifying uncertainty evaluation software and various test procedures for the evaluation of the task-specific measurement uncertainty are given. However, the ISO standard does not consider the specifics of CT. Although there exist CT simulation tools (e.g. aRTist [43], SimCT [44], Scorpius Xlab® [45]), very limited work has been done on the estimation of the measurement uncertainty for CT-based CMSs using simulation tools. An example of such work is given in [22]. Because of the increasing demand for reliable measurements using CT, researchers and industry started to collaborate in this topic [46].

2.2 Influencing factors and effects of multi-material measurements by CT

An overview of the most important factors influencing CT measurements throughout its measurement workflow is presented in Fig. 2.9. Particularly for multi-material measurements, factors associated with the generation, absorption and detection of the X-ray radiation are of relevance. The relevant influencing factors contribute to undesired physical effects — e.g. changes of the X-ray spectrum caused by beam hardening while traveling through the workpiece material. The incorrect consideration of such effects generates inconsistencies or artefacts in the images, degrading the scan quality. In Fig. 2.9, relevant influencing factors of multi-material measurements are highlighted in bold. Although some material effects depend, to a certain degree, on the system geometry (e.g. scattering),

geometry-related factors are less important for multi-material measurements, since the determination of the system geometry has no direct influence on multi-material effects.

In this section, relevant influencing factors of multi-material measurements are described along with physical effects and their effect on the images and measurements.

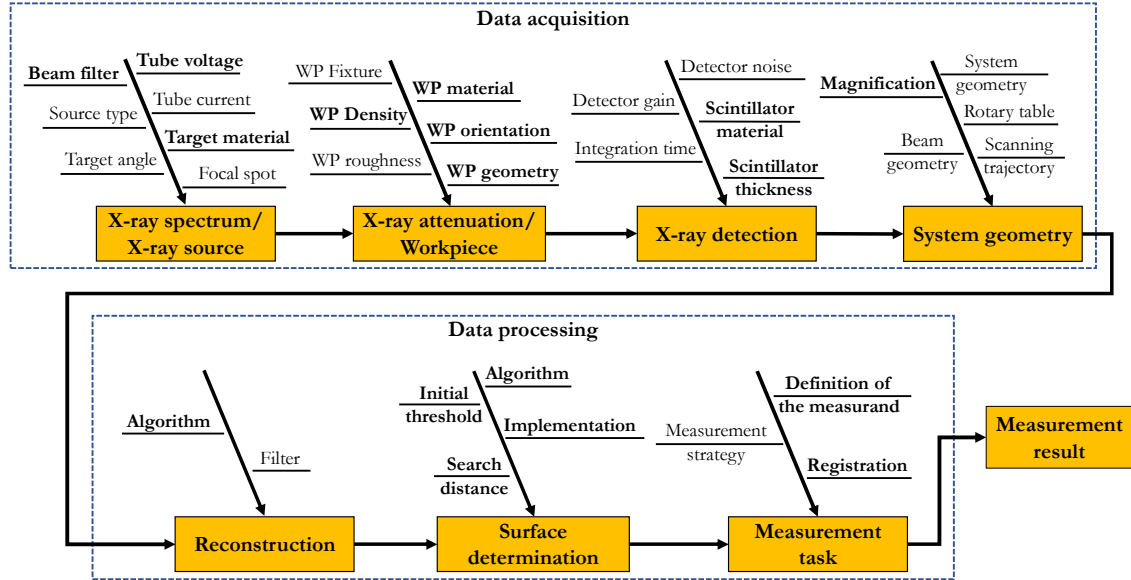


Fig. 2.9. Relevant influencing quantities of CT dimensional measurements. Important factors related to multi-material measurements are highlighted in bold.

2.2.1 Relevant influencing factors

This section presents a description of the factors influencing the X-ray spectrum, absorption and detection.

X-ray spectrum-related influencing factors

The X-ray spectrum determines the beam energy and intensity, and hence its penetration capability and the number of X-ray photons being produced, respectively.

The radiation energy is determined by the X-ray photon energy, which in turn depends on the electron kinetic energy (i.e. velocity) of the high-speed electrons hitting the target material, see *X-ray generation* in § 2.1.1. The velocity of the electrons depends on the **acceleration voltage** across the cathode and the anode; the greater the acceleration voltage, the greater the kinetic energy and thus beam energy.

The number of photons is related to the electric current flowing in the cathode; higher electric currents generate larger number of photons. In general, the electric current is primarily responsible for the noise and contrast observed in the images: higher tube currents yield better images regarding noise and contrast. However, there are further parameters to be considered when setting the tube current, e.g. an increase of the focal spot size with increasing tube current.

In addition to the tube voltage, the X-ray spectrum can also be modified by a **beam-filter**, a physical part attached at the exit of the X-ray source. The main purpose of beam-filters is to increase the spectral beam effective energy by blocking the low-energy photons of a polychromatic spectrum. The filter characteristics depend on the material (i.e. its material attenuation curve, see § *X-ray-matter interaction*) and thickness of the beam-filter. Normally, moderately or strongly absorbing materials are used as beam-filters, e.g. copper, tin or silver, with a thickness ranging from 0.1 mm to 3 mm. The thicker the filter, the higher the resulting spectral energy. Regarding the material attenuation coefficient, generally, beam-filters made of materials with high attenuation coefficient (i.e. average of the X-ray polychromatic energies) tend to result in a higher spectral energy than low absorption materials. Beam-filters also reduce the overall beam intensity, since they decrease the number of photons reaching the detector. Therefore, they increase the image noise and reduce the image contrast.

The **target material** defines the distribution of the X-ray spectrum [47]. The spectrum energy and intensity are significantly altered by different target materials, see Fig. 2.10 the resulting X-ray spectra using different target materials. Tungsten is the most common material used in CT-based CMSs, due to its high atomic number and high melting point. Alternative materials include, for example, molybdenum, silver and copper. Although the anode material is usually inaccessible, some CT systems are equipped with X-ray sources with multiple target materials, which do allow the user to change the material.

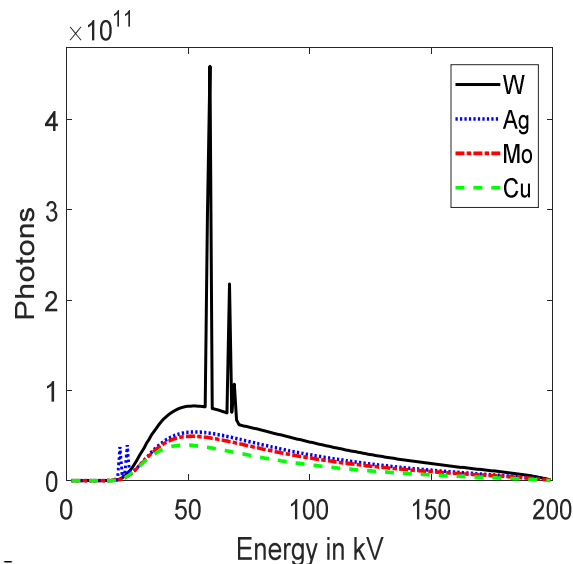


Fig. 2.10. X-ray spectra created with 200 kV; 0.2 mm Cu filter from different anode materials: Tungsten (W), silver (Ag), Molybdenum (Mo) and Copper (Cu) (Source: Spectra generated in aRTist [43]).

The use of **multiple material targets** could be beneficial when multi-material objects are measured, since different target materials generate different spectra. Therefore, the source (different target materials) could be reconfigured to suit each material of the

workpiece [48]. A drawback of this multiple target approach would be the need for multiple scans, which would significantly increase the acquisition time. Other common approaches of multiple spectrum scans use multiple X-ray sources or multi-spectrum scans with e.g. different tube voltages and beam-filters applied to single source. Reiter et al. [49] showed that such dual-spectrum approaches can benefit dimensional measurements of multi-material workpieces. However, with these approaches additional factors will contribute to the measurement uncertainty, e.g. data fusion, a more complex determination of the system geometry, etc.

The selection of the X-ray related scanning parameters for multi-material measurements is a trade-off between several variables. An example is the beam energy: on one hand, the beam energy must be set high enough to be able to penetrate all of the materials. On the other hand, if the beam energy is set too high, the low absorbing material barely attenuates the high energy photons, generating low contrast images.

X-ray absorption-related influencing factors

The workpiece material and thickness determine its absorption characteristics, i.e. how strongly absorbing the material is and thus how the X-ray radiation is attenuated. The absorption of the X-ray radiation by the **workpiece material** depends on material's **atomic number**, **density**, **thickness** and the **wavelength of the incident beam**. These dependencies are illustrated in Fig. 2.11. In general, materials with higher density and higher atomic number have a higher absorption, while a thicker material reduces the number of photons reaching the detector and thus the intensity.

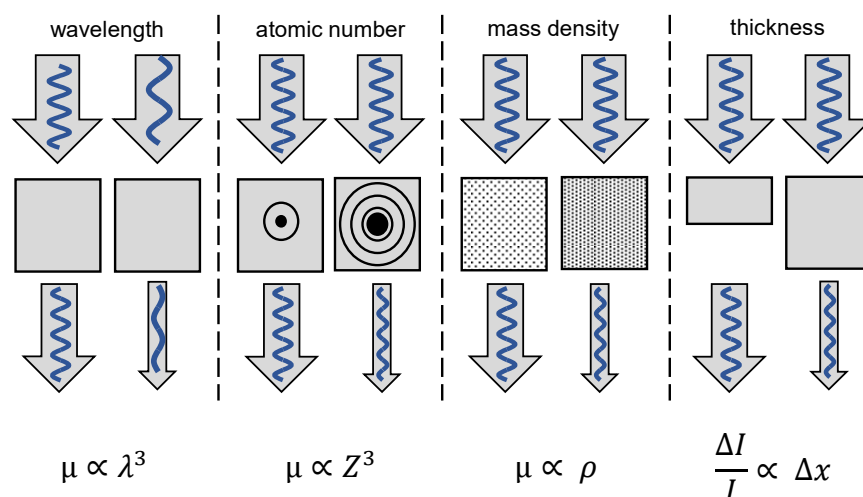


Fig. 2.11. Causes of X-ray absorption by the workpiece materials (source: [12]). See below for definitions.

In Fig. 2.11, μ is the X-ray absorption, λ the wavelength of the incident beam, Z and ρ are the atomic number and density of the material, $\Delta I/I$ is the change in intensity between the incoming and transmitted beam, and Δx is the variation of the material thickness [12].

The **geometry** and **orientation of the workpiece** are important parameters affecting the quality of the scan as well. Both parameters are associated with the total material penetration length the radiation travels through. Long penetration lengths lead to more X-ray photons to be absorbed (as illustrated in Fig. 2.11). Excessive absorption of the X-ray photons can cause e.g. photon starvation effects, more details in § 2.2.2.

Factors influencing X-ray detection

As the detection of X-rays relies on the absorption mechanisms between X-ray radiation and scintillator material, the detector's response curve is critically dependent on the incoming **X-ray spectrum**, **scintillator material** and its **thickness**. In a polychromatic spectrum, the high-energy components reaching the detector are, to a certain extent, not absorbed by the scintillator material. The high-energy radiation passes through the detector undetected. This means that part of the signal is lost.

Associated to the absorption of the X-ray beam by the scintillator material, Illema and Bartscher 2017 demonstrated that the geometrical magnification of cone-beam CT depends on the X-ray spectrum, detector material and thickness [50]. This dependency arises from the fact that, photons with different energies are absorbed at different depths inside the detector's **scintillator**, depending on its **material and thickness**. The absorption at different depths of the detector changes the effective relative distance between source and detector, varying the geometrical magnification of the scan. As the object material modifies the spectrum arriving at the detector, the dependency of the effective position of the detector plane on the absorbing characteristic of the object material was demonstrated by [51].

Finally, quantities such as the detector's quantum efficiency (DQE) for the conversion of X-ray radiation to visible light, and the time constant for the conversion process (i.e. afterglow) also depend on the scintillator material [12].

Reconstruction

As already discussed in § 2.1.2, FBP-based FDK algorithm is the most used reconstruction algorithm used in CT-based CMS datasets (i.e. a cone-beam with circular trajectory), mainly because its relatively low computational demand and high speed. However, a known problem with standard FDK reconstruction algorithms is they are based on several approximations and assumptions that do not correspond to the "real" CT datasets. The sum of X-ray attenuation for every beam path is calculated assuming that X-rays are exponentially

attenuated according to Lambert-Beer's law, described in Eq. (2.1). It assumes a mono-energetic beam and single homogeneous material for all X-ray paths and angles of a CT scan. The complex way in which polychromatic radiation interacts with matter, results in a changing X-ray spectrum while travelling through the material. An example would be the disproportionate absorption of low-energy photons. Although these divergences have been included in Eq. (2.5), they are not considered by the FBP-based reconstruction algorithms, resulting in image artefacts and potentially impacting dimensional measurements.

Algebraic reconstruction techniques may offer a potentially better solution for the image reconstruction of multi-material objects, as these techniques take into account different beam energies, thereby reducing the influence of X-rays going through the matter effects [12]. However, the requirement for high computational capacity limits (the broader) use of these matrix-based reconstruction techniques.

Reconstruction filter: In performance verification tests, usually high-quality reference standards (i.e. low form error and small surface roughness) are used. This implies that most of the observed form error or/and surface roughness is introduced by the noise of the measurement system sensor, and potentially, the projection sampling. The reconstruction filter's main purpose is to remove the high-frequency components of the image, reducing the image blur introduced by the interpolation (see § 2.1.2). Besides this, the filtering process also removes noise of the dataset, due to the high-frequency nature of noise. As a consequence, the reconstruction filter influences measurement results of form and roughness. Preliminary studies showed a small effect on form and size measurements in a multi-material reference standard, when using Ramp (also called Ram-lak) or Hanning reconstruction filters. However, a more detailed study on the influence of different reconstruction filters in dimensional measurements of multi-material workpieces is necessary and a potential topic of further research.

Surface determination

The quality of the reconstructed volume, i.e. image contrast, noise, scattering artefacts, beam hardening artefacts, pole artefacts, et cetera, play an important role in the surface determination process.

The **algorithm** used for the surface determination (e.g. global- or local gradient-based) is — in most of the cases — of vital importance to achieve low measurement errors. The global-based method is extremely sensitive to grey level variations in the dataset, caused by e.g. image artefacts, leading to offsets of the surface. The local gradient-based surface determination method, by contrast is declared by its developers to be less sensitive, delivering better measurement results [28].

Although specialised surface determination algorithms (e.g. local gradient-based algorithms) are less sensitive to image artefacts, the inhomogeneities created in the image can significantly degrade the estimation of the object surface and consequently worsen the measurement result.

For global-based methods, the definition of the surface relies entirely on the **threshold value**. For the local-based methods, however, the threshold value plays a secondary role, as it serves “merely” as a starting contour for the next steps of the algorithm, see § 2.1.2, but it still has some impact on the surface determination.

For multi-material measurements, the surface determination algorithms, which depend on the threshold value, usually consider only one material. This means that the surface determination setting e.g. definition of the starting threshold value is optimised for a particular material. This can result in a surface with large offsets in other materials. These offsets can result in large size errors or, in the worst-case, the inability to perform the measurement, as the surfaces are not or only partially identified. One such example is the high absorbing material (HAM) in Fig. 2.12. Thus, it becomes clear that the use of one threshold value is not suitable for multi-material scenarios and a pre-processing step or a two-step data processing is very often necessary. This current problem characterises an important **limitation** of the state-of-the-art surface determination algorithms.

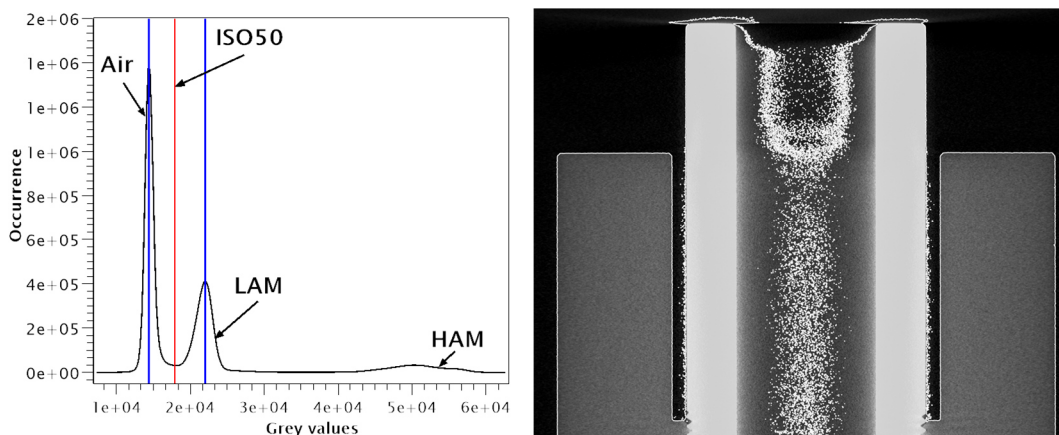


Fig. 2.12. Surface determination in a multi-material assembly: (left) histogram showing threshold optimised for the low absorbing material (LAM) only, (right) surface in the volume data, the inner cylinder made of HAM is not identifiable (white contour represents the estimated surface).

The **search distance** is the distance of a profile normal to the initial contour, that the algorithm considers when determining the final surface. As the surface determination is carried out for each individual profile, the surface decision for artefact-free regions does not depend on corrupted (by image artefacts) regions — as long as the corrupted regions are found outside of the search distance.

For multi-material measurements, if the difference of the attenuation coefficients (i.e. grey levels in the 3D image) between the materials to be measured is small enough so that the “correct” material surface lies within the region covered by the search distance, then the “correct” material surface lies within the region covered by the search distance, then the local-based surface determination algorithm is still able to determine the surface of both materials correctly. However, if the grey values of the materials differ so that, the surface of one material is lying outside of the region covered by the current settings of initial threshold and search distance, severe problems can arise during the surface determination of a material, as shown in Fig. 2.13. This can cause potentially surface offsets or create non-existing structures in the air region.

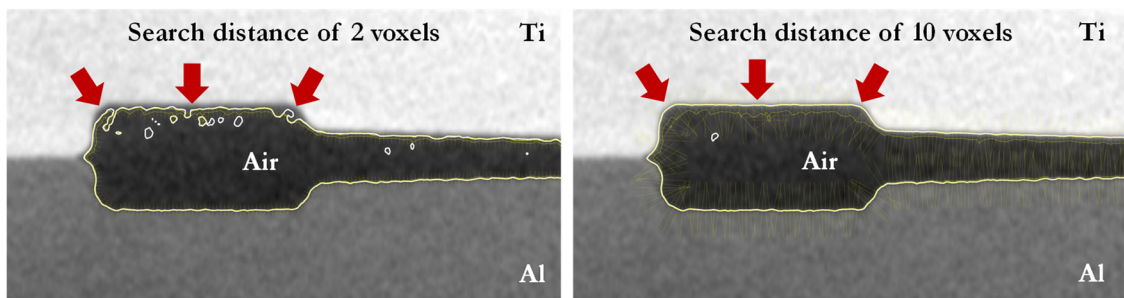


Fig. 2.13. Example of the search distance influence on the determination of the final surface in a multi-material assembly with moderate attenuation coefficient difference (here Al & Ti) using a local-based algorithm as implemented in the CT evaluation software VG Studio Max. This highlights the differences between the final surface being determined with a search distance of two or ten voxels with the same starting threshold value.

2.2.2 Relevant effects

Multi-material effects on a CT scan are linked to the interaction between X-ray radiation and matter and X-ray detection. The most important effects are scattered radiation, beam hardening and detectability of the X-rays depending on the spectrum. In this section, a discussion of the relevant physical effects originating from the X-ray-matter interaction and X-ray detection is presented. Additionally, the effects arising from multi-material measurements are discussed.

Beam hardening effects and their influence on multi-material measurements

In general, low-energy photons of a polychromatic X-ray spectrum are more strongly attenuated than high-energy ones, as schematically illustrated in Fig. 2.14. This effect increases the beam effective energy, resulting in a “harder beam”. This phenomenon is the cause of the so-called beam hardening effect [12,16].

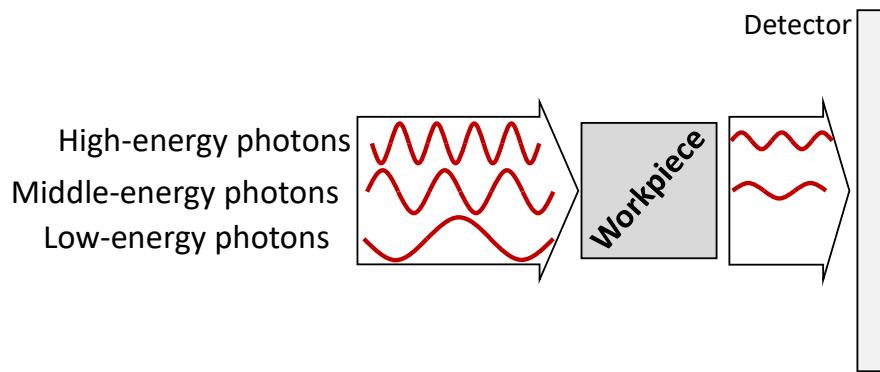


Fig. 2.14. Illustration of the origin of beam hardening effect in a mono-material workpiece. In the illustration low-energy photons of a polychromatic spectrum are more strongly attenuated (smaller amplitude at constant frequency) by the material than the high-energy photons.

Fig. 2.15 didactically presents a multi-material workpiece being irradiated by an unfiltered polychromatic X-ray from two directions. Along the horizontal, the radiation first passes through the HAM and then the low absorbing material (LAM). In this sequence, the low-energy photons are first absorbed by the HAM, allowing only medium- and high-energy attenuated photons to pass through it. In other words, the HAM increases the effective energy of the X-ray beam, effectively serving as a beam-filter. Consequently, artefacts associated with beam hardening effects, caused by absorption of soft photons, will appear in the HAM. The medium- and high-energy components of the spectrum reaching the LAM have enough energy to be attenuated less by the material, therefore fewer beam hardening effect is expected in the LAM.

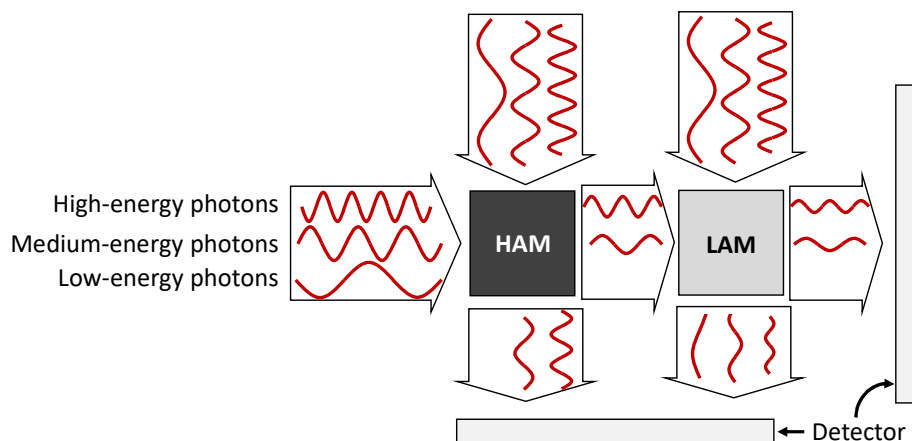


Fig. 2.15. Beam hardening effect. Low-energy photons are easier absorbed than high energy photons by higher absorbing materials.

Beam hardening effects mainly appear in the image as artificial (not representing the object) changes of the grey values. Cupping and streaks artefacts are the most common manifestation of beam hardening in the reconstruction images. Fig. 2.16 presents an example of a cupping artefact in a multi-material scan. The scan is composed of two hollowed

cylindrical parts made of different materials. The outer and inner cylinders are made of low and high absorbing materials, respectively. In the HAM, i.e. the inner cylinder, a cupping artefact caused by beam hardening is observed, see the grey level profile in Fig. 2.16. Cupping artefacts appear e.g. in symmetrical workpieces made of high absorption material, where the outer region of the HAM present a higher grey value than the inner region. In the example presented in Fig. 2.16, the grey values in the HAM decrease by one-third from the outer to the inner part of the cylinder. In the outer cylinder, i.e. in the LAM, no or very little artefact originating from beam hardening can be observed. The outer cylinder is made of low absorbing material, letting even the low-energy or soft photons go through it.

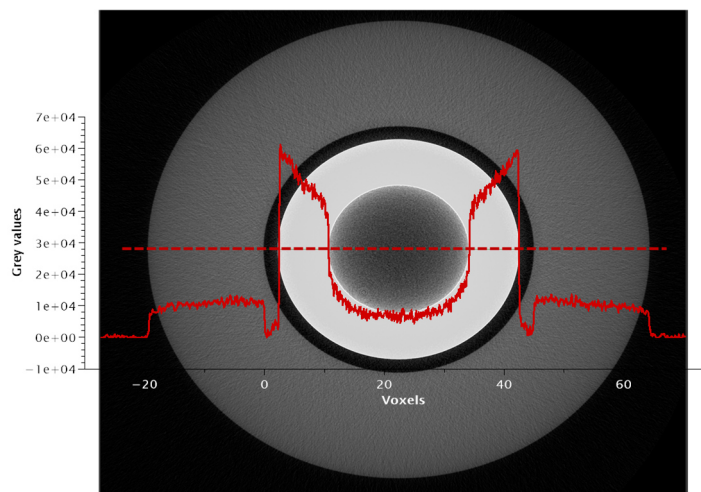


Fig. 2.16. Cupping artefact caused by beam hardening effect, full red line represents the profile in grey values along the dashed red line (source:[52]).

For dimensional measurements, cupping effects commonly cause problems even for local-gradient-based surface determination algorithms. The difficulties stem from the unpredictable grey value variation in the border region of materials, generating an offset of the surface, and thus appearing to alter the measured size of workpieces.

Scattering effects and their influence on multi-material measurements

Above a certain energetic level, incoherent scatter becomes the predominant interaction mechanism between photon and materials, see attenuation curve of Al from ~ 50 keV and of Fe from ~ 100 keV in Fig. 2.4, § 2.1.1. From those curves, it becomes clear that scattered radiation is an intrinsic property of the materials, which also depends on the X-ray energy. Generally, the high-energy components of the spectrum are more susceptible to scattering effects.

Incoherent scattered radiation — as the name suggests — are X-ray photons that have deviated or scattered from their incident path, see Fig. 2.17. Since the deflection angle of the scattered photon is random, the intensity distribution of the scattered photons received by

the detector is a background signal with low frequencies, similar to background noise [16]. Thus, the signal arising from scattered radiation can be difficult to recognise and to separate from background noise.

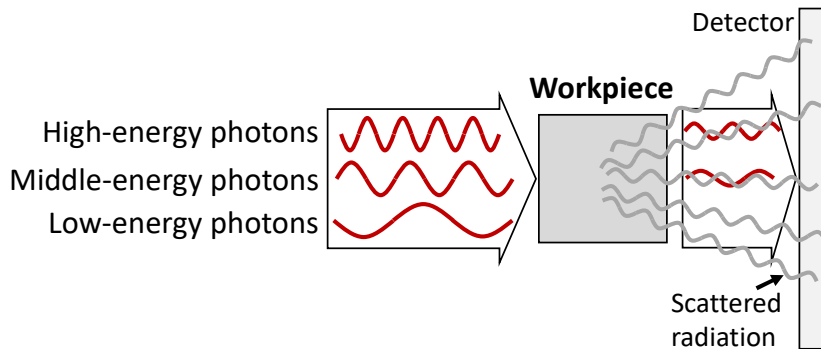


Fig. 2.17. Scattering radiation from the object.

The scattering effect causes an offset of the background signal, diminishing the signal-to-noise-ratio of materials in the acquired image. This could be critical when multi-material workpieces made of materials with divergent attenuation coefficients are measured, because the offset signal caused by scattering, might dominate the LAM signal, see Fig. 2.18.

Low absorbing materials produce more scattered radiation from lower energy levels than high absorbing materials. This is explained by the fact that the higher the difference in energy between the incoming photon and the material electron binding energy the higher is the probability of incoherent scatter interaction [16].

Another physical impact of the scattering for multi-material measurement may arise when the materials are aligned in such a way that the beam path crosses both materials. The first material may act as a beam-filter. This leads to low-energy components of the spectrum being strong attenuated by the first material, hardening the spectrum. From a X-ray-matter interaction perspective, the hardening of the spectrum may culminate in a relative increase of the scattered radiation in the LAM, as illustrated in Fig. 2.18-top. The increase of the scattering effects reduces the signal-to-noise-ratio (SNR) of the entire measurement. When the LAM is irradiated before the HAM, the low-energy scattered photons are absorbed by the HAM and do not reach the detector, see Fig. 2.18-bottom.

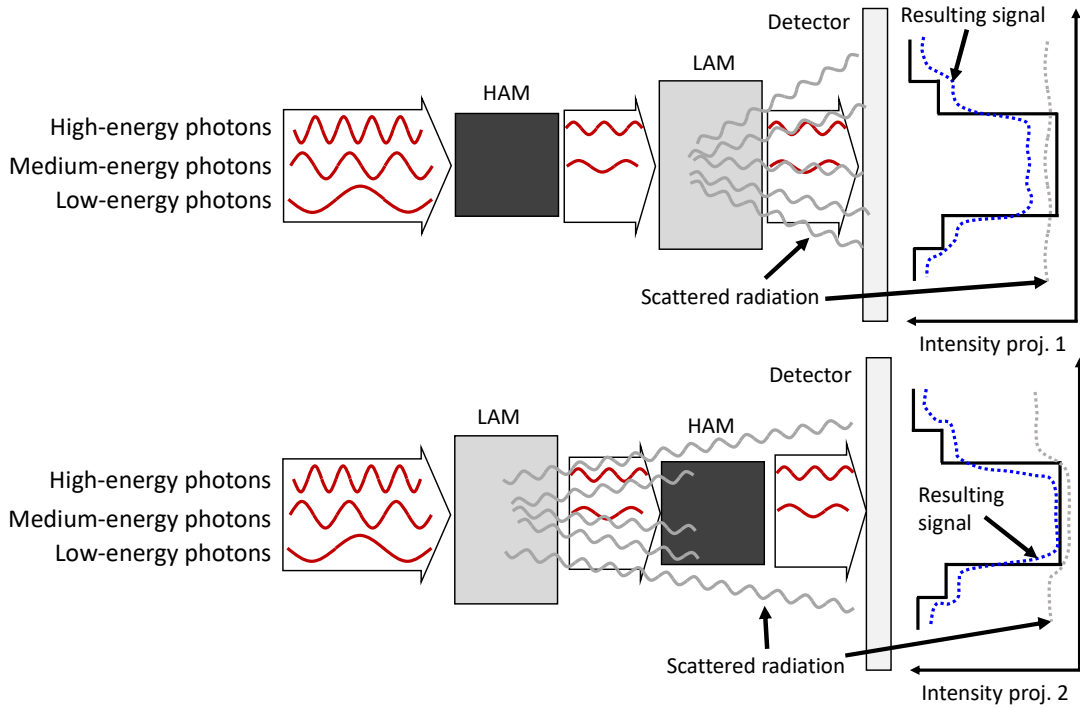


Fig. 2.18. Scattered radiation in multi-material measurements: (top) low absorbing materials generate relative more scattered radiation when the HAM serves as a beam-filter; (bottom) HAM blocking the low-energy scattered photons from the LAM.

Photon starvation, partial-volume effects and their influence on multi-material measurements

When the material to be scanned is extremely high absorbing or very thick, the radiation is attenuated so strongly that almost no photons reach the detector, as schematically illustrated in Fig. 2.19. This effect generates streaks in the reconstruction image by two different phenomena: photon starvation and partial-volume effects.

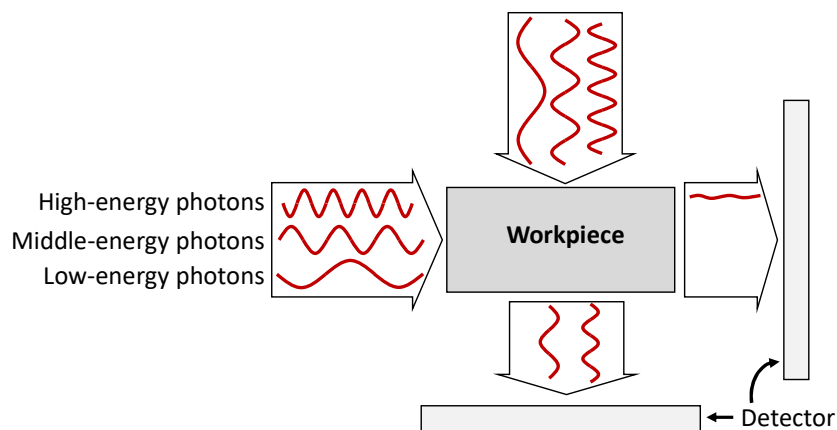


Fig. 2.19. Photon starvation effect. Massive absorption of the radiation so that no or almost no X-ray photon reaches the detector.

The massive reduction of the number of photons reaching the detector significantly increases the scan noise. The noisy signal and residual error of the detector are further

amplified by reconstruction algorithms, generating streaks in the reconstruction volume [12]. This is the root cause of the so-called photon starvation effect.

In multi-material measurements photon starvation can create noisy surfaces, being particularly with the LAM due to its bigger impact on the signal-to-noise ratio of the LAM.

When the radiation is completely attenuated by the material, no radiation at all will reach the detector at that angular position. However, at other angles of the scan, the detector may still receive a signal from the affected regions. During reconstruction, inconsistencies arising from those projection-dependent signals, result in strong streak artefacts. This is known as the partial volume effect [12].

In the multi-material scenario presented in Fig. 2.20, the HAM will be not detected and created several streaks is expected to appear in every direction of the reconstructed volume. The measurement of the LAM will be severely impaired by the streaks caused by partial-volume or photon starvation effects from the HAM.

The high frequency distortions caused by streak artefacts in the image increase the local surface noise, and possibly cause a surface offset, degrading the shape of the workpiece locally.

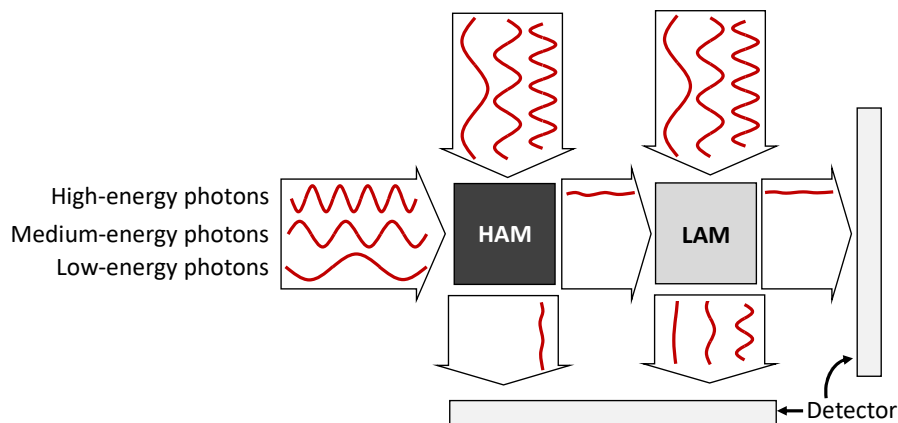


Fig. 2.20. Photon starvation in multi-material measurements. Projection-dependent signals, originating from the photon starvation, can create pronounced streak artefacts in the image.

Multi-material effects related to X-ray detection

In a multi-material workpiece, beam hardening effects are introduced by the high absorbing materials hardening the spectrum more than materials with low attenuation coefficients would. This means that the radiation is absorbed at different effective penetration depths within the detector. The complexity of this effect rises when observed in different orientations of the workpiece. Throughout the scan, the changing orientation alters the conditions of the (prevalent) X-ray to matter interaction. This means the radiation may be detected at varying penetration depths of the detector, subject to the object orientation, as illustrated in Fig. 2.21. The main issue here is that the detector is usually treated as a perfect

plane, and that reconstruction algorithms often consider the relative effective distance between X-ray source and detector to be constant throughout the entire scan.

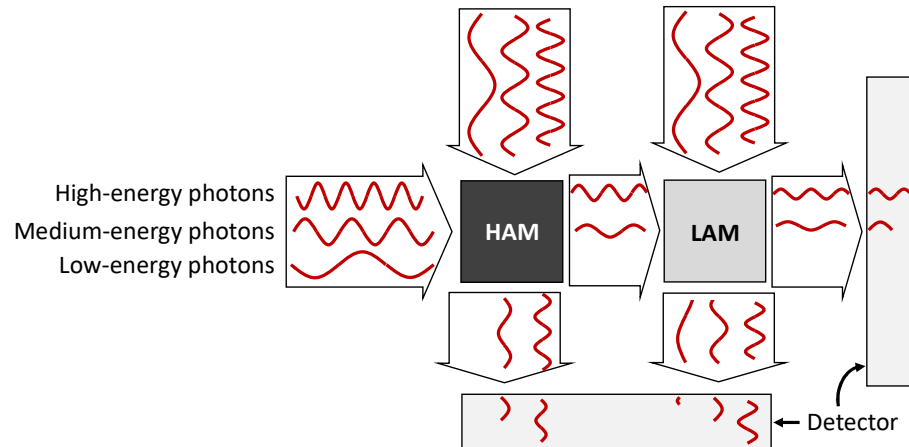


Fig. 2.21. Dependency of the detector absorption depth on multi-material workpiece.

The detection sensitivity of X-ray detectors is correlated with the scintillator material, its absorption characteristics and thickness. An undesired effect arising from this dependency, is that the high-energy components of a polychromatic X-ray spectrum are not or poorly absorbed by the scintillator. This means that the radiation largely passes through the scintillator and the signal from the high-energy components is not or poorly detected. This leads to the conclusions that the detector's response curve depends on the incoming X-ray spectrum, and on the object material in turn, since the latter modifies the spectrum. Interpreting this effect in the context of multi-material measurements, a dependency of X-ray detectability on the workpiece materials and its orientation in the scan may be expected. In general, high-energy photons are worse detected than low-energy photons. Therefore, the detectability is worse for high absorption material than is for low absorption materials.

Influence of multi-material related effects on the measurements/surface

The influence of scattering and beam hardening artefacts on dimensional measurements remains — to a certain extent — unclear and unpredictable. Some authors have studied the influence of these artefacts on dimensional measurements. *Lifton 2016 et al.* [53] conducted an experimental study of the influence of scatter and beam hardening on dimensional CT measurements. The results showed that gradient-based surface determination algorithms are robust enough not to be influenced by these artefacts, for the measurement scenarios studied. *Lifton and Carmignato 2017* [54] studied the influence of scatter and beam hardening using simulation data. It was found that beam hardening artefacts greatly influence the measurement results even when applying the state-of-the-art gradient-based surface determination algorithm. *Bartscher et al. 2016* [55] showed the importance of considering

beam hardening artefacts on performance verification tests, finding major effects of beam hardening on the dimensional measurement of an aluminium hole plate.

The multi-material influence on dimensional measurements and its contribution to the measurement result and uncertainty has not yet been extensively studied. However, the influence of multi-material effects on dimensional measurements were described in [56–59]. With respect to the measurement uncertainty of multi-material measurements, *Schmitt et al. 2018* [60] proposed an optimisation model of CT image parameters for dimensional measurements of multi-material workpieces. *Heinzl et al. 2008* [61], presented a statistical analysis method for multi-material workpieces based on a dual-energy CT approach. A probability dataset (CT volume), based on two scans with different energies, was obtained using a local histogram analysis technique. Actual/nominal comparisons of the computed probability datasets with CAD model of the workpiece were also part of the analysis.

Several approaches of data correction of multi-material effects have been applied to metrological and industrial CT scans. *Reiter et al. 2019* [49] have shown — using a multi-material reference standard — that beam hardening artefact correction methods designed for medical applications can benefit dimensional measurements as well. *Krumm et al. 2010* [62] presented a beam hardening correction method for multi-material objects based on the retro-projection approach. Materials are segmented in the reconstructed CT image. Then monochromatic and polychromatic re-projections are calculated using ray tracing. The amount of correction is calculated by the difference between both re-projections. The method appeared to be efficient from a qualitative point of view; no result regarding multi-material measurements was reported, however. *Amirkhanov et al. 2012* [63] applied a metal-artefact reduction technique based on 2D projections to a multi-material workpiece. Here, the projections are reconstructed, and metal parts are segmented in the reconstructed volume. The next step of the method consists of mapping the segmented voxels onto the projections using forward projection and removing the segmented areas from the projections. The affected regions are then interpolated from adjacent areas without metal content and reconstructed. Finally, the resulting 3D volume is fused with metal parts extracted from the original reconstructed 3D volume. *Kratz et al. 2014* [64] implemented a metal artefact reduction method for multi-material objects based on a non-Equispaced Fast Fourier Transform. The outcome of this study is that the higher dimensional interpolation for metal-artefact reduction applications result in better image results for NDT applications. The Fourier-based methods yielded satisfactory results. *Lifton 2017* [65] applied on multi-material linearization-based beam hardening correction for CT. The evaluation was mainly based on image metrics, i.e. no dimensional analysis was reported. *Herl et al. 2018* [66] presented a

multi-orientation method to correct strong absorption-related artefacts in multi-material workpieces. This method has great potential for artefact-reduction for multi-material workpieces with large difference in attenuation coefficients. However, a disadvantage of the method for potential use in dimensional metrology is the great dependence on the registration procedure of the multiple scans.

In addition, there have been further studies concerning surface determination for multi-material measurements.

Tan et al. 2011 [25] studied the material-dependency of the surface determination. The results have shown that high absorption materials, which are more prone to beam hardening artefacts severely affect the surface, and therefore the measurement result. The authors of [25] also studied a multi-material measurement. Similar effects were found. *Borges de Oliveira et al. 2016* [67] analysed the influence of the surface determination in multi-material scenarios using several segmentation methods from a commercial software [67]. *Heinzl et al. 2007* [68] compared a series of global and local thresholding methods for dimensional measurement and stated the necessity of sophisticated algorithms for dimensional measurement tasks [68]. The segmentation of multi-material workpieces using a dual-energy CT was presented by *Heinzl et al. 2007* [69]. An improvement of the CT results by up to half of the mean deviation using a dual energy CT, compared with a mono-energy CT scan was achieved [69]. *Fujimori and Suzuki 2005* [70] presented a new method for extracting surfaces from a dual-material dataset based on voxel classification. A maximum error of the extracted surface of one voxel size was achieved [70]. *Shammaa et al. 2010* [71] proposed a combination of two well-known algorithms (i.e. region growing and graph-cut) for classifying the volumetric model of a multi-material CT dataset. The algorithm works well for extracting surfaces of materials that have a high attenuation difference (materials with a large difference concerning X-ray attenuation) [71]. However, the method has some problems when classifying voxels with similar grey values, especially if the dataset is very noisy.

2.3 Performance verification of CT-based CMS

The development of international standards and technical guidelines describing specifications for the application of CT as a CMS is currently under development. The progress in standardisation represents an important step towards reliable CT-based CMS measurements, since standardisation contributes towards creating trust in measurement technologies. In this context, the concepts of acceptance and reverification testing are the most accepted and relevant test procedures for performance verification of CMSs. As this

thesis tries to improve the trust of multi-material CT measurements through acceptance testing, a detailed description of the concepts and principles of this kind of test is given.

2.3.1 Acceptance and reverification testing for (CT-based) CMS

When a new CMS is purchased, the buying decision is, to a large extent, based on the system specifications. Important figures related to the system specifications are the so-called maximum permissible errors (MPEs). The manufacturer provides MPE statements, verified or falsified using test measurements, carried out under well-defined rated operating conditions. The test measurements provide information on the system performance for various metrological characteristics. The set of test measurements with which the standardised characteristics are assessed and tested against the specified MPE limits are called acceptance and reverification tests.

The technical content of acceptance and reverification testing is usually identical. Acceptance testing is normally performed when a new system is first bought, delivered and installed to check if the CMS performs according to the manufacturer's specifications. Reverification tests are usually performed at regular time intervals to confirm if the system still performs within specification. It may also be carried out after a significant change or an unexpected event, e.g. system collision. If applicable, reverification tests can be simpler than acceptance tests and they may use different specifications. From the legal and economic aspects, some warranty issues can be clarified by the acceptance test results.

Acceptance and reverification testing enable technical-based decision-making. Besides this, it allows a systematic checking and reviewing of the records of the CMS performance over time. It allows comparisons between different CT-based CMSs or even between CMSs with different sensors (e.g. CT and tactile). Lastly, some aspects of traceability are covered by acceptance testing principles, however, to a limited extent, since acceptance testing provides traceability to the metre only for the tested characteristics. A CMS which has been proven by an acceptance test — to operate according to the manufacturer given specifications — cannot be declared to provide traceable measurements for tasks other than the ones which are tested by the acceptance test. Furthermore, the test samples the performance only on an internationally agreed level. For example, the test of tactile CMSs is based on a sampling of 105 lengths, while a tactile CMS can measure an infinite number of lengths within its measurement volume.

The most relevant document of acceptance testing for CMS is the ISO 10360 series of international standards. Terminology, principles, concepts, rated operating conditions, metrological characteristics and procedures for testing CMSs equipped with different sensors

are addressed in this normative document. Originally designed to test tactile systems, so far only standards for testing tactile and optical sensors and laser trackers have been published e.g. [72–74]. Part 10360-11 dedicated to CMSs using CT for mono-material measurements, is currently under development and reached the status of second committee draft (CD) in mid-2019 [7,55]. Multi-material measurements are, at present, outside the scope of the acceptance testing developments for CT-based CMS.

According to the ISO 10360 series, the acceptance testing is to perform an overall test of the entire performance of the CMS, where all dominant error behaviour of the CMS should be included. The CMS shall be evaluated as an integrated system comprising every step of the measurement workflow. The test measurements shall reflect the standard use of the CMS and real-life effects should therefore be considered in the test design. However, the application of real-life workpieces is limited in the scope of acceptance testing. Their complexity and variability can impede comparisons between CMSs. For instance, a feature of a real-life workpiece, which can be measured by CT, must be also calibrated, which usually requires tactile probing. Thus, internal features must be also physically accessible, e.g. measurement of the disassembled assembly.

All metrological quantities should be tested complying with all rated operating conditions. These conditions are normally specified by the manufacturer. The specification is therefore only valid if the test is carried out under the predefined rated operating conditions. Examples of rated operating conditions include: environmental conditions such as temperature, clamping, surface properties of the reference standard, measurement time, materials, maximum X-ray penetration length, etc.

In the ISO 10360 standard, the most common and well-established metrological characteristics to be assessed are based on local (Probing errors P) and global performance (Length measurement errors E) of a CMS. Recently, metrological structural resolution has also gained importance as a meaningful characteristic for CT specification, due to its contribution of revealing important measurement characteristics of a CT-based CMS, e.g. the use of data filtering during the test. Some proposals for evaluating structural metrological resolution for CT were developed and presented in [75–79].

Probing error test

The local performance of a CMS according to the ISO 10360 is assessed by the probing error test (P -test). The main objective of the P -test is to assess the three-dimensional error behaviour of the CT-based CMS inside a small part of the entire measurement volume. In another words, the P -test assesses the ability of the system to precisely locate and measure the localised point coordinate on the surface of a structure under test within a small

measurement volume of the entire system. In general, the P -test result is determined by the errors related to the probing system, for the case of tactile systems, or related to the sensor of the CMS, e.g. noise, digitalisation error, geometry-dependent interactions with the reference standard, and it is — for the case of CT — largely influenced by the material-dependent interaction with the X-ray radiation [80].

The probing error test is performed by measuring the size and form of a test sphere representing a small portion of the measurement volume. According to guideline VDI/VDE 2630-1.3 [80], the test sphere should preferably have a diameter from 0.1 to 0.2 times the diagonal of the measurement volume.

Several metrological quantities are being discussed for the realisation of the P -test in the ISO 10360 series part -11 for CT [7]. These are based on the developments in the ISO 10360-8 standard for CMSs with optical distance sensors [73]. For form analysis, probing dispersion error and probing error form are under consideration; and for analysis of size, probing error size all and probing size error. A detailed description of these four quantities is given follows:

1. **Probing dispersion error ($P_{\text{Form.Sph.D95\%::CT}}$)**, the smallest possible width of all spherical shells that contains 95% of all data points, see Fig. 2.22-a.
2. **Probing error form ($P_{\text{Form.Sph.1x25::CT}}$)**, the error of indication within the range of the Gaussian radial distance determined by an unconstrained least-square fit of 25 representative points on a test sphere, see Fig. 2.22-b.
3. **Probing error size All ($P_{\text{Size.Sph.All::CT}}$)**, the difference of the diameter of an unconstrained least-square fit of all points measured on a sphere and its calibrated diameter, see Fig. 2.22-a.
4. **Probing size error ($P_{\text{Size.Sph.1x25::CT}}$)**, the error of indication of the difference between the diameter of an unconstrained least-square fit of 25 representative points on a test sphere and its calibrated diameter, see Fig. 2.22-b.

The above notation – in brackets – for the P -characteristics is derived from the current evolution of standards in ISO 10360 (particularly ISO 10360-8 [73]). It is in part described in [7], but is still under development. There is no guarantee that the quantities and the notation used here will be fully implemented in a first ISO 10360-11. The same applies to the tests themselves. The final ISO 10360 P -tests for CT-based CMSs may differ from the above draft statements.

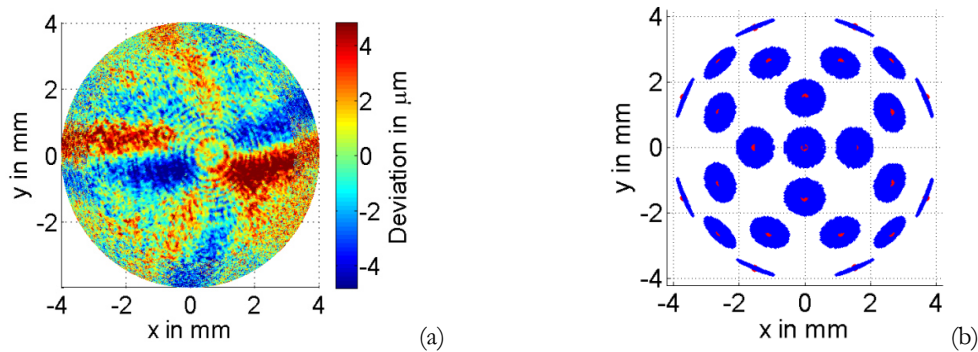


Fig. 2.22. Probing error test with a test sphere — many points are evaluated. (a) Coloured error map of a sphere fit to the measured sphere data. Probing dispersion error using 95% of the points, and probing size error All using all data points are deduced. (b) Probing error size and form evaluation using 25 representative points (shown in red) based on 25 patches (blue) as a subset of all probed points (source: adapted from [81]).

For probing form error and probing size error, the geometric primitive (sphere) is created from a least-square fit of 25 representative points on the test sphere. The representative points are calculated from small regions of the surface, each assessing the local surface within a limited region of the test sphere. Representative points may be deduced from multiple data points inside an extended area — referred to as a patch. This approach — first introduced in the ISO 10360-8 for testing optical distance sensors [73] — improves comparability between measurement technologies and produce more stable results when measuring lengths due to the reduced influence of the sensor noise. Furthermore, the patch approach improves comparability between CMSs with different sensor technologies, mainly due to the high density of points obtained by CT and to morphological filters intrinsic to e.g. tactile probes. On the other hand, the use of patches itself introduces a low pass filtering behaviour and may hide potentially relevant local effects of the system.

As yet, in the current international standard ISO 10360-8 for coordinate measuring machine (CMM) with optical distance sensors, some unsolved issues remain such as the patch geometry, being described in a non-satisfactory way. There is, for example, a constraint that the patch areas must not overlap. However, a well-defined procedure on how to assess these characteristics in CT has not been fully established yet and it is required to create an accepted testing scheme. This “uncertainty” has to be kept in mind when considering potential patch operators in, among others, the multi-material acceptance tests.

Length measurement error test

The underlying concept of the length measurement error test is the evaluation of the three-dimensional error behaviour of the CMS, as represented by a large part of the entire measurement volume. This error behaviour arises from several superposed errors e.g. hysteresis effects stemming from the movement of (different) mechanical axis, random and uncorrected systematic errors. In CT based-CMS, the value of the length measurement errors

is also largely determined by the sensor errors and by the X-ray attenuation properties of the material(s) [80].

The global performance is assessed as a length measurement error test (E -test) through measurement of (long) length reference standards. The E -test describes the three-dimensional error behaviour of a CMS across the entire measurement volume. Examples of length reference standards used to assess the E -test are shown in Fig. 2.23.

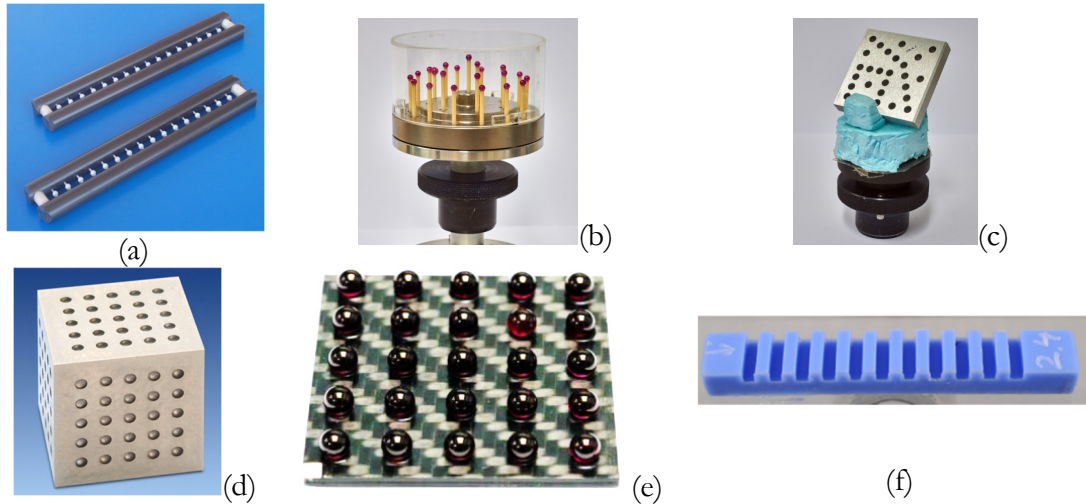


Fig. 2.23. Examples of length standards suitable for CT: (a) ball rail [82], (b) multi-sphere standard [55], (c) hole plate [55], (d) calotte cube [83], (e) ball plate [84], (f) miniature step gauge [85].

Length measurements can be evaluated as bi-, unidirectional or volumetric length measurements, see Fig. 2.24. The difference between unidirectional and bidirectional measurements is the probing direction when measuring a point-to-point distance. A bidirectional length is obtained when both arrows creating a length are pointing to opposite directions as shown by the arrows in Fig. 2.24 (right). When both arrows creating a length are pointing in the same direction, this characterises a unidirectional measurement. In CT, where there is no actual probing, the probing direction is defined by the surface normal of the workpiece. Additionally, the length can be also calculated by the centre-to-centre distance of two fitted elements. Suitable geometric elements such as circles or spheres, are fitted to several points, usually using a least-square method. However, the unidirectional and centre-to-centre length measurements do not entirely reveal local errors of the systems. For example, the surface determination influence and beam hardening influence on CT measurements are not included or included to a very limited extend in the centre-to-centre measurements. This limitation is due to the massive data averaging that occurs when creating the elements.

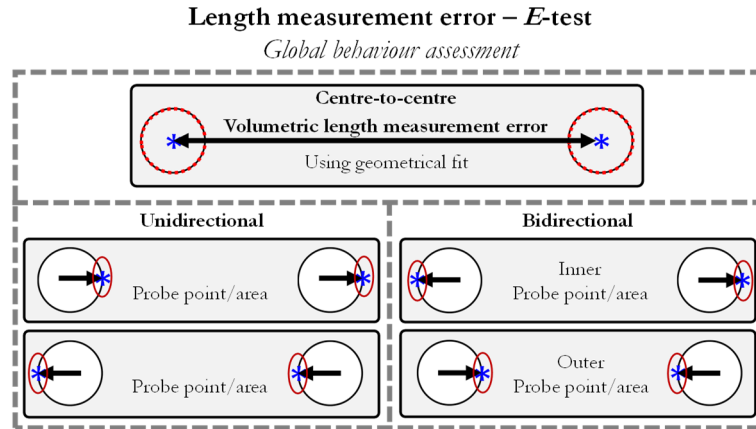


Fig. 2.24. Length measurement error when assessing the global error performance characteristic of a CMS (source: adapted from [13]).

With the point-wise length measurement approaches, uni- or bidirectional lengths may be calculated using patch operators to create representative points, similarly to the probing form error and probing size error analyses.

An overview comparing different length measurement methods regarding their ability to detect effects or error is given in Table 2.1.

Table 2.1. Detected effects/errors by different length measurement methods: bi-, unidirectional and centre-to-centre.

	Bidirectional	Unidirectional	Centre-to-centre
Scale error	✓	✓	✓
Beam hardening (local surface offsets)	✓	□	✗
Surface determination	✓	✗	✗
Noisy data/ scattering	✓	□	✗
Temperature induced errors	✓	✓	✓

Legend: ✓ → effect/error fully detected
 → effect/error partially detected depending how strong the error appears
 → effect/error not or poorly detected

The basic *E*- characteristics under discussion to be assessed in the ISO 10360-11 are:

1. **Bidirectional length measurement error** ($E_{Bi:CT}$), error of indication when bidirectionally measuring a calibrated test length; according to Fig. 2.24. This can be an inner or an outer test length.
2. **Unidirectional length measurement error** ($E_{Uni:CT}$), error of indication when unidirectionally measuring a calibrated test length; according to Fig. 2.24. This can be an inner or an outer test length.
3. **Volumetric length measurement error** ($E_{MVol:CT}$), error of indication when measuring a calibrated test length where the error is deduced from the distance between

two averaged representative points each created from multiple measurement points at two respective geometrical elements.

Related research

Since CT was introduced as an alternative solution of coordinate measurement systems, several studies have been performed to verify and test metrological CT characteristics.

Bartscher et al. 2010 [86] applied a new dismountable traceable reference standard with internal geometries and sculptured surfaces for the analysis of the dimensional performance of CT. The conclusion was that reference objects (block size 120 mm x 90 mm x 60 mm) similar to the workpiece can be used as sensitive tools for verifying the entire measurement process of CT measurements of a given product, additional to the standard test.

Carmignato et al. 2009 [87] presented a test procedure to evaluate the length measurement error of CT using a reference standard made from glass fibres featuring a regular array of inner and outer cylinders (a fibre gauge standard). The cylindrical shaft and the holes have diameter of 120 μm and 250 μm , respectively. The experimental results showed that the reference standard was suitable for determining the length measurement error as well as for compensating residual scale errors of the system.

Cantatore et al 2011 [85] verified the CT performance in accordance with the VDI/VDE 2617-6.2 guideline using a miniature step gauge (42 mm long), originally developed to test optical measurement systems. The study evaluated object orientation, magnification and surface extraction methods. The experimental results showed that an optimal orientation of the workpiece on the rotary stage is important to enhance the reliability of the measurements.

Müller et al. 2012 [84] developed a new reference standard (a CT ball plate standard) for evaluating the metrological performance of CT systems. The standard appears to be a valid solution for the length measurement error test.

Angel et al. 2015 [88] studied the length measurement performance of CT systems using statistical methodologies on step gauge standards made of different materials, focusing on the influence of the material and object orientation. The main effect observed in the study was that the measurement errors were affected by X-ray scattering and therefore material-dependent.

Léonard et al. 2014 [89] presented a method of performance verification for CT systems based on a tetrahedron made of 4 alumina spheres. The results showed that the reference offers a simple versatile solution for assessing CT systems.

Borges de Oliveira et al. 2015 [81] investigated the performance of a combined probing- and length measurement-error tests for the acceptance testing of CT-based CMS using two

different standards. In general, the authors do not recommend the performance of the combined test.

Hiller et al. 2010 [90] compared the results of the probing error test using circular and helical scanning trajectories. Shi et al. [91] assessed the probing error of a CT-based CMS. Similarly, *Andreasen et al. 2019* [92] investigated experimentally the influence of the probing errors on the form measurements of an industrial CT.

Bartscher et al. 2016 [55] carried out a study survey on the material influence on the length measurement error test. The authors highlighted the importance of selecting appropriate standards for the performance of acceptance tests.

Bartscher et al. 2014 [7] published an overview of the current status of standardisation activities for CT in the world.

2.3.2 Decision-making and attributed uncertainty

Commonly, coordinate measurement systems are specified by the manufacturer based on MPE values. The MPEs are specified for each tested system characteristic and represent a range of measured values, for which the system is declared to be in conformance with the specification. When performing an acceptance test, the tester carries out the test measurements — i.e. the measurement of reference standard(s) and acquisition of measurement value(s). The test measurements must be carried out under the specified rated operating conditions, describing e.g. temperature range, maximum material penetration length, etc. allowed in the test. The results of the test measurements are then compared with the MPE values specified by the manufacturer. If a result (i.e. measured test quantity) lies within the range (for the of E -test and P_{Size}) or below the maximum specified value (for P_{Form}) — e.g. in the middle or close to zero depending on the parameter — the respective maximum permissible error, the CMS can most likely be declared to conform to the specifications of that test characteristic. However, if the measured test quantity lies within the MPE range, but close to its limits, the decision of conformance or non-conformance becomes unreliable, because the test measurement is imperfect and has an associated uncertainty. The decision of conformance and non-conformance of a test measurement result is described in the ISO 14253-1 [93].

The test-associated uncertainty is called test value uncertainty and the concepts are described in the ISO 14253-5:2015 [94] international standard, ISO/TS 17865:2016-08 [95] and ISO/TS 23165:2006 [96] international technical specifications. The test value uncertainty approach aims to evaluate the expanded uncertainty of a test associated solely with the testing equipment and its use in that test. Normally, uncertainty contributors part of the test value

uncertainty are the influencing factors, which the tester is responsible for. These concepts are commonly applied to decision-making when performing acceptance testing of CMSs in accordance to e.g. ISO 10360-2, -5 and -8. Since every possible effect potentially influencing the test is considered and quantified as an uncertainty contributor, the test uncertainty expresses how accurate the testing process, as performed by the tester, is.

2.4 Summary and conclusions of the chapter

The measurement workflow of cone-beam CT-based CMSs starts with acquisition of the radiographic images in different angular orientations of the workpiece. The manipulator system places the workpiece between X-ray source and detector and rotates it during the scan. The X-ray images are acquired by the X-ray detector, where the radiation is transformed into a digital signal. The digitalised images are then reconstructed, which results in a 3D representation of the workpiece. The reconstructed image consists of a 3D matrix, where each element, represents the local density of the workpiece, and is expressed in grey levels. The virtual surface of the scanned workpiece is determined based on the grey value behaviour of the dataset. The holistic approach of CT allows a great variety of measurement possibilities. For example, the measurement can be carried out based on the feature extraction of geometrical primitives (based on points acquired on the workpiece's surface), or based on the entire measured workpiece, where the determined surface is compared with e.g. its mathematical model (CAD).

The relevant influencing factors and their effects on CT measurements were gathered and interpreted to multi-material measurements. Table 2.2 summarises the influencing factors considered relevant for multi-material measurements and their impact on the physical effects.

Table 2.2. Overview of the relevant influencing factors and their effects to multi-material measurements.

	Beam hardening	Scattering	Photon starvation	Partial volume	Noise	Detector sensitivity	Detector absorption depth	Detector response curve	Surface offsets
X-ray radiation									
Voltage	⊗	⊗	⊗	⊗		⊗	⊗	⊗	⊗
Filter	⊗	⊗	⊗	⊗	⊗	⊗	⊗	⊗	⊗
Target material	⊗	⊗			⊗				
WP									
Material	⊗	⊗	⊗	⊗	⊗	⊗	⊗	⊗	⊗
Thickness	⊗	⊗	⊗	⊗	⊗	⊗	⊗	⊗	⊗
Detector									
Scintillator material						⊗	⊗	⊗	
Scintillator thickness					⊗	⊗	⊗	⊗	
Reconstruction									
Algorithm	⊗				⊗				
Filter (for FBP)	⊗				⊗				
Surface determination									
Algorithm									⊗
Search distance									⊗
Threshold									⊗

The principles of acceptance testing for the performance verification of CMSs are based on the probing error (P) and length measurement error (E) tests. Metrological characteristics — for P and E — shall be evaluated by means of test measurements on appropriate reference standards. The test measurements shall be carried out under specified, rated operating conditions. The results of the test measurements shall be compared with the system specifications, provided by the manufacturer, and a decision of conformance and non-conformance — supported by the test value uncertainty — is taken.

Lastly, four main issues were identified in the previous chapters, representing the necessity and a growing interest of CT manufacturers and users alike for the creation of acceptance testing dedicated to multi-material measurements: (a) a growing number of multi-material workpieces in industry and the demand of quality control of such workpieces/assemblies, (b) the lack of traceable and systematic methods for the performance assessment of multi-material measurements with CT-based CMS; (c) the absence of standards and technical guidelines for multi-material measurements; and (d) the not fully understood multi-material induced physical effects on the measurement, hindering reliability of multi-material CT measurements. Therefore, a multi-material acceptance test is proposed.

2.4. Summary and conclusions of the chapter

This proposal is designed to fulfil the abovementioned needs, providing an approach to verify the performance of CT-based CMSs when measuring multi-material workpieces considering scientific as well as economic aspects.

Chapter 3: Proposal for a multi-material acceptance test for X-ray CT systems

In light of the context of CT in the industrial and standardisation scenarios presented in the previous sections, the increasing interest of CT users and manufacturers in a systematic and standardised method for evaluating the performance of CT-based CMSs for multi-material measurements, was the main motivation for the development of this thesis.

The creation of a multi-material acceptance test for CT is divided into conceptual and verification phases, see Fig. 3.1. In the conceptual stage, input and knowledge from existing standards and current discussion in standardisation committees and two scientific branches (CT physics and metrology) were used to develop the framework of the proposed test. The verification of the test proposal was carried out executing representative multi-material measurements using novel calibrated reference standards.

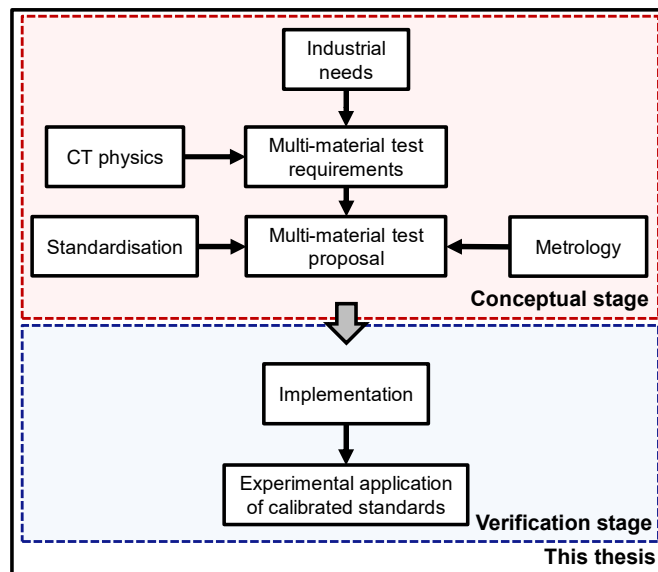


Fig. 3.1. Workflow of the creation of the multi-material acceptance testing.

3.1 Multi-material acceptance test requirements

The establishment of the test design requirements based on the identified needs and on current standards is the first step towards developing the multi-material acceptance test. Thus, the multi-material acceptance test should:

3.1. Multi-material acceptance test requirements

- follow the main concepts described in the ISO 10360 series of standards for acceptance testing of CMSs, either adapting them or creating new concepts where necessary
 - provide traceability to the SI-units with low test value uncertainty (ISO/TS 23165 [96] and ISO 14253-5 [94])
 - provide comparability with other CMSs, even with different sensors
 - provide specification requirements considering the specifics of multi-material CT measurements
- evaluate global (*E*-test) and local (*P*-test) performance characteristics of the CT-based CMS for multi-material measurements
 - demonstrate, for dominant effects related to multi-materials, the sensitivity of probing error (*P*-) and length measurement error (*E*-) tests
 - provide specification statements related to multi-materials, e.g. material combination
 - complement the standard mono-material test and be as efficient as possible while avoiding redundancy with the standard mono-material test
- operational requirements
 - be as simple as possible and easy to understand
 - limit costs to support industrial dissemination and use

According to ISO 10360 concepts, the main objectives of acceptance tests are to provide a metrological and systematic approach for verifying the performance of a measurement system and to allow comparisons between CMSs. In the proposed MuMat test, these concepts are extended to multi-material measurements, that is the test is to assess the capability of a CT-based CMS of measuring multi-material objects.

The reason for following the principles in ISO 10360 series of standards is that they are well-established in coordinate metrology and they provide task-specific traceability and comparability between CMSs. Nevertheless, due to the different measurement principles of different CMSs, e.g. CT- and tactile-based CMSs, not all concepts can be directly applied to CT technology. Therefore, test concepts should be adapted, or new concepts should be created to suit this new application.

The development of an international standard for verifying the performance of CT-based CMSs has already started, see § 2.3.1. Thus, the proposed MuMat-test should be complementary to the in-progress (mono-material) test, and not substitute it. Considering this, the multi-material test focuses specifically on the assessment of systematic multi-

material effects and is not intended to sample the error behaviour covered by the mono-material test. Additionally, the acceptance test should be as efficient as possible, avoiding unnecessary effort and costs.

The proposed test shall demonstrate the dependency of multi-material effects on the local and global performances of the system by means of test measurements with calibrated standards, executed under specified, rated operating conditions. In short, the test shall be able to disclose the dominant multi-material error behaviour of a CT-based CMS.

The high degree of complexity and many different possibilities of multi-material measurements regarding e.g. combination of materials, measurement situation and scenarios, demands a set of requirements (rated operating conditions) tailored to multi-material measurements. As a consequence, if the rated operating conditions are not stated, the system specification, e.g. the MPE for the multi-material characteristic, would be universally valid. As this statement is both impractical and unrealistic, the proposed test should provide specification requirements considering the specifics of multi-material measurements with regard to probing error and length measurement error tests.

To encourage industrial, scientific and standardisation dissemination, the MuMat acceptance test should be as simple as possible and easy to understand. Lastly, the reference standards shall be possible to calibrate, easy to use and stable. Thus, the proposal of a multi-material acceptance test based on the abovementioned requirements is presented.

3.2 Proposal for a multi-material acceptance test

This work aims to provide directions for the performance verification of CT-based CMS according to concepts of acceptance and reverification testing for multi-material measurements.

The following sections present the general test concepts and the specification requirements with regard to multi-material CT measurements, as well as the proposals for the multi-material *P*- and *E*-tests.

3.2.1 General multi-material acceptance testing concepts

This proposal serves to evaluate the metrological performance of CMSs using X-ray CT as the single sensor for multi-material measurements, where the signal is entirely based on absorption contrast. The test is designed to assess CT systems featuring at least one rotary axis, an X-ray source and an X-ray detector. Medical imaging CT, native non-destructive CT as well as non-X-ray CT systems, e.g. Neutron or THz-CT, were excluded from the scope of this test. The proposed test is not limited only to a circular scanning trajectory. This test

3.2. Proposal for a multi-material acceptance test

proposal can in principle be applied to evaluate the multi-material performance of CTs, which use special scanning trajectories (e.g. helical, line-circle). Since, it is assumed that the multi-material effects are originated from the physical interactions between X-ray radiation and matter and are not significantly influenced by the scanning trajectory. However, only test measurements using circular trajectory were carried out in the scope of this thesis.

The assessment of local and global performance of a CMS are concepts used in the mono-material test and should be adopted in the multi-material test concepts, through the evaluation of the probing error test (P) and length measurement error test (E). These characteristics are to be assessed by test measurements of novel multi-material reference standards or multi-material test scenarios under specified conditions.

From the manufacturer's point of view, statements related to the system performance (e.g. MPE values) are made or falsified based on the test measurement results. From the user's perspective, the results of the multi-material test measurements are to be compared to the numbers related to the system specification.

For this document, a multi-material reference standard is defined, as a technical, calibrated workpiece — with known dimensions and geometry — made of two or more materials (excluding air). The materials of the MuMat standard must have different X-ray attenuation coefficients, and significant influence on the measurement by substantial attenuation of the X-ray radiation. Besides this, during the CT scan the total X-ray penetration lengths must include both materials for a defined number of X-ray paths, and dimensional and/or geometrical measurements are carried out in at least one material.

A multi-material test scenario is defined as a set-up where two or more objects made of different materials are used to perform the test measurements, and dimensional or geometrical measurements are carried out on at least one object (hence at least one object must be a reference standard and the other object serves as an obstructive body). The materials of the MuMat test scenario must have different X-ray attenuation coefficients, and significant influence on the measurement by substantial attenuation of the X-ray radiation. Besides this, during the scan the total X-ray penetration lengths must consist of both materials for a defined amount of X-ray paths.

Note: X-ray attenuation is considered to be substantial, when the material — being irradiated alone — absorbs at least 15% of the X-ray radiation going through it (i.e. less than 85% X-ray transmission) in the given set-up (i.e. material, geometry and X-ray spectrum).

Material combination for the multi-material acceptance testing

The multi-material test shall be carried out using either a MuMat standard or a MuMat measurement scenario. Statements defining the material combination, which the system is

specified, associated to the material attenuation coefficients, are required. These statements must define material (or class thereof) and how different the materials included in the MuMat test have to be.

This work proposes two (possible) definitions to describe the difference between attenuation coefficients: a simplified and a more detailed definition of the material ratio in a MuMat standard. The simple definition is based on the attenuation coefficient ratio for a specific spectrum energy, according to Eq. (3.1). The more complex definition, which is presented in Eq. (3.3), considers the entire attenuation curve and polychromatic spectrum in a defined energetic interval.

However, the attenuation coefficient ratio can partially define the combination of the materials of the MuMat acceptance test. To complete it, a specification related to the absolute X-ray attenuation (considering the tested materials) is necessary. This specification is intended to avoid, that e.g. high absorbing materials (e.g. Fe) being paired with moderate absorbing material (e.g. Al) have the same specification as moderate absorbing materials being combined with low absorbing materials (e.g. plastics). This MuMat characteristic can be determined by material classes or based on the absolute attenuation coefficient, e.g. by calculating the average of the attenuation coefficients of the materials for a single spectral energy or a range of energies, according to Eq. (3.2) and (3.4), respectively.

There is some indication that the developing ISO mono-material test for CT-based CMS will determine a material classification based on at least three material classes, they are: plastics-like materials, aluminium-like materials and iron-like materials (excluding alloys with materials featuring extremely high attenuation coefficient, e.g. lead, tungsten). However, this classification is incomplete, since some materials important to industry (e.g. Ti and some types of optical glasses) are not included.

$$R_{\mu_B/\mu_A} = \frac{\mu_B(E)}{\mu_A(E)} \quad \text{for } \left\{ \begin{array}{l} \mu_A > \mu_B, \\ E \in \{0, \dots, E_{max}\} \end{array} \right\} \quad (3.1)$$

$$\bar{\mu}_{\mu_A \& \mu_B} = \frac{\mu_A(E) + \mu_B(E)}{2} \quad \text{for } \left\{ \begin{array}{l} \mu_A > \mu_B, \\ E \in \{0, \dots, E_{max}\} \end{array} \right\} \quad (3.2)$$

$$R_{\mu_B/\mu_A} = \frac{\int_0^{E_{max}} I_0(E) e^{-\mu_B(E)x} dE}{\int_0^{E_{max}} I_0(E) e^{-\mu_A(E)x} dE} \quad \text{for } \mu_A > \mu_B \quad (3.3)$$

3.2. Proposal for a multi-material acceptance test

$$\bar{\mu}_{\mu_A \& \mu_B} = \frac{\int_0^{E_{max}} I_0(E) e^{-\mu_B(E)x} dE}{\int_0^{E_{max}} I_0(E) dE} + \frac{\int_0^{E_{max}} I_0(E) e^{-\mu_A(E)x} dE}{\int_0^{E_{max}} I_0(E) dE} \quad \text{for } \mu_A > \mu_B \quad (3.4)$$

Where R_{μ_B/μ_A} and $\bar{\mu}_{\mu_A \& \mu_B}$ are the attenuation coefficient ratio and average between material ‘‘A’’ and ‘‘B’’, respectively; μ_A and μ_B are the attenuation coefficients of material ‘‘B’’ and ‘‘A’’, respectively; E is the spectrum energy and I_0 is the incident intensity.

A classification of attenuation coefficient ratios of multi-material assemblies is presented in Table 3.1. The attenuation coefficient ratios can be calculated with Eq. (3.1) and (3.3). High attenuation coefficient ratios (i.e. close to one) show that the materials have similar X-ray attenuation, whereas low attenuation coefficient ratios (i.e. close to zero), indicates rather different X-ray attenuation coefficients.

Table 3.1. Classification of the attenuation coefficient scenarios.

Low	$0 < \mu_B \leq 0.2 \mu_A$
Low-moderate	$0.2 \mu_A < \mu_B \leq 0.4 \mu_A$
Moderate	$0.4 \mu_A < \mu_B \leq 0.6 \mu_A$
Moderate-high	$0.6 \mu_A < \mu_B \leq 0.8 \mu_A$
High	$0.8 \mu_A < \mu_B \leq 1 \mu_A$

Multi-material measurement situation

There are three measurement situations possible to be carried out in a multi-material test scenario or multi-material standard. The measurement situations rely on the multi-material influence, on the material interface and on the creation of the measurand. This classification aims to provide a better overview of the material influence on the MuMat measurements by separating these situations.

Thus, three measurement situations are considered: mono-material measurements, inter-material measurements and in-material measurements, see Fig. 3.2.

A measurement is classified as **mono-material**, when the interface between the geometric elements creating a measurand (e.g. distance between circles) consists of one single material and air; and the total X-ray penetration lengths are attenuated only by a single material and no other material significantly influences the measurement (by attenuation of the X-ray radiation), see Fig. 3.2-left.

A measurement is classified as **inter-material**, when the X-ray radiation is significantly attenuated by two or more materials (excluding air), when two geometric elements

composing a measurand are created in different materials, and they are interfaced with air, see Fig. 3.2-centre.

A measurement is classified as **in-material**, when the geometric elements used for the measurement are created in one single material, yet the measurement of the geometric elements is significantly influenced by more than one material (i.e. the X-ray radiation is significantly attenuated by two or more materials, see Fig. 3.2-right).

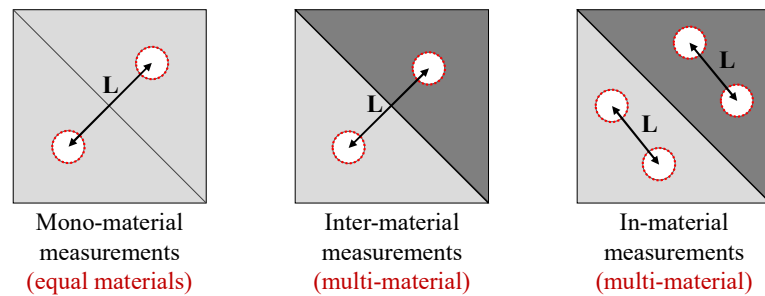


Fig. 3.2. Measurement situations: (left) mono-material scenario (creation of the elements for the measurand based on material A and air, material A and air, no material B present); inter-material measurements in multi-material scenario (creation of the elements for the measurand based on material A and air, material B and air); in-material measurements in a multi-material scenario (creation of the elements for the measurand based on material A and air, material A and air, however, material B is part of the penetration length).

Although the proposed MuMat acceptance test exclusively covers measurands created from geometrical elements interfaced with air, other measurement scenarios are possible, e.g. when the material interface consists of two different materials (e.g. material A and material B) (application example: mechanical limits, fits and tolerances). This type of measurand is strategically out of the proposed MuMat test scope, since it is incompatible with tactile and often even optical reference measurements of the standard, which subsequently impairs the comparability, applicability and traceability of the test. Also, this measurand type characterises an unusual test scenario when compared to the other parts in the ISO 10360 test, where reference standards are only interfaced with air.

3.2.2 Specification requirements related to multi-material measurements

A general requirement of the ISO 10360 standards is that, in order to be considered valid test measurements, all specifications shall be fulfilled. This implies that the MPE shall be guaranteed only if the rated operating conditions are met. The manufacturer is responsible for providing MPE values and specification requirements, including rated operating conditions to be complied with test measurements. If no specification is provided, the CMS is specified for every test condition. This would mean that the tester is free to choose scanning parameters, material combinations, etc. to perform the test measurements, and the MPE would still be guaranteed in every case.

Therefore, the specification shall include the full set of parameters, settings and conditions required to test and achieve the specified performance. Information are either required to operate the CMS (e.g. environmental conditions, workpiece loading effects, measurement time etc.) or to process the data (e.g. evaluation software and version) shall be included in the specification. All basic requirements for specifications are already included in the ISO 10360 series of standards and they are expected to be included in the upcoming acceptance test for CT-based CMS. The specification requirements described in the mono-material acceptance test for CT shall also be followed in this test proposal, unless stated otherwise. However, specification statements considering multi-material measurements are not included in the future standard. Therefore, this thesis focuses on specification statements relevant when performing multi-material test measurements.

Specification related to multi-material situations

In principle, it is possible to obtain mono-material measurements in multi-material standards or test scenarios. However, the multi-material performance of a CT-based CMS can be fully tested, when in- and inter-material measurement situation are carried out. Therefore, for the MuMat probing error test, in-material measurement situation is mandatory. Since form and size measurements in inter-material situations are severely impaired by measurement equipment design, an additional data correction is usually required. For the MuMat length measurement error test, inter-material measurements are mandatory to ensure all relevant MuMat effects are included in the test.

Statements related to the multi-material situation are mandatory. An example of such statement might be the following: the system is specified for the MuMat length measurement error test based on the measurement of 108 lengths, where at least 20% of the measured lengths shall characterise inter-material measurements. For the MuMat probing error test, the system is specified based on form and size measured in in-material situations.

Specifications for the selection of the scanning and post-processing parameters

The set of scanning parameters, with which *P*- and *E*-test measurements shall be carried out, shall be specified. The specified MPEs are only guaranteed if the test measurements are carried out in conformance with the specified scanning parameters.

The multi-material error characteristic of a CT strongly depends on physical interactions between X-ray radiation and material attenuation behaviour. Post-processing steps can also have significant influence on the measurement results. Thus, the scanning parameters important to multi-material measurements and considered in this thesis are:

- Parameters related to X-ray spectrum

- Post-processing parameters related to surface determination and correction methods

The *X-ray spectrum-related parameters* have a strong impact on the multi-material measurement results, given the nature of the multi-material effects. Thus, X-ray voltage and beam-filter material and thickness must be specified. This specification aims to provide fair test scenarios by defining a minimum amount of X-rays going through the materials in a single projection (considering also the energetic restrictions of the system). Due to the potential asymmetry of the MuMat reference standard or test scenario, the maximum number of projections, for which the minimum X-ray transmission may be exceeded (e.g. exceeding the dynamic range of the detector), should be stated as well. The X-ray transmission should be measured in relation to the free X-ray beam.

When specifying a CT-based CMS for e.g. moderate attenuation coefficient ratios (see Table 3.1), general recommendation is to select the X-ray parameters in such a way as to guarantee an X-ray transmission of at least 10% relative to the free-beam (before detector gain qualification) for at least 90% of the 2D projections of a CT scan conducted as part of the MuMat acceptance test.

Also, some *post-processing parameters* such as methods for determining the surface of the measured object and multi-material-related correction methods can significantly influence multi-material measurement results. Thus, a detailed description of the post-processing parameters used is required. In state-of-the-art software for data analysis, the capability for simultaneously finding surfaces of different materials depends mainly on the attenuation coefficient ratio between the materials of the MuMat object, as discussed in §2.2.1. Therefore, if specialised procedures for finding the surface of multi-material datasets are used in the test, they should be described in detail. Besides that, data correction or filtering is only allowed in the multi-material test, if they are implemented in the CT system evaluation and data processing packages. When external tools are used, a complete description of the data processing parameters used for the test measurements are once again required and must be agreed upon beforehand.

Specification related to material combination

The combination of materials to be used to test a CMS shall be specified by the manufacturer as well. The specification statement shall include the materials to be used in the MuMat test. With alloys, the core element of the alloy shall be stated, see the example of a system specification for a material combination consisting of aluminium and titanium for multi-material *P*- test in Eq. (3.5). The complete description of the materials used in the MuMat test, including, for example, thermal expansion coefficient, material content and density shall be documented and provided to the user.

$$P_{\text{Form.Sph.All.MuMa.Al\&Ti::CT,MPE}} \quad (3.5)$$

The materials used to perform the P - and E -tests are not required to be the same, to allow for the technical restrictions of manufacturing of the reference standards with metrological quality (i.e. it is difficult to find (half) spheres made of certain materials). However, they must have similar multi-material conditions, i.e. same class of attenuation coefficient ratio and similar average.

Material thickness

The MuMat characteristics of a CT-based CMS should be also specified based on the maximum allowed penetration length for each material and for a specified range of X-ray spectrum energy. This specification establishes a maximum material thickness allowed in the test, ensuring e.g. a minimum degree of X-ray transmission, considering both the CT's spectrum energetic limit and attenuation coefficients of materials. Therefore, the range of thicknesses of the materials to be combined shall be specified. Since the X-ray attenuation depends on the X-ray energy, the range of X-ray energies shall also be included in this specification.

The specification can be made for the entire range of material thicknesses or part of it, since the full range of material thickness may be not relevant for all cases. In both cases, it is required to specify the characteristic continuously, and not discretely.

An example specification for a CT-based CMS covering the entire range of material thickness ratios for multi-material pairings made of Fe & Al, and valid for an energy range from 100 keV can be seen in Fig. 3.3.

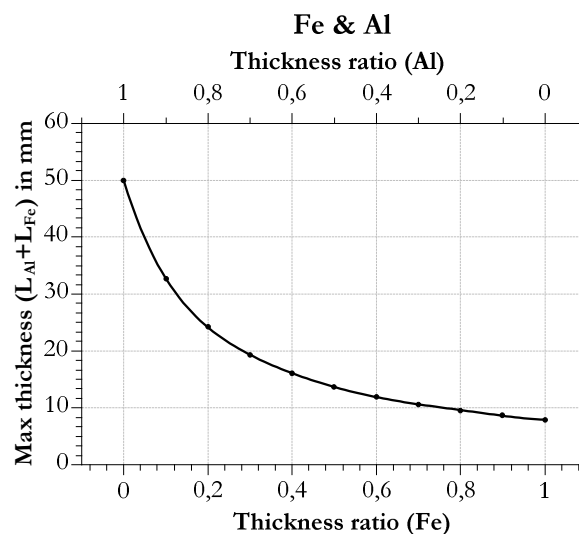


Fig. 3.3. Specification example of maximum material thickness in a MuMat scenario comprising Fe & Al for a CT-based CMS with maximum voltage of 225 kV and valid for an X-ray spectrum energy from 100 keV.

The specification of maximum material thickness in a MuMat scenario presented in Fig. 3.3 is derived from the Lambert-Beer law of attenuation, Eq. (2.1), for an X-ray transmission of 10% for an spectral energy of 100 keV, according to Eq. (3.6).

$$L_{Al} + L_{Fe} = \frac{-\ln(0.1)}{R\mu_{Fe} + (1-R)\mu_{Al}} \quad (3.6)$$

Where $L_{Al} + L_{Fe}$ is the maximum total thickness allowed; R is the thickness ratio; μ_{Al} and μ_{Fe} are the attenuation coefficients of Al and Fe, respectively. They were obtained from the theoretical attenuation coefficient table from [17].

3.2.3 Multi-material probing error test

The main objective of the multi-material P -test is to assess the three-dimensional error behaviour of the CT-based CMS for multi-material measurements within a small section of the entire measurement volume. In general, the P -test result is determined by the errors related to the sensor of the CMS, e.g. noise, digitalisation error, geometry-dependent interactions with the reference standard, and it is — in the case of CT — heavily influenced by the material-dependent interaction with the X-ray radiation [38].

(Suggested) Multi-material probing error geometrical characteristics

The probing error characteristic of a CMS is assessed by form error and size (diameter) measurements to be evaluated on a test sphere. The characteristics — to be measured on the MuMat test spheres or on the MoMat test sphere measured simultaneously with an obstructive body made of different material — are to highlight the MuMat influence during the probing error test. The difficulty to achieve comparability with other CMSs is also addressed with the P -characteristics. Thus, this approach limits the complexity and variety of the measurands — when compared with real-life scenarios. The P -test characteristics suggested in this work are based on the current discussions in international standardisation and the definition of the four metrological quantities to be evaluated is given follows:

1. **Multi-material probing dispersion error ($P_{\text{Form.MuMa.Sph.D95\%::CT}}$)**, the smallest possible width of all spherical shells which contains 95% of all data points measured on the test sphere.
2. **Multi-material probing form error ($P_{\text{Form.MuMa.Sph.1x25::CT}}$)**, the error of indication within the range of the Gaussian radial distance determined by an unconstrained least-square fit of 25 or more representative points (based on patches) on the test sphere.
3. **Multi-material probing size error All ($P_{\text{Size.MuMa.Sph.All::CT}}$)**, the difference of the diameter of an unconstrained least-square fit of all points measured on the test sphere and its calibrated diameter.

4. **Multi-material probing size error ($P_{\text{Size.MuMa.Sph.1x25::CT}}$)**, the error of indication of the difference between the diameter of an unconstrained least-square fit of 25 or more representative points on the test sphere and its calibrated diameter.

Remark on notation: The notation stated above — in brackets — is derived from the current evolution of standards in ISO 10360 (particularly ISO 10360-8). It is partially described in [97] but is constantly being revised.

Measuring equipment for the multi-material probing error test

Reaching maximum comparability with the standard mono-material test, the multi-material P -test requires also a test sphere for the test measurements. However, the proposed test shall be performed on a calibrated compound test sphere consisting of two symmetric half spheres (HS) made of different materials (MuMat sphere) to ensure material influence of both half spheres in the measurement; or in a MuMat P -test scenario, which consists of a calibrated MoMat test sphere to be measured simultaneously with an obstructive body (also a sphere) made of a different material.

If the MuMat P -test is assessed as MuMat test scenario, a solid test sphere shall be made of a material with lower attenuation coefficient than the obstructive body. Moreover, the obstructive body must also have spherical geometry with similar dimensions as the test sphere, ensuring material influence of the obstructive body on the test sphere.

The diameter of the test sphere — as a condition of the test — shall not be larger than 20% of the longest spatial diagonal of the measurement volume for the given geometrical magnification, representing a small portion of the measurement volume. If the obstructive sphere is used, its diameter shall be within $\pm 5\%$ of the MoMat test sphere diameter.

To guarantee traceability in the test, the form and size of the test sphere shall be calibrated. The calibrated form error of the test sphere and its associated uncertainty as well as the uncertainty associated with the calibration of size measurement must be documented, since they have an important role in the evaluation of the test value uncertainty. The form error and the uncertainties associated with form and size measurements are required to be significantly smaller than the specified $P_{\text{MuMa::CT,MPE}}$ of the CMS (maximum 20% of the expected MPE [97]).

The specification of the materials and material thicknesses for the P -test shall comply with the requirements of materials and attenuation coefficient scenarios as well as the material thickness as described in § 3.2.2.

Multi-material probing error test procedure

The test measurements shall be carried out in accordance with the specified rated operating conditions. The results of the test measurements are to be compared with the MPEs.

The MPEs of the multi-material probing characteristics can be specified for each specific multi-material combination (i.e. class of attenuation coefficient ratio and classes of materials). This means that a single CT-based CMS can be specified for several MPEs. The manufacturer is also allowed to specify the system covering a greater range of material combination. However, it then becomes necessary to specify for which material combinations the specification is valid. For instance, a system's multi-material MPE might be valid from high to moderate-low attenuation coefficients ratios for plastic-like with Al-like materials and plastic-like with Ti-like materials.

The MuMat probing error test measurements shall be performed using a MuMat test sphere or a MuMat *P*-test scenario as described in § *Measuring equipment*. The manufacturer shall determine whether the test shall be carried out with a MuMat test sphere or a MuMat test scenario. The MPE shall be maintained only if the test is performed as specified by the manufacturer, i.e. if the manufacturer specifies the system based on measurements with a MuMat test sphere, the MPE is only guaranteed if the test measurements are also carried out using a MuMat test sphere.

If MuMat test spheres are used to perform the test measurements, the test sphere can be placed freely within the measurement volume, as long as a complete scan of the test sphere is guaranteed. A complete scan means, that whole test spheres shall be acquired in all projections. The MPE should be guaranteed in the entire measurement volume.

If a MuMat *P*-test scenario is used to perform the test measurements, the test sphere and the obstructive sphere can be positioned freely. However, the set-up shall be mounted in such way that for several projections (e.g. at least 40% of the projections) the test sphere and the obstructive sphere are simultaneously penetrated by the same X-ray beams. The test and the obstructive spheres must not touch each other, and a distance between 0.5 and 1 test sphere diameter shall be maintained between them. Both test sphere or/and obstructive sphere shall be acquired in their entirety in all projections of the scan.

The MuMat set-up shall be rigidly mounted to minimise errors due to unwanted vibrations and movements during scan. Re-using the same test sphere in previous qualifications steps is strictly prohibited, to avoid doubtful test results created by e.g. correction methods implemented specifically for qualification steps using specific reference standards.

3.2. Proposal for a multi-material acceptance test

The materials and attenuation coefficient ratios used to perform the MuMat *P*-test shall be specified by the manufacturer. The tester is able to use different material than stated in the system specification to perform the test. However, the MPE shall be only guaranteed if the test measurements are carried out using materials within the material class and attenuation coefficient ratio class as the specified materials.

The MuMat *P*-test shall be performed at one geometrical magnification per MuMat test set-up, i.e. material combination. The geometrical magnification shall be chosen so that the test sphere should cover a maximum of 20% of the longest measurement volume diagonal (i.e. at low geometrical magnifications), since the *P*-test evaluates the performance of the system within a small portion of the measurement volume. Besides this, scattered radiation also increases at lower geometrical magnifications, potentially causing a noisier surface and degrading the form of the test sphere. At least three measurement repetitions should be carried out per MuMat *P*-test set-up (i.e. MuMat test sphere or MoMat test sphere plus obstructive sphere made of different material). This is a divergence with the current developments of the ISO standard for CT, which requires test measurements in at least two geometrical magnifications. However, the multi-material effect depending on the geometrical magnification, i.e. noise from scattered radiation, is already included in the low magnification *P*-test measurements.

If more than one test set-up is used (e.g. covering two ranges of attenuation coefficient ratios), the manufacturer shall specify if the MuMat set-ups are to be scanned separately or in a combined scan.

The position and orientation of the MuMat set-up have to ensure a valid and complete measurement of the test sphere (i.e. the complete geometry being tested shall be acquired). The measured area of the MuMat test sphere shall be as large as possible, not in contact with any other material and shall be measured across its entire calibrated surface area. The measurement of the test sphere shall not be affected by the mounting system (e.g. the shaft/support material). At least 50% of the surface of the full sphere (even if not connected) shall be measured.

Finally, the test value uncertainty should be calculated. The uncertainty should be low enough to allow making statements about MuMat effects. The relevant concepts from the international technical specification ISO/TS 23165:2006 should be applied to estimate the test value uncertainty.

The four *P*- metrological characteristics are to be measured and compared with reference values and MPEs provided by the manufacturer.

Multi-material probing dispersion error $P_{\text{Form.MuMa.Sph.D95\%::CT}}$: If a multi-material test sphere is used in the test, data points should be separately acquired on the free surface of each half sphere. It has to be guaranteed that mounting effects and its vicinity, derived from the manufacturing process, have no influence on the measurement. If a multi-material test scenario is used in the test, the data points should be acquired on the free surface of the MoMat test sphere. Based on data points acquired with one half (HS1) of a MuMat test sphere or the MoMat test sphere, fit an unconstrained Gaussian sphere. Determine the smallest possible width of all spherical shells that contain 95% of all data points of the half or MoMat test sphere. Practically this can be realised by an interactive process, where the distances between each data point to the sphere centre is calculated. 5% of the data points with the largest distances to the sphere centre are excluded from the data analysis. The radial width of this spherical shell is the probing dispersion error of half sphere 1 (HS1) or the MoMat test sphere. If a multi-material sphere is used, repeat the procedure in the second half of the MuMat test sphere to obtain the probing dispersion error of HS2. Compare the probing dispersion errors of HS1 and HS2; the highest absolute value is the multi-material probing dispersion error $P_{\text{Form.MuMa.Sph.D95\%::CT}}$.

Multi-material probing form error $P_{\text{Form.MuMa.Sph.1x25::CT}}$: From the raw data points acquired either in one half sphere (HS1) of the MuMat test sphere or in the MoMat test sphere, select 25 patches on one half sphere (HS1) or on the entire solid test sphere, and reduce them to representative points. Calculate a Gaussian associated sphere using the 25 representative points and Gaussian radial distances for these points. Determine the range of the Gaussian radial distances. This range is defined as the probing form error of HS1 or the MoMat test sphere. If a multi-material sphere is used, repeat the procedure for the second half of the MuMat test sphere to obtain the probing form error of HS2. Compare the probing dispersion errors of HS1 and HS2; the highest absolute value is the multi-material probing form error $P_{\text{Form.MuMa.Sph.1x25::CT}}$.

The size of all patch areas should be equal and can be freely chosen as long as no overlap between patches occurs. A suggested pattern for the patches is given in ISO 10360-5 [97] and presented in Fig. 3.4. If a multi-material sphere is used, the patch pattern should be aligned in such way to cover the surface of one half sphere (made of a single material). To separate material effects, patches in the pole region of the MuMat test sphere should be avoided, since pole artefacts are expected to be covered in the mono-material test for CT. Patches significantly impaired by the MuMat assembly design or pole artefacts shall be also avoided in the analysis, e.g. two materials creating a single patch, or patch being disturbed by the mounting shaft or glue. To be considered a valid patch, its points should cover at least

3.2. Proposal for a multi-material acceptance test

50% of the predefined patch area. A minimum of 13 patch-based representative points per half sphere shall be used for the analysis. The same raw data points acquired in both halves of the MuMat test sphere used to calculate the $P_{\text{Form.MuMa.Sph.D95\%::CT}}$, shall be used to calculate the $P_{\text{Form.MuMa.Sph.1x25::CT}}$.

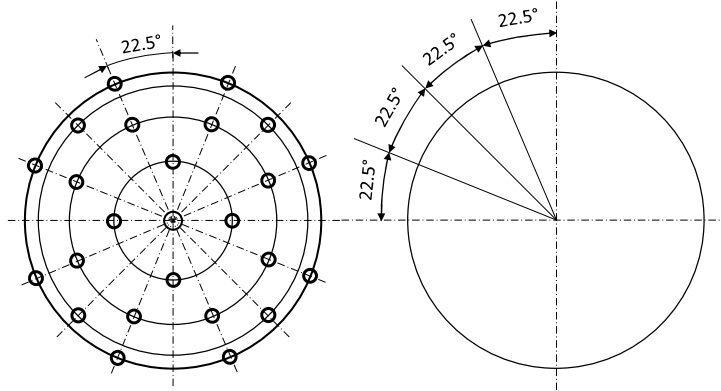


Fig. 3.4. Suggested pattern of the 25 patch-based representative points for the evaluation of $P_{\text{Form.MuMa.Sph.1x25::CT}}$ and $P_{\text{Size.MuMa.Sph.1x25::CT}}$ (Source: [97]).

Multi-material probing size error All ($P_{\text{Size.MuMa.Sph.All::CT}}$): From the raw data points acquired with both halves of the MuMat test sphere or with the MoMat test sphere used to calculate $P_{\text{Form.MuMa.Sph.D95\%::CT}}$ and $P_{\text{Form.MuMa.Sph.1x25::CT}}$, fit an unconstrained least-squares sphere based on all raw points acquired for one half (HS1) of the MuMat test sphere or for the MoMat test sphere, and determine its diameter. The difference of the diameter between the least-square sphere and its calibrated diameter is the multi-material probing size error All of HS1 or of the MoMat test sphere. If a multi-material sphere is used, repeat the procedure using the raw points acquired for the second half sphere to obtain the multi-material probing size error All of HS2. Compare multi-material probing size error All of HS1 and HS2; the highest absolute value is the multi-material probing size error All $P_{\text{Size.MuMa.Sph.All::CT}}$.

Multi-material probing size error ($P_{\text{Size.MuMa.Sph.1x25::CT}}$): The same representative points, which have been used for the MuMat probing form error of HS1 or the MoMat test sphere are used for the evaluation of the MuMat probing size error of HS1 or of the MoMat test sphere. Fit an unconstrained least-squares sphere using the representative points. Determine the diameter of the patch-based least-square sphere in one half sphere or in the MoMat test sphere. The difference of the patch-based sphere diameter to its calibrated diameter is the multi-material probing size error of HS1 or of the MoMat test sphere. If a multi-material sphere is used, repeat the procedure using the representative points calculated in the second half of the MuMat test sphere, which were used for the MuMat probing form error of HS2 to obtain the multi-material probing size error of HS2. Compare the multi-

material probing size error of HS1 and HS2. The highest absolute value is the multi-material probing size error $P_{\text{Size,MuMa,Sph.1x25:CT}}$.

Derivation of the MuMat P -test results

The metrological characteristics of the multi-material probing error test comply with the specified MPE if the measured quantities do not exceed the probing error maximum permissible errors $P_{\text{MuMa:CT,MPE}}$. The expanded test value uncertainty shall be considered as described in the ISO 14253-1 [93]:

- $|P_{\text{MuMa:CT}}| \leq |P_{\text{MuMa:CT,MPE}}| - U_{\text{Test}}$ for performing the test by the manufacturer to demonstrate conformity with the maximum permissible errors.
- $|P_{\text{MuMa:CT}}| > |P_{\text{MuMa:CT,MPE}}| + U_{\text{Test}}$ for performing the test by the user to demonstrate nonconformity with the maximum permissible errors.

Fig. 3.5 illustrates these inequalities of conform and nonconform zones for the evaluation of the MuMat P -test results.

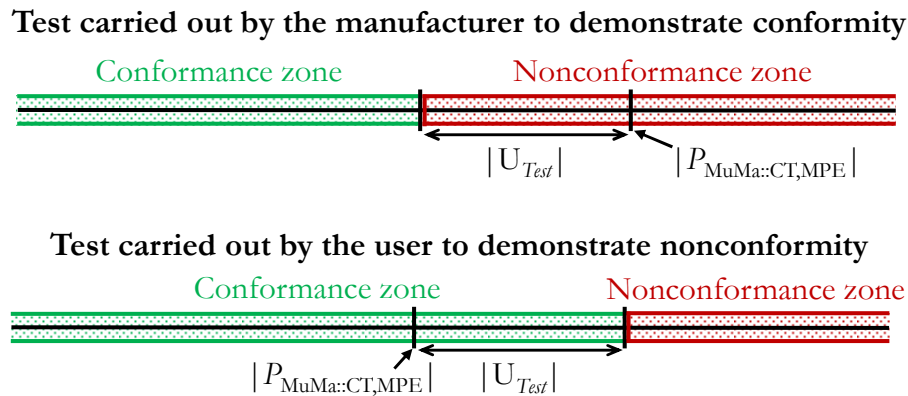


Fig. 3.5. Graphical illustration of conformity and nonconformity considering the test value uncertainty.

All repeated measurements for all measured metrological characteristics shall conform with the MPE provided by the manufacturer. If any repetition or metrological characteristics exceed the respective MPE, the scan shall be repeated once.

3.2.4 Multi-material length measurement error test

The principle of measuring (long) length reference standards from the ISO 10360-2 is also adopted in the multi-material E -test. However, for the proposed E -test, the test measurements are to be performed with multi-material length reference standard(s).

The data evaluation is based on length (i.e. distance) measurements between geometric elements (e.g. cylinders, spheres, planes, etc.). The results of the CT length measurements are to be compared with calibrated reference measurements and the multi-material influence on the length measurement is to be identified.

The MPEs of the multi-material length measurement shall be declared along with the test conditions, e.g. material combination, maximum penetration length per material, in which the MPE is specified. Different material combinations of the E -test could result in different MuMat length measurement errors. Therefore, the manufacturer can either declare several MPEs for the multi-material length measurement error for different material combinations, or a single MPE covering a wide range of material combinations.

(Suggested) Multi-material length measurement test characteristics

Length is the main characteristic to be evaluated by the multi-material E -test. Several types of measurand can define a length: bi-, unidirectional or lengths based on the centre of mass of points acquired on surface of geometrical features, see Fig. 2.24. Uni- or bidirectional measurements may be evaluated using representative points reduced from patch operators.

The MuMat E -characteristics — to be assessed using multi-material length reference standard — are used to detect the MuMat influence on length. The E -test characteristics suggested in this work are based on the current discussions of standards and the definition of the two metrological quantities to be evaluated by the E -test are given below:

Multi-material bidirectional length measurement error ($E_{\text{Bi:MuMa:CT}}$): error of indication (bidirectional length measurement error) when bidirectionally measuring a calibrated test length. Inner and outer distances are to be assessed as point-to-point distance or representative point-to-representative point distance, where each point is created from patch operators. If patch-based representative points are used to create the measurand, it should be stated as e.g. $E_{\text{Bi:MuMa:1x2:CT}}$.

Multi-material volumetric length measurement error ($E_{\text{MVol:MuMa:Avg:CT}}$): error of indication when measuring a calibrated test length where the error is derived from the distance between two averaged representative points each created from multiple measurement points of two respective geometrical elements to be measured with MuMat length reference standard. The averaged representative points can be derived from e.g. centre-to-centre measurements between spheres or circles. Centre-to-centre distances between cylinders can be also used, but the calculated cylinder axis must be projected onto a defined plane.

In this test proposal, length measurement error is assessed using the mandatory characteristics multi-material bidirectional length measurement error being assessed as a mandatory inter-material measurement situation. The MuMat volumetric length measurement error and in-material and mono-material measurement situations might be optionally evaluated.

Measuring equipment for the multi-material length measurement error

The MuMat *E*-test is to be performed in a MuMat length reference standard. The materials for the MuMat *E*-test should comply with the manufacturer requirements and specifications. The selection of the materials for the test should conform with the requirements for the material combination and thickness presented in § 3.2.2.

At least three bidirectional inner and outer lengths, each in five different spatial directions are required to be measured. Short, middle and long calibrated lengths ranging from 20% or less and more than 70% of the measurement volume's longest diagonal are required. The MuMat influence on the measurement depends on different material penetration lengths. Therefore, the standard should feature different multi-material penetration lengths as well.

For the evaluation of the multi-material volumetric length measurement error, the distances to be measured should be created by fitting operations based on the cartesian points acquired on geometrical primitives, e.g. cylinders, circles, spheres.

The *E*-test shall include bidirectional inner and outer length measurements to be measured as inter-material measurement situation. Optionally, the test could also include measurements based on centre-to-centre lengths measured in mono- and in-material measurement situations, serving as a tool for separation of effects in the data evaluation.

Multi-material length measurement test procedure

The test measurements shall be carried out according to the specifications and recommendations provided by the manufacturer and shall comply with the specified rated operating conditions. The results of the test measurements are to be compared with the MPEs. The manufacturer specifies the MPEs of the multi-material length measurement error characteristics so that they can be maintained throughout the entire measurement volume.

The MPEs of the multi-material length measurement error characteristics can be specified for each specific multi-material combination (i.e. material and attenuation coefficient ratio classes). This means a single CT-based CMS can be specified for several MPEs. The manufacturer is also allowed to specify the system covering a greater range of material combinations. However, in this case it is necessary to specify for which material combinations a given specification is valid, e.g. the systems multi-material MPE is valid from high to moderate-low attenuation coefficients ratios for plastic-like with Al-like materials and plastic-like with Ti-like materials.

All MuMat *E*-test measurements shall be performed using MuMat length standard. To guarantee independent results, re-using the MuMat standard in any qualification step is prohibited.

3.2. Proposal for a multi-material acceptance test

The manufacturer shall provide the set of scanning parameters to perform the scans and information about the material combination for the test measurements, i.e. classes of materials and class of attenuation coefficient ratio, unless agreed. The user is free to choose the material within the material class, as long as the attenuation coefficient ratio and material classes are maintained.

The MuMat E -test shall be performed at one geometrical magnification per multi-material combination. The geometrical magnification should be chosen such that the longest length to be measured in the MuMat length standard covers at least 70% of the longest spatial diagonal of the measurement volume. All length measurements shall lie within specification, i.e. within the MPE range. If one repetition lies out of specification, a single additional repetition is allowed.

The positioning and orientation of the standard shall ensure a valid and complete measurement of the MuMat length standard, i.e. the complete geometry under test shall be acquired in all projections. The regions, where the data points are acquired shall not be influenced by the clamping system or fixing components.

The MuMat standard is to be scanned in such way that its materials significantly attenuate the radiation. The total material penetration length should include both materials in at least 40% of the 2D projections i.e. multi-material overlap in the X-ray projections should be significant. It is recommended that throughout the complete CT scan, i.e. 360° rotation, the overlap between the materials should increase until it reaches full and decrease until it reaches no material overlap.

All fitting operations for the measurements shall be based on the least-squares method. Point-to-point measurements resulting from the operation of multiple points being acquired in a large part of the geometrical primitive are used in the test measurements. Also, length measurements based on representative point-to-representative point — derived from patch operators representing a small portion of the geometrical primitive are used in the data evaluation as well. The latter is intended to create bidirectional measurements to detect effects and error not detected by e.g. centre-to-centre measurements.

If more than one MuMat length standard is used with e.g. different material combinations, each standard shall be scanned separately. The materials and attenuation coefficient ratio of the materials used in the test shall be stated as well. The manufacturer can either state separate MPEs for each multi-material combination tested or a single MPE covering a large range of multi-material combinations. However, in the latter case, it is necessary to specify for which multi-material combinations the specification the MPE is

valid, e.g. the system is specified for attenuation coefficient ratios from high to moderate-low for plastic-like with Al-like materials and Ti-like materials.

The two metrological characteristics are to be measured and compared to both reference values and to the maximum permissible errors provided by the manufacturer.

Multi-material volumetric length measurement error ($E_{MVol:MuMa::CT}$): Fit appropriate unconstrained Gaussian primitive elements (e.g. cylinders, circles, spheres, planes) using all data points acquired on the geometrical elements of a multi-material length reference standard. Calculate the averaged point representing the centre of mass of all acquired points. At least 50% of the geometrical primitive's surface should be covered when creating the averaged point (e.g. if sphere centres are measured, at least half of the sphere should be used). The length is defined as the 3D distance between two averaged points created in two geometrical elements of the same kind (e.g. circle centre to circle centre distance). The two centres of mass used to form a length should be created using the same measurement strategy (i.e. same nominal number of points, same geometrical element). The error of indication of a length measurement when compared to the calibrated length (using the same measurement strategy) is the multi-material length measurement error average $E_{MVol:MuMa::CT}$.

Multi-material bidirectional length measurement error ($E_{Bi:MuMa::CT}$): Acquire data points on the surface of the geometrical primitives and calculate the centre of mass of the acquired points for each primitive. Create a connecting line between both centre of mass points. Extend the line until it intersects the geometrical elements. Create intersection points of the extended line with the primitive's surfaces. If the line intersects the element's surface in more than one point (e.g. this is the case of spheres or cylinders), the point to be used shall be based on the measurand. For instance, for measuring bidirectional outer lengths, the points characterising the shortest distance between the two elements shall be used, cf. Fig. 2.24. Using the raw data points, select regions of points — patches — on the geometrical primitives of a MuMat length standard to calculate representative points. The point regions should be centred on the intersection points to form a bidirectional length. Both inner and outer bidirectional lengths are mandatory. Fit the appropriate unconstrained Gaussian primitive and calculate the centre of mass from the points selected in the patch. Calculate the connecting line between the centre of mass of the points and the centre of the Gaussian element based on the patch points. Next, calculate the intersection point between the line and the surface of the Gaussian primitive based on the patch points. The intersection point corresponds to the representative point based on the patch points. Repeat the procedure for the second geometrical primitive with surface normal opposite to the first geometrical

element to create the second representative point. The distance between two representative points, created from distinct geometrical primitives, with opposite surface normal direction, represents the bidirectional length. The error of indication between the measured bidirectional test length and its calibrated length being measured in a multi-material standard is the multi-material bidirectional length measurement error $E_{Bi:MuMat:CT}$. Both representative points must be created using nominally the same measurement strategy, e.g. same patch size and point density. The patch shall cover a small region of the geometrical primitive and, in order to guarantee a stable fit of the geometrical element based on the patch points, the patch region shall cover between 15% and 25% of the total area of the geometrical element. To be considered a valid patch, the area of selection shall be connected, and the representative point shall be based on more than 60% of the nominal number of patch points.

Bidirectional lengths can also be created from the measurement of single points being probed in opposite surface normals of a MuMat length standard. However, for comparability reasons between e.g. CT- and tactile-based CMSs, it is recommended to carry out the bidirectional length measurements based on patch operators. If patch-based representative points are used to create the measurand, it should be stated as e.g. $E_{Bi:1x2:MuMa:CT}$.

Derivation of the MuMat length measurement error test results

The CMS complies with the specified $E_{MuMa:CT,MPE}$ for the metrological characteristics of the MuMat length error test if the measured quantities do not exceed the respective MPEs.

The test value uncertainty should also be stated in the E -test report. The concepts described in the ISO/TS 23165:2006 international standard are to be applied for the estimation of the test value uncertainty. The graphical illustration of the MuMat E -test results can be interpreted analogously to the MuMat P -test result, as illustrated in Fig. 3.5.

The expanded test value uncertainty shall be considered in the test results as follows:

- $|E_{MuMa:CT}| \leq |E_{MuMa:CT,MPE}| - U_{Test}$ for performing the test by the manufacturer to demonstrate conformity with the maximum permissible errors.
- $|E_{MuMa:CT}| > |E_{MuMa:CT,MPE}| + U_{Test}$ for performing the test by the user to demonstrate nonconformity with the maximum permissible errors.

At least 29 (i.e. 95%) out of the 30 required lengths based on the metrological characteristics shall conform to the MPEs provided by the manufacturer. If more than 5% of the measured lengths for any metrological characteristic exceed the respective MPE, the scan can be repeated once.

3.3 Verification concept

The verification concept consists of the implementation of the proposed MuMat test and the execution of the experimental studies using PTB's CT-based CMS for verifying if the multi-material acceptance test proposal fulfils its requirements.

The definition of the implementation and experimental requirements is based on the proposal requirements (i.e. § 3.1) and it is the first step towards the verification of the proposal. The implementation includes designs, concepts and the steps of the proposal realisation. At the end of the verification concept, the description of the experimental plan is presented.

3.3.1 Requirements of the verification concept

The verification requirements aim to limit the scope of the implementation and experiments, as in practice, it is very costly to specify a CT-based CMS for all possible multi-material measurements. Therefore, the verification concept should:

- Verify if the MuMat test requirements are fulfilled
 - By demonstrating the influence of MuMat effects on CT measurements by means of measuring a set of MuMat standards for probing and length measurement error tests.
 - By evaluating the uncertainty of the test.
- General requirements of the implementation of the acceptance test
 - Multi-material standards for *P*- and *E*- should be realised.
 - The standards shall be calibrated using a traceable tactile CMS.
 - The data analyses should be suitable for CT and tactile measurements ensuring comparability and traceability to the metre.
 - The design of the standards should have sufficient multi-material penetration lengths in every relevant orientation.
 - The multi-material standards should allow the creation of different multi-material combinations, i.e. attenuation coefficient ratios, see § *Material combination for the multi-material acceptance testing*, using suitable materials, with respect to X-ray attenuation coefficient for a 225 kV CT-based CMS.
 - Additionally, the test should also include a mono-material standard using the same basic design (as a reference).
- Requirements of the implementation of the MuMat probing error

3.3. Verification concept

- The multi-material P -test should use the existing concepts of the standardised mono-material P -test. Therefore, it comprises size and form measurements of a (MuMat) test sphere.
- The size of the test sphere shall represent a small portion of the measurement volume (e.g. maximum 20% of the longest diagonal of the targeted measurement volume).
- The geometrical and surface properties of the multi-material test sphere(s) shall have a negligible influence on the measurement result by CT.
- The mechanical design and manufacturing induced errors of the multi-material test sphere shall not significantly affect the test measurement results.
- The MuMat test sphere design shall allow in-material measurement situations. Inter-material measurement situations are optional.
- Specific requirements of the implementation of the MuMat length measurement error
 - The multi-material E -test should be evaluated as length measurements using standards consisting of two or more materials.
 - The size of the standard should allow measurements with medium-range magnification, based on the assumption that the multi-material effects are generic in nature.
 - The design of multi-material length standard should feature short and long lengths to be measured along different spatial directions.
 - The measurands should be created based on geometrical primitives, i.e. regular geometries such as spheres, circles, etc.
 - The measurands created from geometrical elements should have different (multi-) material penetration lengths.
 - The MuMat standard body should enable separation of effects through different measurement situations (cf. Fig. 3.2). Inter-material and in-material measurements as well as mono-material measurements should be performed in the test.
 - The implementation of the MuMat E -test should allow flexibility regarding the definition of measurands. Volumetric measurements based on the centre of mass of several points, uni- and bidirectional length measurands based on patch operators are required.

- The length standard should feature different ratios of multi-material penetration lengths.
- Fixing elements (e.g. screws and nuts) should not affect the measurement significantly, however they shall maintain the mechanical stability of the standard.
- The *E*-test reference standard shall feature sufficiently low geometrical errors and surface roughness as to have a negligible impact on the measurement results. This includes assembly-induced effects.
- Requirements of the experiments
 - Carry out the experimental application of the complete — for *E* and *P* — multi-material acceptance test in the PTB’s CT-based CMS.
 - Verify the need for a multi-material acceptance testing with a statistical comparison to mono-material standards.
 - Verify the sensitivity of the test for MuMat effects by varying the CT parameters known to significantly influence MuMat measurements, e.g. X-ray spectrum.
 - Simulate extremecases of multi-material combinations e.g. with low attenuation coefficient ratio using the same experimental design as the real CT measurements. This experiment is to verify if the multi-material effects increase proportionally with the difference in the attenuation coefficient.

3.3.2 Implementation of the multi-material *P*-test

The main objective of the implementation phase is to design and develop a set of MuMat standards and to develop an example measurement workflow including all the steps of the measurement chain. The MuMat standards and the measurement workflow shall be able to test the performance of the CT-based CMS for *P* metrological characteristics. These should comply with the proposal and verification requirements.

Reference standard — Design of the multi-material test spheres

The main function of reference standards is to realise, maintain or reproduce physical quantities (e.g. the metre). In the MuMat *P*-test, the two main physical characteristics to be observed are form deviation and size of a multi-material test sphere. The MuMat reference standards are to be measured with CT and metrological characteristics are to be compared with calibrated values, providing information about the performance of the CT-based CMS. Next, the reference standards (design, materials and reference measurements) and suggested

metrological characteristics to be evaluated as well as a data analysis workflow for the MuMat probing error test are presented.

For the implementation of the multi-material *P*-test, two half spheres (HS) made of different materials are used to create a compound test sphere, see Fig. 3.6. The HS have (nominally) the same geometry and size – due to the availability, HS of 9/16 inches (approximately 14.3 mm) in diameter were used. Construction started by using a grinding process to reduce a complete, polished sphere to a half sphere and polishing the grinded flat surface. The polished faces of the two HS were glued together using high-stability epoxy-resin glue to create a finished compound sphere. The production of each separately polished half sphere was done by the sphere manufacturer. The gluing process was completed at PTB. Preliminary optical-based measurements revealed that the gap between halves created by the glue was in the range of 50 -150 μm .

The standards — test spheres — used for this kind of tests shall feature excellent metrological properties (i.e. low form error, low roughness and good mechanical stability) to allow the separation of the effects and, subsequently, statements about the performance of the CMS. Therefore, the compound sphere design (e.g. effects from grinding and gluing of the HS) and its geometrical and surface properties should not significantly influence the measurement results of the multi-material *P*-test.

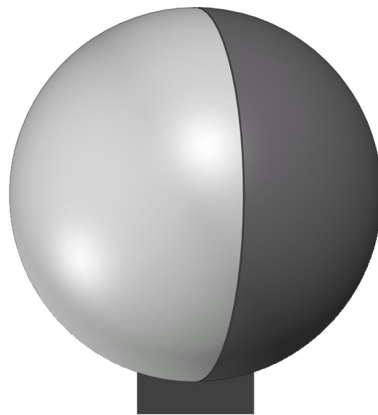


Fig. 3.6. Design of the multi-material test sphere used for the proposed *P*-test.

Materials of the multi-material test spheres

Considering the requirements for X-ray attenuation, costs, availability, geometrical and surface properties, the range of materials suitable for manufacturing a spherical geometry is limited.

The materials considered for the MuMat *P*-test were initially based on spheres commonly used as tactile probes, as they usually feature excellent metrological properties (i.e. are comparable to the measurement uncertainty levels obtained with tactile-based CMSs), competitive pricing and wide-spread availability. The most common materials used

for the tactile probing spheres are ruby ($\text{Al}_2\text{O}_3\text{:Cr}$), aluminium oxide (Al_2O_3) and silicon nitride (Si_3N_4).

The attenuation coefficients of the materials were tested beforehand using simulations and real data. Several X-ray spectra and different materials were used to confirm whether the materials fulfilled the implementation requirements of high and moderate classes of attenuation coefficient ratio. Silicon nitride and aluminium oxide were found to be suitable materials for the proposed implementation, with respect to attenuation, metrological properties and costs.

However, Si_3N_4 and Al_2O_3 do not fully meet the requirement of moderate attenuation coefficient ratio, as they have similar attenuation coefficients (e.g. at 150 kV with no filter, an attenuation coefficient ratio of approximately 0.9, see Table 3.3). Therefore, a third material, with significantly higher attenuation coefficient, had to be added to the test. A variety of materials such as metals, ceramics and glasses were considered.

For the implementation of the MuMat acceptance test, titanium, when combined with e.g. Al_2O_3 , reaches a moderate attenuation coefficient ratio for all energies of the spectrum ranging from 30 kV to 225 kV. Optical glasses such as N-SF6 (which is a lead-free version of SF6) and SF6 were considered for their adequate attenuation coefficient and excellent surface and geometrical quality, even when manufactured in a spherical shape. Zirconia oxide was also considered as a potential third material for implementing the MuMat *P*-test. This ceramic is also widely used for tactile probe spheres, featuring excellent surface and geometrical properties.

The four materials: Ti, N-SF6, SF6 and ZrO_2 were compared in a decision matrix, where criteria such as attenuation coefficient (where it matched the implementation requirements), manufacturing costs, delivery time, surface and geometrical characteristics, material homogeneity and the presence of lead in their chemical composition were considered, see Table 3.2. Preliminary measurements have shown that lead (e.g. in the grained mixed form) can severely disturb the CT measurement, causing local surface offsets, due to its high atomic number and attenuation coefficient.

Each criterion was weighted according to its importance. Similarly, each material was rated for its degree of compliance with the criteria. In Table 3.2, importance and compliance were scored from one to five, where five represents the highest importance or full compliance with the criterion, while one is of lowest importance and no-compliance with the criterium. For each criterion, importance and rating were multiplied. The final score of each material was calculated as the sum total of its weighted scores. The optical glass N-SF6 achieved the highest rating in the table and was therefore selected as third material.

3.3. Verification concept

Table 3.2. Decision matrix for the selection of the third material for the multi-material *P*-test.

Criterion	Materials								
	Importance	Ti		N-SF6		ZrO ₂		SF6	
Attenuation coefficient	5	× 5	25	× 5	25	× 1	5	× 1	5
Manufacturing costs	4	× 5	20	× 4	16	× 5	20	× 4	16
Delivery time	4	× 5	20	× 4	16	× 5	20	× 4	16
Surface properties	5	× 2	10	× 5	25	× 5	25	× 5	25
Geometrical properties	5	× 1	5	× 5	25	× 5	25	× 5	25
Homogeneity	5	× 5	25	× 5	25	× 5	25	× 5	25
Lead-free	5	× 5	25	× 5	25	× 5	25	× 1	5
Sum total		140		157		145		117	

The three selected materials (namely) silicon nitride (Si₃N₄), aluminium oxide (Al₂O₃) and the lead-free glass, N-SF6, were paired, resulting in three multi-material compound test spheres and – as a reference – three mono-material compound spheres, see Fig. 3.7.



Fig. 3.7. Set of multi- and mono-material compound spheres used for the assessment of the *P*-test. From left to right: three MuMat-spheres Al₂O₃ & Si₃N₄, Si₃N₄ & N-SF6 and Al₂O₃ & N-SF6; and three MoMat-spheres Si₃N₄ & Si₃N₄, Al₂O₃ & Al₂O₃ and N-SF6 & N-SF6.

Fig. 3.8 presents the theoretical attenuation curves for the X-ray spectrum from 0 to 225 kV of Al₂O₃, Si₃N₄ and N-SF6 materials. The attenuation curves were created using the CT simulation tool aRTist, BAM, Berlin. The chemical composition of N-SF6 was obtained in [98].

Additionally, Table 3.3 shows the experimental attenuation coefficient ratios (μ_2/μ_1) at 150 kV X-ray tube voltage without a physical filter on the source. The attenuation coefficient was measured and calculated based on the Lambert-Beer Law and the X-ray transmission of each material quantified for a given material penetration length. Note that the example values reported in the Table 3.3 are not physical constants as they depend on the X-ray spectrum, cf. Fig. 3.8. As an example, N-SF6 and Al₂O₃ absorption values are greater than Si₃N₄ by a factor of 2.3 and 1.1, respectively. More asymmetric scenarios with respect to shape and absorption could also occur, e.g. with the volume of the reference objects consisting of 95% N-SF6 and 5% Si₃N₄ or half spheres made of steel and PEEK. In this work more extreme multi-material cases are tested based only on simulation data. The investigations based on

real CT scans were focused on the evaluation of the new MuMat test concept and extreme cases are included.

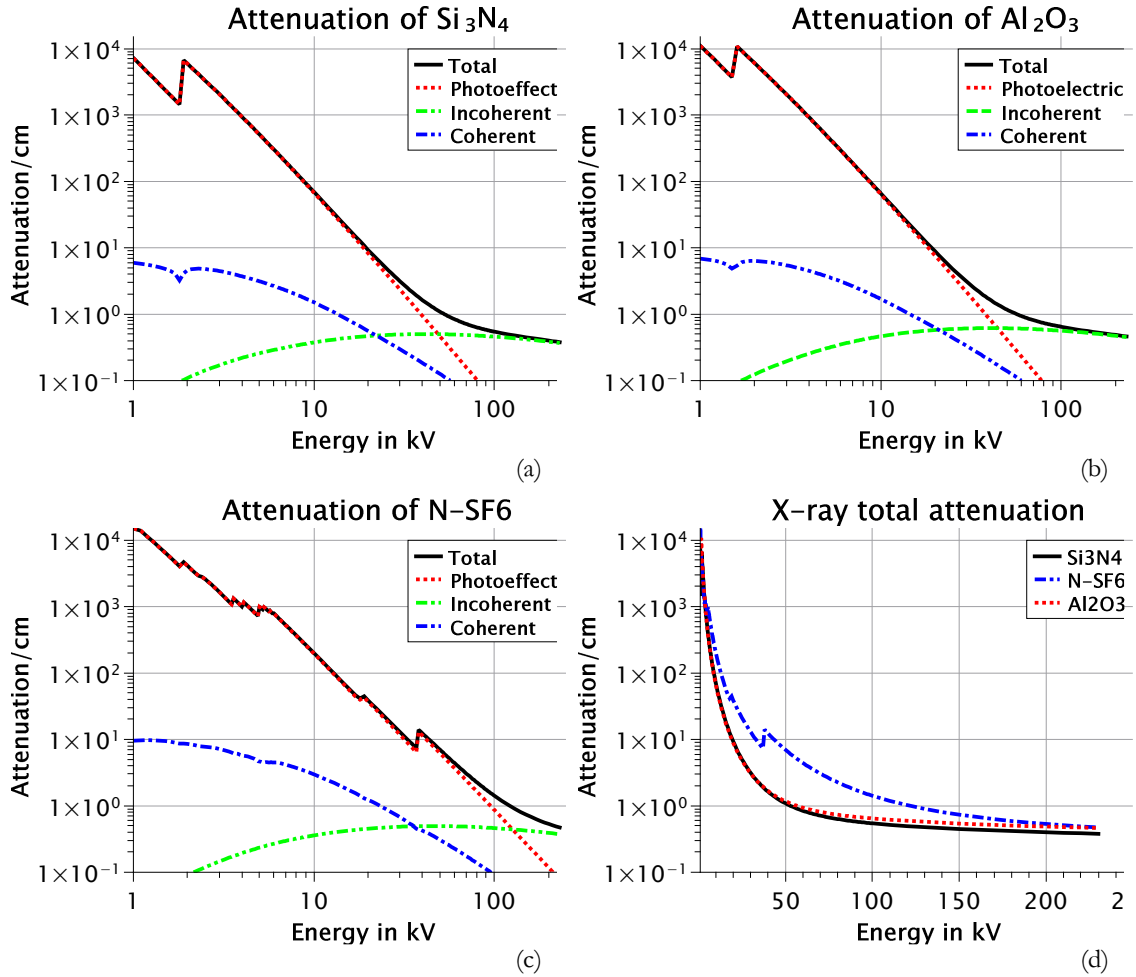


Fig. 3.8. Attenuation curves of the materials selected for the multi-material *P*-test: (a) Si₃N₄; (b) Al₂O₃, (c) N-SF₆ and (d) total attenuation of the three materials. (Source:[43,98]).

Table 3.3. Material pairings used for the multi-material *P*-test realisation with their experimentally determined X-ray attenuation coefficient ratio and classification of the attenuation coefficient scenarios based on Table 3.1.

	Materials	Attenuation coefficient ratio (μ_2/μ_1) at 150 kV, no filter	Classification
MuMat spheres	Al ₂ O ₃ /Si ₃ N ₄	0.9	High
	N-SF ₆ /Al ₂ O ₃	0.5	Moderate
	N-SF ₆ /Si ₃ N ₄	0.4	Low-moderate

Reference measurements of the multi-material test spheres

The multi- and mono-material spheres were all calibrated using a tactile CMS. The calibration strategy measures each half sphere separately (but already in the glued compound state). The gluing process of the multi-material spheres was carried out manually; the gap/glue was estimated to be in the range of 40 to 150 μm . An area within approximately 500 μm close to the transition was therefore excluded from tactile CMS probing. A total of 64 evenly

3.3. Verification concept

distributed points were acquired over an area of approximate 120° opening angle near the pole (opposite to the carbon fibre shaft, see Fig. 3.9). Thus, the glue/gap area and its immediate vicinity were excluded from the analysis. The expanded measurement uncertainty U ($k=2$) of each single point was of the order of $1\ \mu\text{m}$ or less.

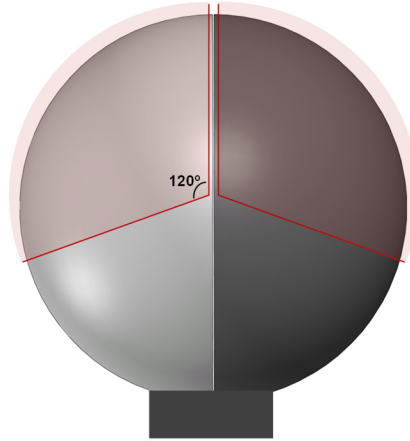


Fig. 3.9. Calibration area of the multi-material spheres.

Diameter and form deviation of each half sphere were determined separately using a least-squares fit. The data evaluation performed on two HS separately, differs from the standard mono-material P -test. Preliminary experiments showed a significant influence of the glue/gap area in the results. It is worth mentioning that sphere fit used for probing characteristics in tactile-based CMSs are also based on half spheres, due to the limited access of the probing sphere below the test sphere equator.

The form deviation of all half spheres was found to be below $0.5\ \mu\text{m}$. This number is comparable to the specified form error of full spheres. Thus, it confirms that cutting or grinding full spheres to create half spheres made of the given materials does not cause significant degradation of the form. Spheres with high form deviation (greater than the voxel size) would not allow statements to be made about multi-material effects due to the confluence of several influence factors present in the data.

It is recommended to perform the tactile calibration of the two half spheres separately to avoid the interface region between two material and its vicinity. This interface region between the two materials leads to an invalid measurement when compared to the standard MoMat test, since it can result, for instance, in large form errors due to potential manufacturing errors. Large form errors may lead to mistaken statements when the form error measured from the CT data is compared to the tactile form error measured in the region affected by the manufacturing process.

Data analyses

The data analyses of the multi-material probing error test are based on the deviations from the tactile reference measurements for size measurements and absolute form measurements. The evaluation of different material combinations, i.e. mono-material, high and moderate and low-moderate attenuation coefficient ratio, are also part of the data analyses. The diameter and form deviation of each HS were evaluated separately based on the four metrological characteristics: $P_{\text{Form.MuMa.Sph.D95\%:CT}}$, $P_{\text{Form.MuMa.Sph.1x25:CT}}$, $P_{\text{Size.MuMa.Sph.All:CT}}$ and $P_{\text{Size.MuMa.Sph.1x25:CT}}$, cf section (*Suggested*) *Multi-material probing error geometrical characteristics*.

The evaluation of the MuMat P -test is carried out in each HS separately because of the unavoidable mounting-related effects, see examples in Fig. 3.10, present in any realistic scenario of compound sphere such as this. Preliminary simulation-based tests have shown a non-negligible influence of the mounting-related imperfections of the MuMat-spheres on the measurement results, unless data handling of the HS is applied, e.g. a translation and re-scale of one HS relative to the other.

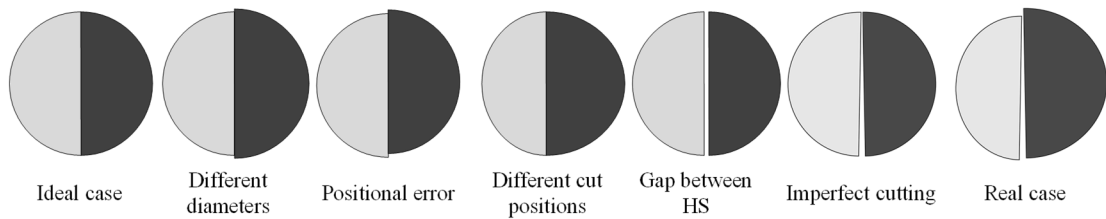


Fig. 3.10. Unwanted cutting- or mounting-related scenarios.

Size (i.e. diameter) and form error are to be calculated using the data points acquired on the MuMat test spheres, using all, 95% of the data points and using 25 representative points reduced from patch operators. This approach — which entered ISO 10360 methodology with ISO 10360-8 [73] for optical distance sensors — yields more stable results when measuring form and size, by reducing the influence of the sensor noise e.g. by eliminating outliers. The patch approach also improves comparability between CMSs with different sensor technologies, mainly due to the high density of points obtained by CT and optical sensors, and due to the morphological filtering inherent to tactile probing. However, in the current international standard for optical distance sensors some unsolved issues remain, e.g. the unsatisfactory patch geometry description. Besides this, the use of patches has intrinsic low pass filter characteristics and may suppress local effects of the system, which might be relevant for the user.

Moreover, when the multi-material P -test is performed on a MuMat test sphere as a whole, some patches of the pattern should be excluded from the analysis, as they might comprise two different materials in a single patch. This is not a common scenario in

coordinate metrology and might be considered unfair when compared to the standard mono-material P -test. Furthermore, Feldkamp artefacts (i.e. pole artefacts) are also excluded from the approach applied to the multi-material P -test, seeing as they are already included in the standard mono-material test. Therefore, in order to set up a fair test scenario for the probing error test with a multi-material assembled sphere, the HS data are evaluated separately. The same strategy was also applied to three mono-material spheres to cross-check the concept.

Current surface determination algorithms implemented in commercial CT data analysis software determine the surface of a material based on a single threshold value as starting step. They do not consider the presence of a second material. However, if the difference in the attenuation coefficients of the materials being measured are large enough, the result of the single-threshold-based surface determination is a large offset of the surface in one of the materials, creating large size errors or, in some cases, the inability to perform the measurement (at all) in the LAM, as presented in Fig. 3.11.

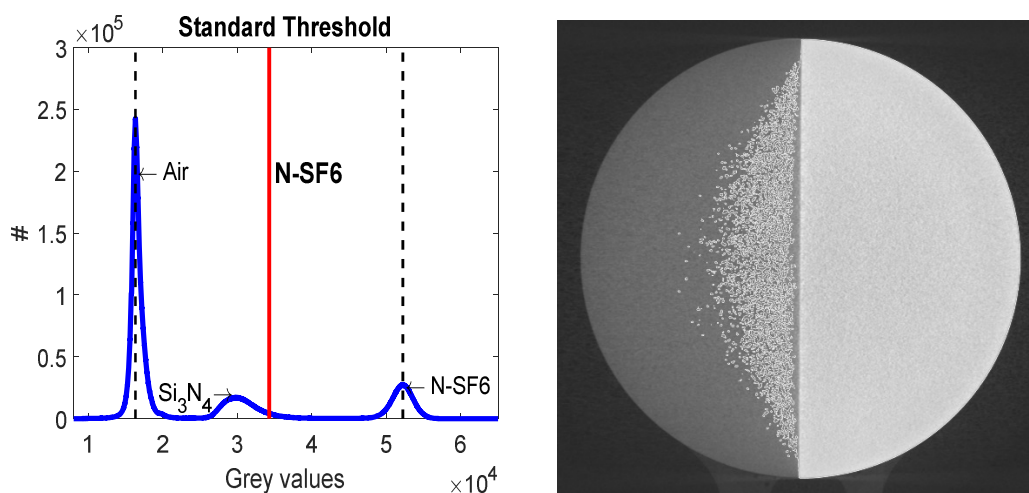


Fig. 3.11. Standard threshold value for the multi-material sphere. This example shows the histogram and the central slice of the CT scan of the HS made of Si_3N_4 and the optical glass N-SF6. The standard method of surface determination does not consider the presence of the Si_3N_4 . Therefore, the surface determination of the Si_3N_4 half is heavily impaired and dimensional measurements are not possible.

The workflow starts with the scan of the MuMat compound spheres, see Fig. 3.12. To overcome the imperfections introduced by the assembly process, and the limitations of current surface determination algorithms regarding multi-material measurements, a novel multi-step data analysis workflow for the multi-material P -test was created and applied. The first surface determination step is optimised for the low absorption material (LAM). In the second step, an independent surface determination optimized for the high absorption material (HAM) is carried out. Next, two volumes are extracted separating the LAM HS and the HAM HS using geometry-based regions of interest (ROI). The extracted volumes (deliberately) excluded the shaft and the glue interface region. It is important to remark that the surface determinations for both HAM and LAM HSs are carried out in the same volume,

see Fig. 3.12. This means, the volume used for the surface determination steps contains the complete CT scan, including both materials of the MuMat sphere, along with the shaft and surrounding air. The extraction of the LAM and HAM HS into two separate volumes is carried out only after the surface determination for both LAM and HAM is complete. This guarantees that no information is excluded from the surface determination steps. The calculation of the P -test characteristics is also performed separately for each half sphere, as presented in Fig. 3.12.

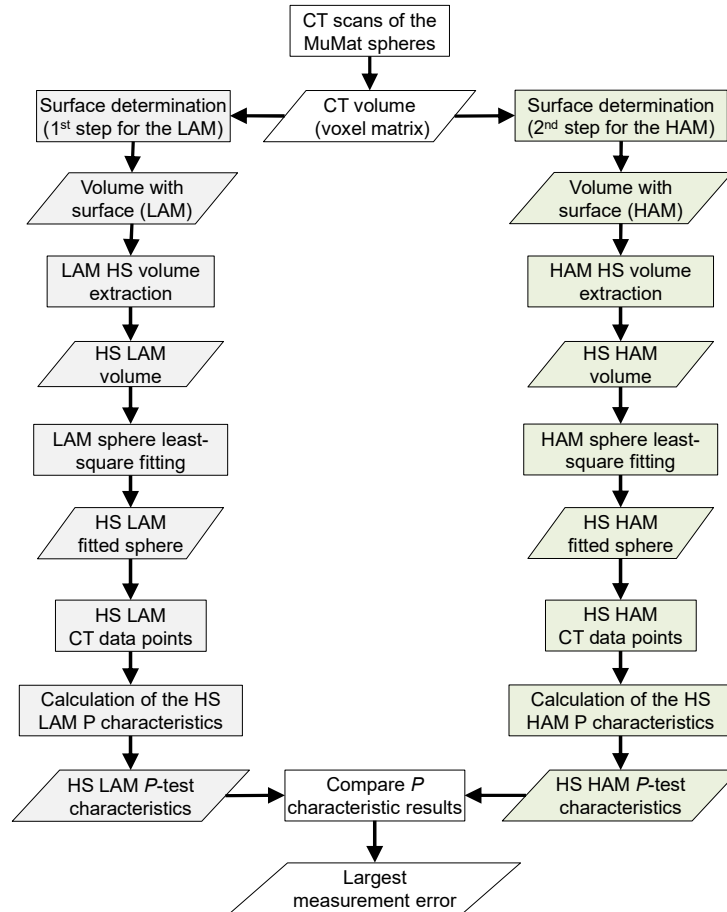


Fig. 3.12. Workflow of the multi-material P -test data analysis. The box colours indicate which volumes are involved in the individual steps towards calculating the P -characteristics. White: Full CT scan volume; Grey: Extracted LAM volume; Green: Extracted HAM volume.

The results, to be compared with reference values, are to detect the multi-material influence on the probing error test for the high and moderate and low-moderate attenuation ratio scenarios. Additionally, to verify the reference standard design, mono-material test spheres constructed using the same approach of the MuMat test spheres are to be tested as well.

The 25 representative points based on the patch operator used for the multi-material P -test characteristics, $P_{\text{Form.MuMa.Sph.1x25::CT}}$ and $P_{\text{Size.MuMa.Sph.1x25::CT}}$, are calculated for each HS separately as follows:

3.3. Verification concept

1. Fit an unconstrained least-square sphere to all data points of the complete sphere, see Fig. 3.13-a (this step will be used for a rough alignment of the sphere);
2. Align the sphere, where the centre of the half of interest should be at $x=0$ and $y=0$ and the data points of interest (i.e. the data points of the HS to be evaluated) should be at $+z$, see Fig. 3.13-b;
3. Fit an unconstrained least-squares sphere to all data points of the HS of interest, Fig. 3.13-b;
4. Select at least 13 patch centres on the fitted sphere (e.g. using the ISO 10360-5 pattern);
5. Construct cones symmetric to the selected patch centres, placing each cone apex at the initially fitted sphere centre, see Fig. 3.13-c;
6. For each individual cone, select all data points within its volume, resulting in sub point cloud (patches); the data points should not overlap each other, Fig. 3.13-c.
7. Construct centre of mass points from the patch points e.g. sphere-Fit;
8. Construct a line between the fitted sphere centre (created from all data points) and the centre of mass points calculated from each patch;
9. Intersect the lines created in step 8 with the fitted patch-based spheres resulting in representative points, see Fig. 3.13-d.

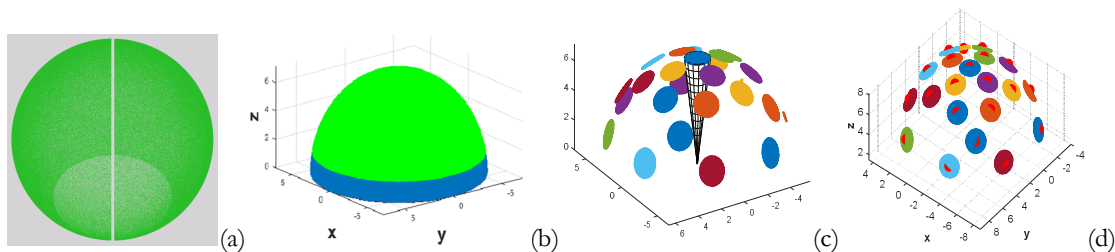


Fig. 3.13. Creation of the representative points based on patches workflow. Separation into two point-clouds and data rotation; selection of the points to be analysed (excluding the points close to the cut/glue); patch selection based on a conical shape, and creation of the 25 representative points based on 25 patches.

3.3.3 Implementation of a multi-material E -test

This section of the thesis addresses the challenge of implementing the multi-material length measurement error test (MuMat E -test). The design and realisation of the new reference object as well as the description of the data analysis are presented.

Reference standard – Design of the multi-material hole cube

For the performance evaluation of multi-material CT measurements, calibrated test lengths sensitive to MuMat effects (i.e. multi-material test length) shall be measured. A test length can be obtained when the distance of two distinct points representing the local surface or a

region or a feature of a workpiece is measured. A multi-material length is obtained when the feature points are extracted in regions of the workpiece measured by CT, where the total X-ray absorption consists of the attenuation by two or more materials.

A lack of appropriate multi-material standards for the evaluation of the length measurement error test was identified. Thus, a novel MuMat length standard design was created and presented. The design of new multi-material reference standard was inspired in the hole plate reference standard by PTB and NMIJ [55], where distances between holes in different spatial orientations are measured. The evolution of the multi-material reference standard design is presented in Fig. 3.14. The initial conception was based on a cylindrical outer shape consisting of two symmetric parts separated by a diagonal straight cut to obtain different ratios of material lengths over the standard. Besides that, the design featured calottes on the outer part of the cylinder to indicate the measurement position, respective to different ratios of material lengths, see Fig. 3.14-a. The second generation of the design also consisted in a cylindrical outer shape with similar geometrical elements (i.e. holes and calottes). However, the elements were enlarged, when compared with the initial design, to improve the measurement and manufacturing conditions (e.g. larger measurement surface in the calottes, improved aspect ratio of the holes), Fig. 3.14-b. Moderate modifications can be observed in the third generation of the design, where the calottes were replaced by “V”-shaped grooves, Fig. 3.14-c. From the manufacturing point of view, grooves are generally easier to produce than calottes, consequently elements with higher geometrical and surface quality would be obtained with the grooves. The cylindrical outer shape of the design provides highly symmetric material penetration lengths in every measurement orientation of the standard (i.e. plane perpendicular to the hole axes). To include different material penetration lengths, the original outer cylindrical shape of the design was replaced by a cubic shape presented in Fig. 3.14-d. Additionally, the straight diagonal cut present in the previous versions were also modified to the step-like diagonal cut, so that the multi-material length ratio is kept constant in the measurement areas.

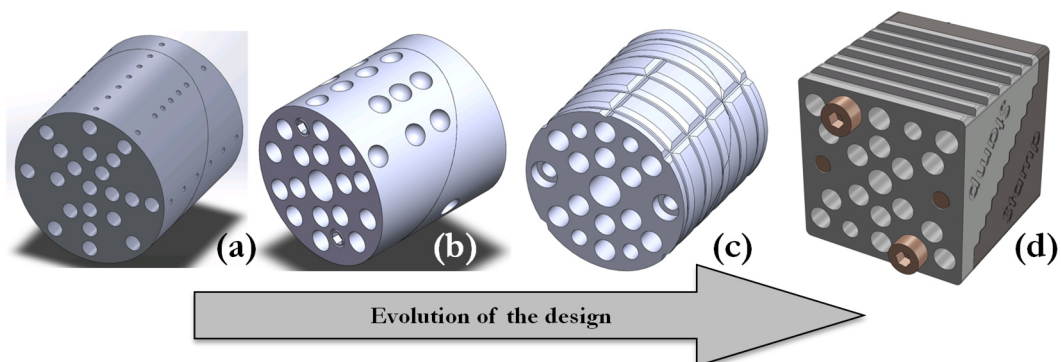


Fig. 3.14. Evolution of the multi-material length reference standard for the multi-material *E*-test.

3.3. Verification concept

More details of the multi-material hole cube standard (MuMat-HC) design is presented in Fig. 3.15. The design consists of two symmetric half cubes made of different materials, joined with fitting pins, screws and nuts made of low absorbing materials (e.g. polymers) to avoid a significant influence on the measurements. The MuMat-HC has outer dimensions of 30 mm × 30 mm × 30 mm with 17 holes and 12 “V”-shaped grooves, see in Fig. 3.15-b and -c. The design also features a stepwise “cut” along its diagonal creating a series of well-defined multi-material penetration length ratios along the standard’s height, see Fig. 3.15-c.

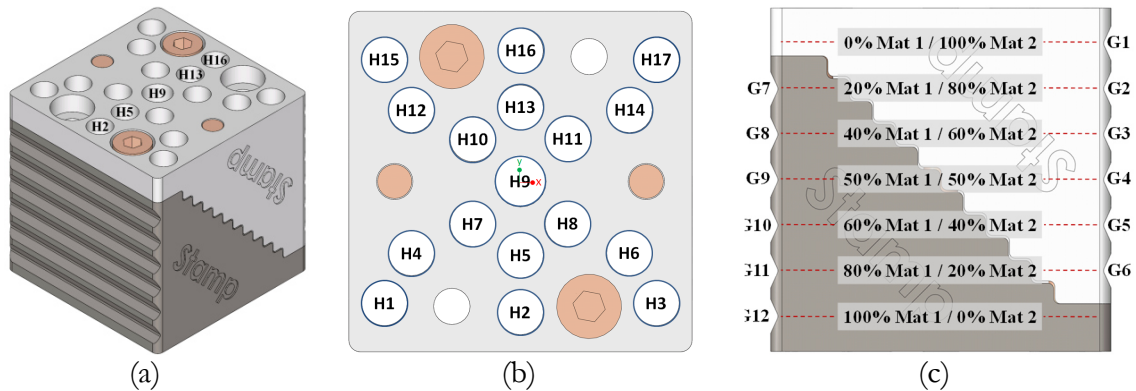


Fig. 3.15. Multi-material hole cube (MuMat-HC) design: (a) isometric view of the MuMat-HC; (b) top view of the design - highlighted the position of the holes and (c) side view of the MuMat-HC – highlighted the different material ratios along the standard.

All 17 holes have a nominal diameter of 4 mm, except hole #9, which has 4.5 mm in diameter. The reason of this difference is a higher aspect ratio for H9, which helps to stabilise the tactile reference measurements. This is important as H9 is used to register the MuMat-HC. The positions of the holes were chosen to create different material penetration lengths along different directions of the standard. The holes are arranged in such a way as to provide at least three independent length measurements in seven different directions, ranging from 1 mm to 35 mm. This is a divergence from the ISO 10360 standard, which, in several parts, requires the measurement of five independent lengths in seven main directions. However, total material penetration length as well as restrictions of the manufacturing process limit the design to three independent lengths per direction. It is also worth noting that, with regard to the mono-material standard, it is uncertain whether a requirement for five independent lengths will remain part of future versions of ISO 10360.

The length measurands in the MuMat-HC are generally based on the distances between the 17 holes in 7 heights. Such hole-to-hole length measurements permit a certain flexibility of measurands — lengths can be created using hole centre-to-centre as well as point-to-point or patch-based strategies. Thus, it is possible to use volumetric lengths, uni- or bidirectional measurements. However, in the MuMat-HC only lengths created in one plane (i.e. height) are used for the evaluation. This simplifies the data analysis by separation of effects, i.e. lengths are measured with unique and well-known multi-material ratios.

The evaluation of different multi-material measurement situations is also included in the MuMat-HC. The design allows the measurement of 136×2 mono-material lengths at grooves #1 and #12, see Fig. 3.15-c; 137×2 in-material lengths from grooves #2 to #6; and 238 inter-material length measurements in a multi-material scenario also from grooves #2 to #6. Additionally, 160 lengths using unusual measurands, where a single primitive (e.g. cylinder, circle) is created in two materials simultaneously, are also possible.

The V-shaped grooves are used for the registration/alignment of the standard to avoid regions corrupted by artefacts unrelated to multi-material effects for the registration procedure. These artefacts can be found in a measurement setup where the MuMat-HC is placed in the CT with the hole axes parallel to the rotational axis of the rotary stage. The planes perpendicular to the hole axes (top and bottom plane) are severely affected by cone-beam (Feldkamp) artefacts.

With this design, a minimum transmission of X-rays is guaranteed for a broad range of materials and CT systems. It also allows CT measurements at moderate magnifications. With the CT system used to perform the experiments in this thesis, for example, the highest magnification possible to measure with the MuMat-HC is approximately 8.5 times, where the longest measurable length covers approximately 85% of the measurement volume side-length. On the other hand, the minimum magnification — for the longest length to cover at least e.g. 50% of the measurement volume length is approximately 5 times.

A disadvantage of this concept for the multi-material *E*-test is that it depends on a complex assembly made from several materials. The different materials have potentially different thermal coefficients of expansion. This may lead to an anisotropic thermal expansion of the assembly, which in turn may cause — in extreme cases — undesired, relative displacements of the two halves. Hence, it is recommended to store and measure the cubes at a temperature range of $(20 \pm 5) ^\circ\text{C}$. In addition, the connectors fixing system used to hold the assembly together must prevent a relative movement between the two halves. Consequently, the cubes should be handled with great care. Finally, the cubes should be manufactured with high-precision manufacturing processes with sufficient surface finish quality for all selected materials, ensuring high metrological quality and a precise fit between the two parts of the assembly.

Materials of the multi-material hole cubes

In order to meet the implementation requirement, which states that the verification of the test should include high, moderate and low-moderate attenuation coefficient ratios, at least three materials must be selected and paired.

3.3. Verification concept

The starting point of the material selection was the suitability of the material's attenuation coefficient to fulfil the test requirements in the MuMat-HC design (e.g. maximum material penetration length). The selection of the materials was based on several prerequisites such as metrological stability (also relevant for tactile reference measurements), X-ray attenuation properties, manufacturing process (ideally, all materials should be manufactured with the same process to ensure similar geometrical and surface quality), material price, applicability in industry, thermal expansion coefficient, among others.

Titanium presents attractive characteristics such as suitable attenuation coefficient, interesting mechanical, thermal properties as well as electro-conductivity making it amenable to processing with high-precision electrical discharge machining technologies (EDM).

Analogous to the approach used for the multi-material *P*-test, a decision matrix, presented in Table 3.4, was used to assist in the material selection for the MuMat *E*-tests. Materials such as aluminium (Al), Zerodur, the glass ceramic Macor and the conductive ceramic Cescic were compared.

Table 3.4. Decision matrix for the selection of two materials for the multi-material *E*-test.

Criteria	Option of materials									
	Weight	Al		Zerodur		Macor		Cescic		
Attenuation coefficient	5	5	25	3	15	4	20	5	25	
Manufacturing costs	5	5	25	2	10	2	10	4	20	
Material costs	4	5	20	2	8	4	16	3	12	
Surface properties	5	5	25	5	25	5	25	5	25	
Geometrical properties	5	5	25	5	25	5	25	5	25	
Homogeneity	5	5	25	5	25	5	25	4	20	
Total		145		108		121		127		

As the complete test comprises three materials, Ti having already been selected, the two materials with the highest scores were selected from the decision matrix. Thus, Cescic — a carbon fibre composite reinforced with silicon carbide and two metal materials — aluminium (AlMg4.5Mn0.7) and titanium (Ti6Al4V). They were selected due to their large industrial applications, as well as their suitable mechanical properties and X-ray attenuation coefficients.

Although the attenuation coefficient criterion is considered in the Table 3.4, it only considers whether the attenuation coefficient of the evaluated materials differs significantly from Ti, but not if the requirement for both large and small (relative attenuation coefficients) differences in the attenuation coefficient of the complete test is fulfilled. Thus, the attenuation coefficient of aluminium, Cescic and Ti were compared. The result is shown in

Table 3.5, where a attenuation coefficient ratio equal to 1 indicates that the materials are similar and close to zero indicates that the paired materials have very different attenuation coefficients.

Table 3.5 Materials for the multi- and mono-material E -test and their measured attenuation coefficient ratios and classification of the attenuation coefficient scenarios based on Table 3.1.

	Materials	Attenuation coefficient ratio (μ_A/μ_B) @ 200 kV, no filter	Classification
MuMat-HC	Al/Cesic	0.9	High
	Cesic/Ti	0.5	Moderate
	Al/Ti	0.4	Low-moderate

There are two kinds of Cesic available on the market: HB-Cesic and Cesic-MF. The main difference between the two kinds of Cesic — as stated in the datasheet provided by the manufacturer — is the starting material used for creating the composite. The primary concern while selecting the type of Cesic to be used were inhomogeneities of the material. Preliminary tests were carried out using an optical measuring device (Alicona, based on focus variation principle) and CT scans at resolutions higher than those required for the test. Both Cesic compositions were found to be adequate for the reference standard. At the magnification to be used, no significant effect from the inhomogeneity of Cesic on the measurements is expected. Ultimately, HB-Cesic was selected for the MuMat-HCs due to its immediate availability. As a drawback, however, as a ceramic, Cesic is a fragile material and should be processed and handled carefully.

The selected materials were combined, and six cubes assembled: three mono- and three multi-material versions, see Fig. 3.16. The MuMat cubes were made to evaluate the performance of a CT-based CMS for MuMat length measurements. The MoMat cubes were measured as reference and to evaluate the design. All cubes were manufactured by electro discharge machining at PTB. Here, the electrical conductivity of all three materials, even the composite, proved to be of a great advantage over other materials considered for the design. Since, all three materials are manufactured using the same manufacturing technology, similar manufacturing quality was thus obtained. Moreover, the fitting pins and fixing screws/nuts were made from polyether ether ketone (PEEK) material due to its low attenuation coefficient and attractive mechanical properties, and they were processed by turning.

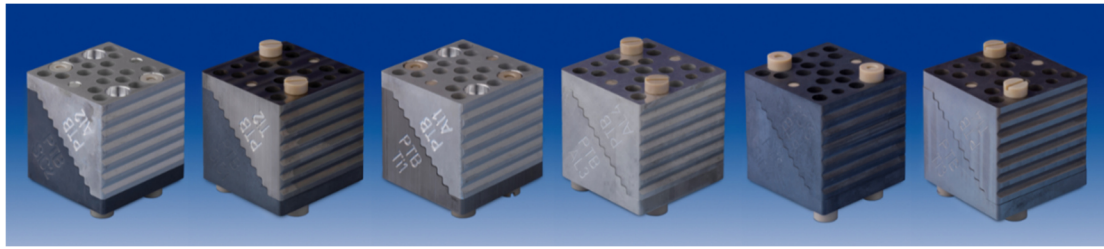


Fig. 3.16. Hole cube standards, from left to right: multi-material Al & Cesium, Cesium & Ti and Al & Ti; and mono-material Al & Al, Cesium & Cesium and Ti & Ti.

Fig. 3.17 shows the theoretical attenuation coefficient curves of the three selected materials for a spectrum range from 0 to 225 kV. It should be noted that silicon carbide was considered in place of Cesium. The simplification was necessary due to the difficulty of correctly reproducing the carbon fibres for the simulation. However, as carbon fibre has a (very) low attenuation coefficient, the impact is expected to be negligible.

The curves were created using information obtained from the material producer’s technical specifications and inspection certificates [99–101] with the CT simulation tool aRTist, BAM, Berlin.

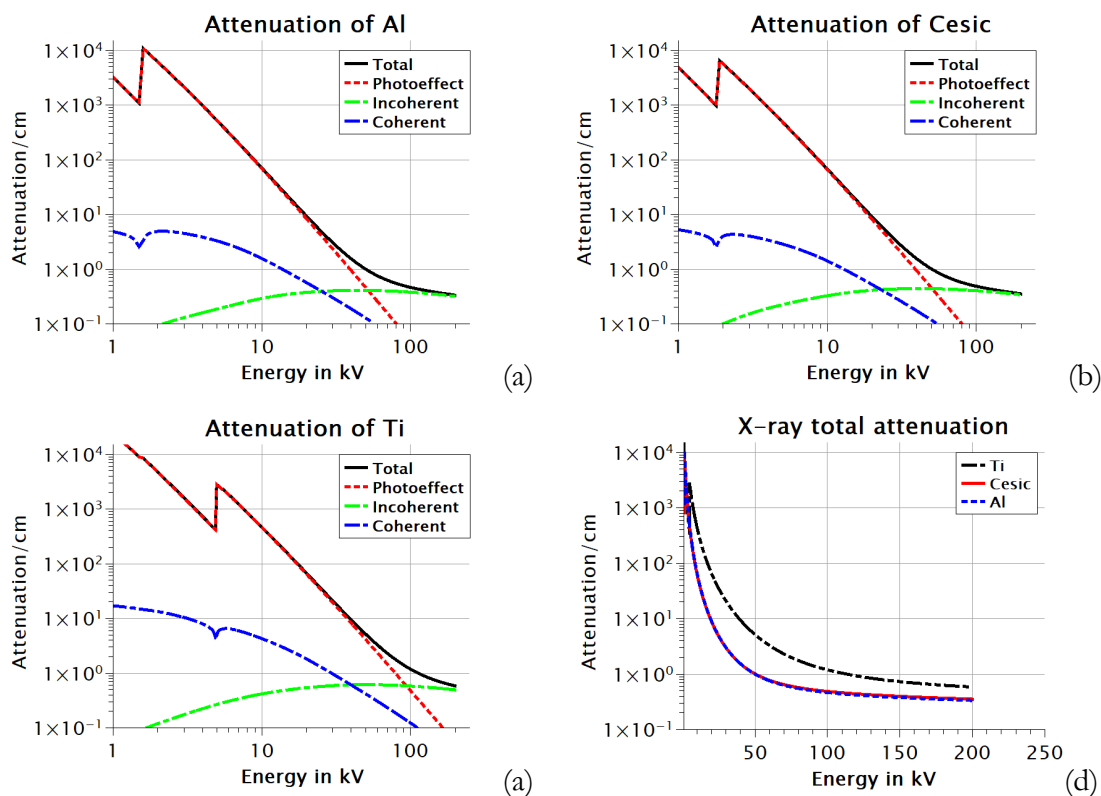


Fig. 3.17. Theoretical attenuation curves of the materials selected for implementation of the multi-material *E*-test: (a) Al; (b) Cesium, (c) Ti and (d) total attenuation of the three materials. (Source: [43,99,100]).

Reference measurements on the multi-material hole cubes

The reference measurements of the MuMat-HC were performed using a tactile CMM Carl Zeiss Prismo Ultra ($E_{0,MPE} = 0.6 + L/500 \mu\text{m}$ and “L” in mm) at PTB. All 17 holes were measured at seven heights (indicated by the groove positions), see Fig. 3.18. For each groove

height, seven circumferential lines at different heights (circumferential lines distance $25\ \mu\text{m}$) were measured inside the holes. The distance of $25\ \mu\text{m}$ in height between the circumferential lines was selected in order to achieve the distances between points smaller than the voxel size (minimum voxel size is approximately $30\ \mu\text{m}$) of CT scans at PTB.

The tactile reference measurements of the cubes were performed using scanning mode with approximately $25\ \mu\text{m}$ sampling distance between points. This results in similar lateral and vertical point distances. In total, around 0.5 million points were obtained from the tactile scanning measurements. A diamond probe was used to avoid contaminating the probe with aluminium, as might occur when using a more common ruby probe.

This measurement approach allows flexible evaluation of the measurands, i.e. the use of single- and multi-point or patch evaluation and improves the comparability between the CMSs. Distances using different measurands (e.g. centre-to-centre, patch-based) were calculated automatically using scripts in the evaluation software GOM Inspect 7.2 [102].

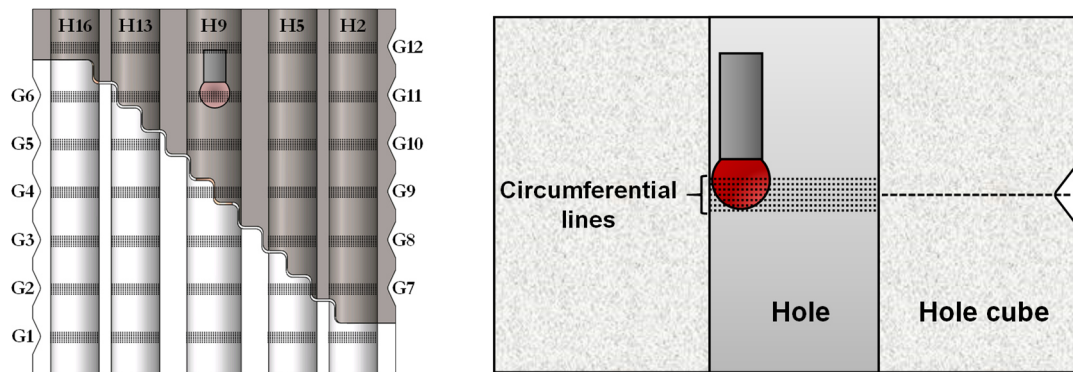


Fig. 3.18. Central cut of the design highlighting the stepwise diagonal cut separating materials, “V”-shaped grooves and calibration strategy, CMM probe (in red) added here for visualization of relative dimensions only.

Data analysis

A simplified workflow of the analysis applied in the multi-material hole cube is depicted in Fig. 3.19. The data analysis of the multi-material E -test is based on the deviation from the tactile reference measurements.

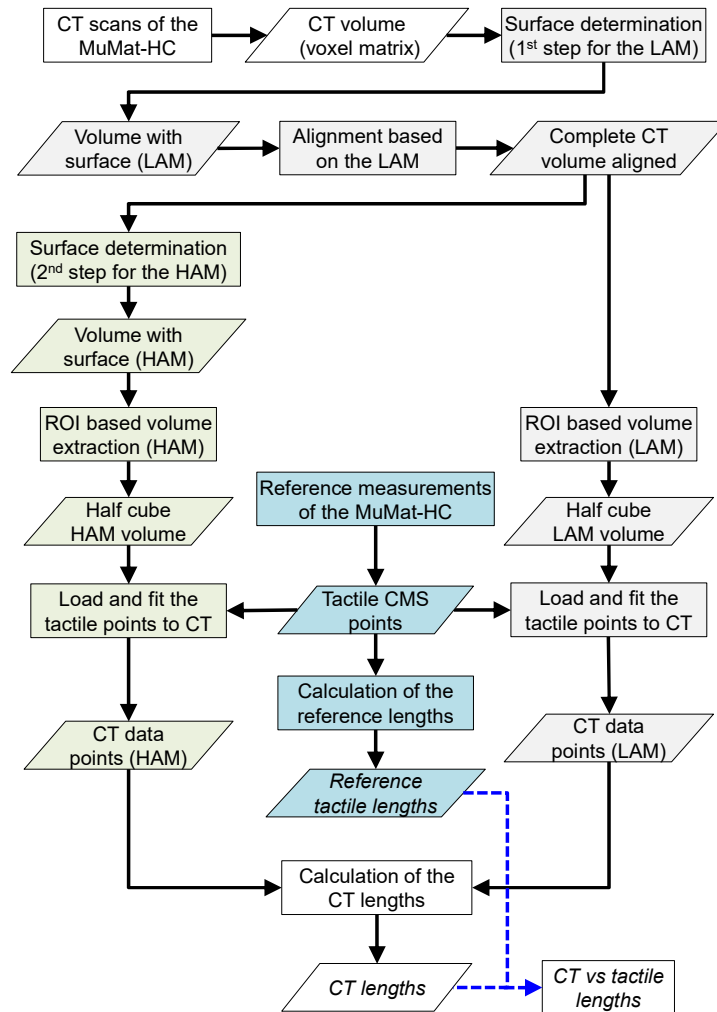


Fig. 3.19. Simplified workflow of the CT measurement of the MuMat-HC.

The alignment procedure as well as the measurement using a strategy identical to the one applied to the tactile reference measurements, allowing comparisons between tactile and CT results to be made. All 17 holes at 7 different heights were measured by CT — similar to the strategy used in the tactile measurements. The points obtained from the tactile measurements were imported and fitted to the CT dataset, i.e. to the CT surface, using VG Studio Max 3.0. The fitting algorithm uses the surface normal vector, representing the tactile probing direction, to search the closest surface of each individual point. Where necessary (i.e. with large attenuation coefficient ratios), the multi-step surface determination procedures (i.e. with two threshold values) was applied to determine the surface of the HAM and LAM independently. The CT dataset was then split in two separate volumes, one containing the LAM and the second containing the HAM. This step was carried out to avoid points being fitted to a poor surface. For example, when the surface is optimised for the HAM, the data points addressed to be fit in the LAM should be excluded.

Comparable results between CT and reference measurements are achieved thanks to the registration procedure. To guarantee an optimal registration of the object, geometrical

elements dependent only on one material were used for the alignment procedure of the MuMat-HC. The alignment of the MuMat-HC is performed as follows:

- Cylinder axis created in H9 (points acquired in one material only) defines the primary datum (+z axis), see Fig. 3.20-a and -b.
- Secondary datum (+y axis) is defined by a line connecting circles H2 and H16. The circles are acquired 2 mm below the top plane, see Fig. 3.20-a and -b.
- The origin of the coordinate system is defined by projecting the symmetry line from the grooves G2, G3, G5 and G6 and the cylinder axis H9. Due to relatively small areas of the grooves planes and to assure a stable registration, the symmetry line is created from the symmetric element between the grooves G2, G3, G5 and G6, see Fig. 3.20-c. The groove lines are created by the intersection line between the two groove planes.

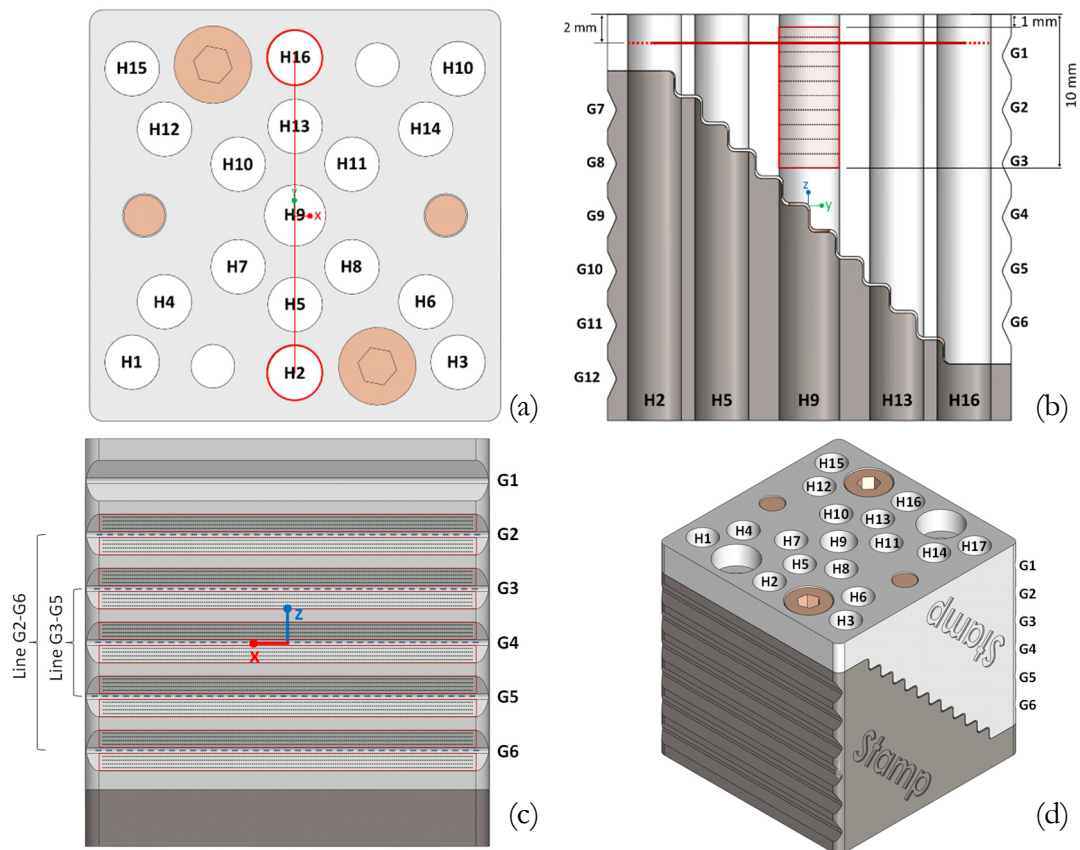


Fig. 3.20. Alignment procedure of the MuMat-HC: (a) top view of the MuMat-HC, cylinder H9 axis defines the +z-axis; (b) Line between the centres of circles H2 and H16 defines +y-axis; and (c) the symmetry lines between the grooves G2, G6 and G3, G5 their intersection with cylinder H9 defines the origin of the coordinate system. (d) Isometric view of the MuMat-HC, hole and groove numbers highlighted. Note: all the elements used for the alignment procedure lie only in one material.

Different length measurands, i.e. bidirectional inner and outer patch-based and centre-to-centre measurements are carried out in the data analysis. Centre-to-centre measurements are evaluated as the distance between two cylinder centres. The cylinder centre represents a point intersecting with a theoretical plane, defined at a specific height (i.e. the nominal heights

of the grooves) and normal to +z axis. The projected point is created by the intersection operation between the least-squares cylinder axis and the theoretical plane.

Additionally, bidirectional length measurements are evaluated as the distance defined by two representative points created through patch operators representing a small area of the hole surface. The steps for the calculation of the representative points created from patch operators are presented in Fig. 3.21.

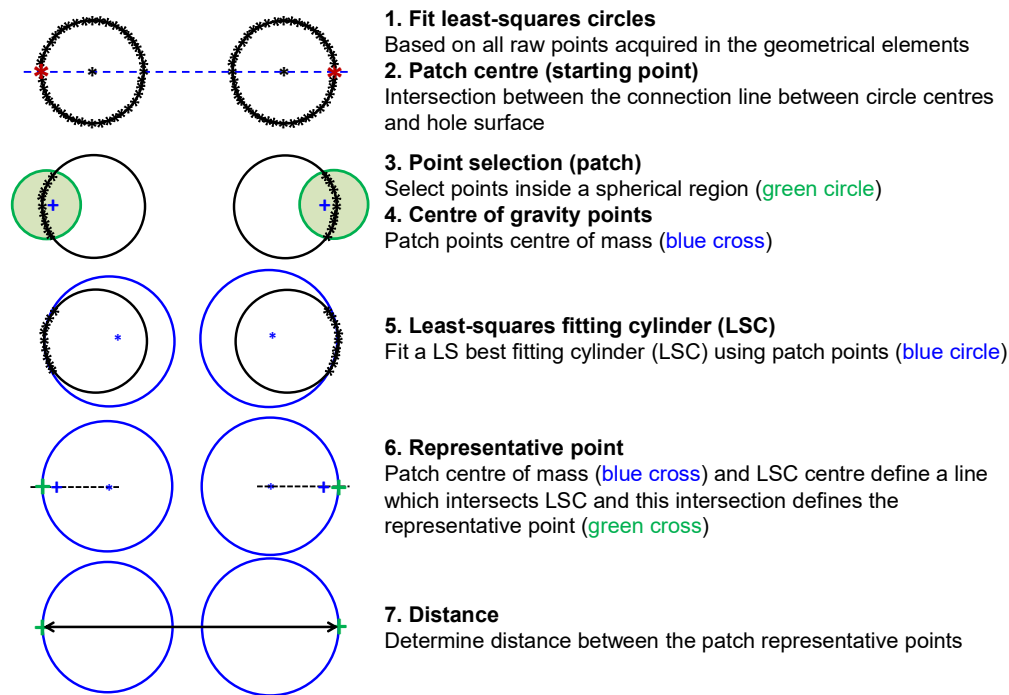


Fig. 3.21. Creation of the patch-based representative points for the uni- and bidirectional length measurements.

3.3.4 Experimental application of the multi-material acceptance test

The main objective of the experimental application of the MuMat acceptance test is to evaluate the performance of a CT system with representative, but also with limited complexity, examples of multi-material measurements. Furthermore, the experiments also serve to assess the test concepts and operability, and the sensitivity of the reference standards to MuMat effects.

The experiments are divided in two parts dealing with application of the MuMat *P*- and *E*-test, respectively. For both *P* and *E*, real CT scans as well as CT simulations were performed, and the measurement results evaluated. The simulation served as a supporting tool for the real measurements and evaluation statements. In total eight experiments are presented, testing different parameters of multi-material measurements and the results are presented in Chapter 4. An overview of the experiments is presented in Table 3.6.

Table 3.6. Overview of the experiments carried out in this thesis.

Experiments of the MuMat <i>P</i> -test		Experiments of the MuMat <i>E</i> -test	
<i>P0</i>	Multi-material local performance of the CT	<i>E0</i>	Multi-material global performance of the CT
<i>P1</i>	Evidence of the necessity of MuMat <i>P</i> -test	<i>E1</i>	Evidence of the necessity of MuMat <i>E</i> -test
<i>P2</i>	Beam hardening correction on the MuMat measurements	<i>E2</i>	Sensibility test on different spectrum energies
<i>P3</i>	Simulation of more extreme MuMat case	<i>E3</i>	Simulation of more extreme MuMat case

The experiments were carried out using the metrological Nikon Metrology MCT225 system of the *Physikalisch-Technische Bundesanstalt* (PTB), Braunschweig, Germany, see Fig. 3.22. The CT system features a reflexive target X-ray source with a maximum acceleration voltage of 225 kV and maximum power of 225 W. In the X-ray source, a tungsten rod is used as anode material and a beryllium window with 2 mm thickness is placed at the aperture of the X-rays source. The manipulator is constructed in an “L”- shaped configuration with 3 translation axes and 1 rotary axis. The system is equipped with a flat panel detector array PerkinElmer 1620 AN3CS with caesium iodine scintillator material and total size of 400 mm x 400 mm with 2000 x 2000 pixels. The detector is protected by a 2 mm thick aluminium sheet on the frontside. The system has a length measurement error specification (MPE_{SD}) of $9 \mu\text{m} + (L / 50) \mu\text{m}$ (L in mm) for centre-to-centre distances.



Fig. 3.22. PTB's Nikon Metrology MCT 225 system used for the experiments.

All the scans were carried out using a circular trajectory and continuous scanning mode. In other words, the rotary table rotates continuously in at a slow pace while X-ray images are acquired. The air temperature measured close to the measurement object, inside the CT cabin, was monitored during all measurements and found to be in the range of $(20.0 \pm 1.0) ^\circ\text{C}$.

Data acquisition and reconstruction were carried out using the proprietary software of the CT system, i.e. Inspect-X Version XT 3.1.9 and CT PRO 3D version XT 3.1.9 from Nikon Metrology, Tring, UK.

The data reconstruction used is based on the FDK algorithm using different reconstruction filters, depending on the experiment. Adaptive local surface determination implemented in the commercial data analysis software for CT VG Studio Max version 3.0, Heidelberg, Germany was used for all the CT datasets.

System qualification steps such as intensity qualification of the flat panel detector was carried out prior to each measurement of the multi-material reference standards. Also, a software-based routine to find the centre-of-rotation axis based on two slices was used to increase the sharpness of the reconstructed image. This routine is an embedded solution implemented in the reconstruction tool provided by the CT manufacturer. It is worth mentioning that the qualification routines were only started after thermal stabilisation of the entire CT system. Special care was given to the X-ray source thermal stabilisation after any changes of the X-ray settings (i.e. voltage and power).

Computed tomography simulations were also performed in this thesis to support the results. The CT simulations were carried out using the software package analytical RT inspection simulation tool “aRTist” from the *Bundesanstalt für Materialforschung und -prüfung*, Berlin, Germany [43,103].

Simulation parameters such as system geometry or X-ray source and detector properties, were chosen to correspond to PTB’s CT system. The adjustment of the simulation tool was performed mainly based on 2D projection images and information obtained from the manufacturer. The free-beam projection was normalised, for example, to the same grey level as the real projection, trying to maximise the use of the dynamic range of the 16 Bit detector. The noise in the projections was likewise compared and tuned in the simulation to similar noise levels (based on the standard deviation of the grey levels) as seen in real CT scans. Detector characteristics e.g. unsharpness and long range unsharpness were also tuned based on the projections. The materials and alloys were simulated based on the elemental compositions, as provided by the suppliers. Similar scanning parameters as used in the real CT scans were used in the simulations. The data reconstruction of the simulations was carried out using the reconstruction solution implemented in the PTB’s CT system to improve comparability of the results between real CT scans and simulations.

Experimental application of the multi-material *P*-test

Four experiments, presented in Table 3.6, were carried out to evaluate the multi-material influence on the probing error test; to evidence the necessity of the MuMat *P*-test; to assess

the influence of beam hardening effects on the MuMat probing measurements; and to study more difficult multi-material combinations using simulation.

For all CT scans and simulations, the test spheres were all positioned with the glue-gap parallel to the CT's rotational axis. All scans were performed at a magnification of 2.4 times, leading to a voxel size of $(82.5 \mu\text{m})^3$, with 1200 projections.

Diameter and form error of the test spheres were assessed based on the 4 metrological characteristics presented in section 3.2.3. To avoid mounting-related errors, the data evaluation was carried out on each half sphere separately, as also presented in §3.2.3.

Experiment P0: Local multi-material performance of the CT-based CMS

All the compound test spheres were CT scanned to verify the local performance of the system by multi-material measurements. The test comprised measuring three multi-material test spheres, but three mono-material test spheres as well. The first was to verify the multi-material influence on the probing error test when measuring objects with high, moderate and low-moderate attenuation coefficient ratios, cf. Table 3.1. The mono-material compound spheres served as references and verification for the multi-material spheres and also to demonstrate that the half spheres design is not significantly affected by the cutting/gluing, and therefore appropriate for the proposed test.

The scanning parameters, which are reported in Table 3.7, were selected for each assembly to maintain similar noise levels and constant focal spot size in the measurements.

Table 3.7. CT scanning parameters used for each mounted MuMat and MoMat sphere.

Parameter	Unit	Si ₃ N ₄ & Al ₂ O ₃	Si ₃ N ₄ & N-SF6	Al ₂ O ₃ & N-SF6	Si ₃ N ₄ & Si ₃ N ₄	Al ₂ O ₃ & Al ₂ O ₃	N-SF6 & N-SF6
Voltage	kV	200	225	225	200	200	225
Current	μA	90	80	80	90	90	80
Power	W	18	18	18	18	18	18
Cu filter thickness	mm	0.25	1	1	0.25	0.25	1
Exposure time	ms	708	1415	1415	708	708	1415
Scan time	min	14.2	28.3	28.3	14.2	14.2	28.3
Beam hardening correction		None	None	None	None	None	None

Form and size measurements — based on the four metrological characteristics: $P_{\text{Form.MuMa.Sph.1x25:CT}}$, $P_{\text{Form.MuMa.Sph.D95%:CT}}$, $P_{\text{Size.MuMa.Sph.1x25:CT}}$, and $P_{\text{Size.MuMa.Sph.All:CT}}$ described in § 3.2.3 — were carried out with all six compound spheres. The data analysis was carried out for each HS separately using VG und Matlab, as depicted in Fig. 3.12.

Additionally, the test value uncertainty of the CT experiments was considered. The suitability of the multi-material P -test is verified by the test value uncertainty. To be considered a suitable test, the test value uncertainty should be relatively small compared to the uncertainty of the system itself. The evaluation of the test value uncertainty is based on the ISO/TS 23165:2006 technical specification [96]. According to this, the test value uncertainty concept is an approach to evaluate the expanded uncertainty of a test associated solely with the testing equipment and its use in that test, cf. §2.3.2. The concept is mainly applied to decision-making when performing acceptance testing of tactile CMSs according to the standard ISO 10360-2 [97], see *Derivation of the MuMat P-test results*. Since the potential effects in the test are considered and quantified as an uncertainty contributor, the test uncertainty expresses how accurate the testing process is. Nevertheless, the experimental test setup presented in this work represents a similar setup to the test proposed in the ISO 10360-2 standard. Some differences can be observed, e.g. the test is performed on the multi-material spheres, and therefore the uncertainty estimation procedure has to be adapted to the present case. The standard uncertainty of the error of indication, for size $u(P_S)$ and form $u(P_F)$, was defined taking inspiration from the ISO/TS 23165 according to Eq. (3.7) and (3.8), respectively.

$$u(P_S) = \sqrt{\left(\frac{F}{2}\right)^2 + u^2(F) + u^2(\varepsilon_\alpha) + u^2(\varepsilon_{\text{Samp}}) + u^2(\varepsilon_t) + u(b)} \quad (3.7)$$

$$u(P_F) = \sqrt{\left(\frac{F}{2}\right)^2 + u^2(F) + u^2(\varepsilon_{\text{Samp}})} \quad (3.8)$$

where:

- F form error of the standard, stated in the calibration certificate
- $u(F)$ standard uncertainty of the form error, stated in the calibration certificate
- ε_α error due to the input value of the coefficient of thermal expansion (CTE) of the standard
- ε_t error due to the input value of the temperature
- $\varepsilon_{\text{Samp}}$ error due to the incomplete sampling of the sphere
- $u(b)$ uncertainty associated with the correction of systematic errors e.g. voxel size correction.

F is directly obtained from the reference measurements of the compound spheres, as is $u(F)$. The CTE value can be obtained from the manufacturer datasheets and the uncertainty of the CTE value is often unknown. In this case, the guideline VDI/VDE/DGQ 2618

part 1.2:2003-12, could be followed, where a minimum range of 20% of the nominal value should be used as a rectangular distribution [104]. The ε_t contribution is usually zero in all relevant cases in acceptance testing [96], since all the rated conditions shall be met during the test. For the experiments carried out in this thesis, no rated condition of temperature was stated; thus, the contribution of the temperature in the test measurements was considered as an uncertainty contributor. In theory, two materials creating a compound sphere have different CTEs, leading to different expansion of the HS and varying their size differently. However, in the experiments presented in this paper, a change in the temperature caused an expansion of the workpiece, which impaired the results. Therefore, ε_t was estimated based on reference measurements of the temperature sensor and the variation of the spheres size was carried out considering the material with largest CTE. ε_{samp} is the uncertainty contribution associated with the incomplete sampling of the spheres. Due to the design of the compound spheres, only part of the half spheres is probed. Therefore, the uncertainty contribution cannot be equal to zero. The uncertainty was estimated using a software developed in-house (SphereFit) and it uses the method described in [105]. A scale correction based on measurements of a multi-sphere standard before and after every measurement of the compound spheres was carried out to correct for the voxel size of the CT measurements. The uncertainty of this correction is included in the test value uncertainty. Therefore, the uncertainty of the multi-sphere standard was included as an uncertainty contribution $u(b)$. The test value uncertainty budget for form and size of the multi-material P -test is shown in Table 3.8.

Table 3.8. Test value uncertainty representing the worst-case contributions considered in the multi-material P -test.

		Size	Form
F	μm	0.5	0.5
$u(F)$	μm	0.5	0.5
$u(\varepsilon_\alpha)$	μm	0.0005	
$u(\varepsilon_{samp})$	μm	0.001	0.001
$u(\varepsilon_t)$	μm	0.04	
$u(b)$	μm	0.25	
$U(P)$	μm	1.3	0.7

Experiment $P1$: Necessity of the multi-material P -test

To demonstrate the utility of the multi-material P -test, two mono-material (Si_3N_4 & Si_3N_4 and N-SF6 & N-SF6) and one multi-material (Si_3N_4 & N-SF6) compound spheres were

measured and compared. The measurements were carried out using the corresponding scanning parameters presented in Table 3.7. The comparison between the compound sphere results is carried out using a statistical hypothesis test, Welch's test [106], based on five repeated measurements of the compound spheres.

In this experiment, half spheres made of the same material, but mounted in different compound spheres were compared statistically, as schematically presented in Fig. 3.23. This experiment should demonstrate that multi-material effects present in the multi-material assembly are not present in the mono-material compound sphere so that, the utility of the multi-material P -test can be confirmed. A further objective of this statistical experiment was to verify if the standard design influences the measurement results. The comparison was based on four quantities for size and form as presented in § 3.2.3.

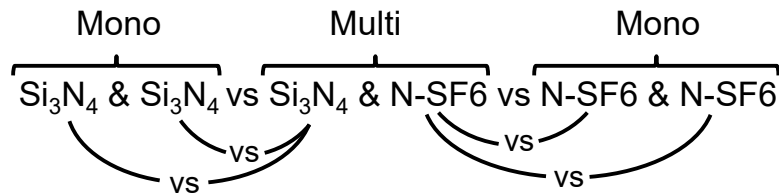


Fig. 3.23. Schematic of experiment $P1$. Half spheres made of the same material but mounted in different compound spheres are statistically compared.

The statistical Welch's test is based on two hypotheses: the null hypothesis (H_0) assumes that the averages based on the five repetitions (of each metrological characteristic) of each half sphere made of same material but mounted in different compound spheres are equal, see Eq. (3.9). The alternative hypothesis (H_1) assumes that the HSs averages are different, see Eq. (3.10).

$$H_0: \bar{X}_1 - \bar{X}_2 = 0 \quad (3.9)$$

$$H_1: \bar{X}_1 - \bar{X}_2 \neq 0 \quad (3.10)$$

Assuming two-tailed distributions for both samples, H_0 can be rejected, if the Welch's number, t_w , is bigger than tabled t -student number for a significance level of $\alpha = 95\%$ and ν degrees of freedom.

H_0 can be rejected, if:

$$t_w > t\text{-student}_{\alpha,\nu} \quad (3.11)$$

Rearranging Eq. (3.11), the normalised deviation is obtained in Eq (3.12).

$$\text{Normalised deviation} = t_w / t\text{-student}_{\alpha,\nu} \quad (3.12)$$

The Welch's t -test defines the statistic t_w by the Eq. (3.13):

$$t_W = \frac{\bar{X}_1 - \bar{X}_2}{\sqrt{\frac{s_1^2}{N_1} + \frac{s_2^2}{N_2}}} \quad (3.13)$$

Where \bar{X}_1 and \bar{X}_2 are the averages, s_1 and s_2 the standard deviations calculated from the five repeated measurements N_1 and N_2 are the number of repeated measurements, in this case, five.

The degrees of freedom, ν , used for the tabled t-student number is calculated based on Eq. (3.14).

$$\nu = \frac{\left(\frac{s_1^2}{N_1} + \frac{s_2^2}{N_2}\right)^2}{\frac{s_1^4}{N_1^2 \nu_1} + \frac{s_2^4}{N_2^2 \nu_2}} \quad (3.14)$$

Where the degrees of freedom associated with the standard deviations of sample 1 and 2, respectively.

H_0 can be rejected with 95% reliability if the normalised deviation, Eq. (3.12), is greater than 1, meaning that the alternative hypothesis can be accepted. The deviation is normalised with the tabled t-student factor (for ν , α), where ν is the number of degrees of freedom and α is the reliability factor for a unimodal distribution (considered only the absolute difference between the averages). Similar to the standard hypothesis test “t-test”, the Welch’s test assumes normal distributions for the compared samples, however different variances. This is the main difference to the standard t-test [106].

Experiment P2: Beam hardening influence on the multi-material probing error test

The influence of beam hardening on multi-material P -test measurements was verified. Beam hardening is an X-ray attenuation-related effect, and it can have a significant influence on multi-material measurements. A soft beam hardening correction⁵ (BHC) was applied to the measurements of the multi-material compound sphere (i.e. Si_3N_4 & N-SF6). Form and size measurements were carried out in the datasets with and without BHC and statistically compared. It is worth to remark that no new CT scans were performed, i.e. the five repeated measurements used in experiment P1 were also used in experiment P2. The datasets of the MuMat-sphere were reconstructed again using different BHC settings.

⁵ Nikon Metrology CT PRO 3D version 3.1.9 standard beam hardening correction based on a polynomial function of order 2 (soft) was carried out during the reconstruction of the projections.

The averages of the five repeated measurements with and without BHC are compared using the same statistical Welch's test as used in experiment *P1*.

Experiment *P3*: Simulation of the more difficult multi-material combination for the *P*-test

The main objective of the experiment *P3* was to extend the MuMat probing error test to multi-material combinations with lower attenuation coefficient ratios than used in the real CT scans, e.g. by including iron (Fe) and polymers e.g. polyether ether ketone (PEEK). The same compound sphere design is also used in the simulations.

The experiment consisted of two parts. (a) Verification of the simulation tools; and (b) simulation of a more extreme multi-material case. In (a) the verification of the simulation tool was carried out by comparison between real CT scans and simulations. Two mono-material and one multi-material compound spheres (i.e. Si_3N_4 & Si_3N_4 , N-SF6 & N-SF6 and Si_3N_4 & N-SF6) were simulated and compared with the corresponding real CT measurements. In (b), more extreme multi-material combinations were simulated. The polymer PEEK was paired with Si_3N_4 , N-SF6 and Fe to verify the CT behaviour when measuring more extreme multi-material combinations and to demonstrate the general concept. With these multi-material combinations, moderate, moderate-low and low attenuation coefficient ratios are obtained.

Experimental application of the multi-material *E*-test

Four experiments were carried out using the hole cube standards to evaluate the multi-material influence on the length measurement error test. This is to demonstrate the necessity of the MuMat *E*-test, to depict the sensibility of the MuMat *E*-test and simulation-based experiments covering more difficult multi-material combinations.

For all scans and simulations, the multi-material hole cube standards were positioned with the hole axis in parallel to the rotational axis of the CT system, to approximately maintain a constant X-ray penetration length for each groove (height). All scans were performed with the same magnification of six times, which leads to a voxel size of $(30 \mu\text{m})^3$, and 2500 projections. For all CT scans, residual scaling errors were reduced by a voxel size re-scale, to improve the accuracy of the analyses. The scale correction was based on the 2D approach published in [14].

Distances between all 17 holes in seven different heights were measured in the hole cubes standards. The evaluation was based on in-, inter- and mono-material measurements evaluated as bidirectional inner and outer lengths as well as centre-to-centre measurements. Approximately 780 distances were evaluated for each hole cube. The bidirectional lengths were measured based on representative points created with patch operators, as presented in

Fig. 3.21. Patch points were selected with a spherical selection tool with a radius of 0.9 mm to represent a small section of the cylinder. The selected region included approximately 15% of the whole cylinder. The workflow from data acquisition to the characterisation of the feature was performed as presented in Fig. 3.19.

Experiment *E0*: Multi-material influence on the length measurement error test

The MuMat-HC standards were scanned to evaluate the multi-material influence on the length measurement error test. All six reference standards consisting of three MoMat-HCs and three MuMat-HCs were measured. The evaluation was based on differences between CT and tactile measurements of lengths measured as centre-to-centre, bidirectional inner and outer.

The CT scanning parameters — shown in Table 3.9 — were selected for each hole cube individually, in order to reduce beam hardening artefacts and yield similar noise level for all scans.

Table 3.9. CT scanning parameters used for the hole cube standards in experiment *E0*.

Parameter	Unit	Al & Cesic	Cesic & Ti	Al & Ti	Al & Al	Cesic & Cesic	Ti & Ti
Voltage	kV	200	225	225	200	200	225
Current	μA	75	110	150	169	75	150
Power	W	15	25	33.8	33.8	15	33.8
Filter material		Cu	Ag	Ag	Cu	Cu	Ag
Filter thickness	mm	1	1	1	1	1	1
Exposure time	ms	2829	4000	2000	708	2829	4000
Images to average		1	1	2	1	1	1
Scan time	min	141	200	167	30	141	167
Gain	dB	24	24	24	24	24	18
Beam hardening correction		none	soft	soft	none	none	soft

The test value uncertainty of the experiments by CT was estimated. The standard uncertainty of the error of indication, $u(E)$, was defined taking inspiration from the ISO/TS 23165 according to Eq. (3.15).

$$u(E) = \sqrt{u^2(\varepsilon_{cal}) + u^2(\varepsilon_{\alpha}) + u^2(\varepsilon_t) + u^2(\varepsilon_{alig}) + u^2(\varepsilon_{fix}) + u^2(\varepsilon_{samp}) + u(b)} \quad (3.15)$$

where:

ε_{cal} calibration error of the standard

ε_{α} error due to the input value of the CTE of the standard

ε_t error due to the input value of the temperature of the standard

3.3. Verification concept

ε_{align}	error due to alignment/registration procedure used
ε_{fix}	error due to fixturing of the standard
ε_{samp}	error due to sampling strategy in the geometrical elements
$u(b)$	uncertainty associated to the correction of systematic errors e.g. voxel size correction.

$u(\varepsilon_{cal})$ is directly obtained by the reference measurements of the multi-material spheres, divided by the coverage factor. The CTE value can be obtained from the manufacturer datasheet and the uncertainty of the CTE value is usually unknown. In this case, the guideline VDI/VDE/DGQ 2618 part 1.2, could be followed, where a minimum range of 20% of the nominal value should be used as a rectangular distribution [104]. In the experiments presented in this thesis, a change in the temperature causes an expansion of the workpiece, which causes a change in the lengths. The uncertainty due to (ε_t) was considered for each material separately. The contribution from the alignment procedure (ε_{align}) was calculated based on preliminary tests, where datasets were re-aligned and the longest lengths in three different (H1-H3, H1-H15 and H1-H17) directions measured. The maximum variation of this experiment in the lengths was used as uncertainty contribution. For the $u(\varepsilon_{fixt})$, no significant clamping force was used to clamp the multi-material cubes, therefore no significant effect was considered. $u(\varepsilon_{samp})$ is the uncertainty contribution associated with the sampling of the cylinders (for centre-centre length measurements) and representative points (for bidirectional length measurements). For the centre-centre measurements, $u(\varepsilon_{samp})$ was considered negligible, since the probed points, used to fit the geometrical elements, were evenly distributed over the complete cylinders. However, due to the nature of the patch-based bidirectional measurement sampling strategy, i.e. only part of the cylinders are used to create the representative points, the uncertainty contribution cannot be neglected. The uncertainty was estimated experimentally where the longest length in the cube were repeatedly measured (i.e. 10 repetitions) in the same dataset and the largest deviation between the measurements was taken as the uncertainty contribution. $u(b)$ was directly obtained by the calibration certificate of the standard (i.e. hole foil) used for the correction of the voxel size. A simplified test uncertainty budget is presented in Table 3.10.

Table 3.10. Test value uncertainty estimation of the length measurements

	unit	Centre-centre	Bidirectional
$\mathbf{u(cal)}$	μm	0.75	1
$\mathbf{u(\alpha)}$	μm	0.001	0.001
$\mathbf{u(t)}$	μm	0.028	0.028
$\mathbf{u(align)}$	μm	0.2	0.3
$\mathbf{u(fix)}$	μm	0	0
$\mathbf{u(samp)}$	μm	0	0.1
$\mathbf{u(b)}$	μm	0.25	0.25
$\mathbf{U(E)}$	μm	1.6	2.1

Experiment *E1*: Necessity of the multi-material length measurement error test

The objective of the experiment *E1* is to demonstrate that multi-material effects — observed in a multi-material cube — do not occur in mono-material measurements. The experiment consists of measuring three hole cubes — two MoMat (Al & Al and Ti & Ti) and a MuMat (Al & Ti) — five times each. The scanning parameters used in experiment *E0* (reported in Table 3.9) were also used in *E1* for each respective cube. With assistance of the CT simulation tool, i.e. aRTist, BAM, Berlin, the scanning parameters, presented in Table 3.10, were selected to yield for each assembly, similar contrast-to-noise-ratios in the reconstructed volumes and same focal spot size, while minimising beam hardening effects.

The cubes were scanned with the hole axis parallel to the rotary axis and for every repetition, they were repositioned (i.e. removed and replaced) on the rotary table. Likewise, the magnification axis as well as the height axis of the CT manipulator system were randomly moved out of position and repositioned. Scale correction based on a 2D method was applied, aiming to reduce residual systematic errors and improve the measurement accuracy.

The evaluation was based on differences between CT and tactile measurements of lengths measured as centre-to-centre, bidirectional inner and outer distances.

All lengths were statistically compared by means of the hypothesis test — Welch’s test. The test was applied to demonstrate the utility of the MuMat-test by showing significant a difference between averages based on the five repeated measurements of each cube. The length measurements in the cube Al & Ti were compared to the corresponding lengths in cubes Al & Al and Ti & Ti.

The null hypothesis, which states that both averages are equal, can be rejected if the Welch’s number, t_w (Eq. (3.11)), is bigger than number of t -student for a significance level of $\alpha = 95\%$ and ν degrees of freedom. Two-tailed distributions of both samples are considered.

Experiment *E2*: Sensibility verification of the test for the multi-material effects

The experiment *E2* intended to verify the sensibility of the proposed multi-material *E*-test to multi-material effects and to evidence the dependency of the multi-material effects on the X-ray spectrum. The MuMat cube with lowest attenuation coefficient ratio (i.e. Al & Ti) was scanned with three different X-ray spectra. Each set-up was measured five times. The scanning parameters were selected to produce significant difference in the X-ray spectrum, see Table 3.11.

Table 3.11. CT scanning parameters used for the hole cube Al & Ti measured with different X-ray spectra in experiment *E2*.

Parameter	Unit	Spectrum 1	Spectrum 2	Spectrum 3
Voltage	kV	225	200	175
Current	μ A	150	169	192
Power	W	33.8	33.8	33.6
Filter material		Ag	Cu	Cu
Filter thickness	mm	1	2	0.5
Exposure time	ms	2000	1415	500
Images to average		2	1	1
Scan time	min	167	60	21
Gain	dB	24	24	24

Similar to experiment *E1*, the results of the cube measurements with varied X-ray spectra were statistically compared using the Welch's statistic. However, in *E2*, \bar{X}_1 and \bar{X}_2 in Eq. (3.9) are the averages of two measurements with different X-ray spectra.

The measurements of the Al & Ti cube with three spectra were compared in pairs, each scan was compared to each of the others, see Fig. 3.24.

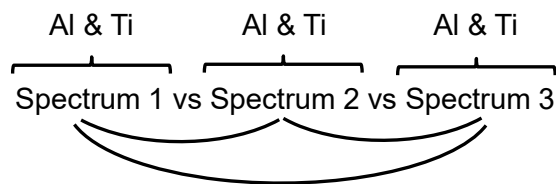


Fig. 3.24. Comparison scheme of experiment *E2*. Measurements based on different spectra are compared.

Experiment *E3*: Simulation of the more difficult multi-material combination for the *E*-test

The main objective of experiment *E3* was to extend the MuMat length measurement error test to multi-material combinations, featuring lower attenuation coefficient ratios than the real CT scans, e.g. with Fe and PEEK. The simulations used the design of the hole standard.

The experiment consists of two parts. (a) Verification of the simulation tools; and (b) simulation of more extreme multi-material case. In (a) the verification of the simulation tool was carried out by comparison between real CT scans and simulations. Two mono-material

and one multi-material compound spheres (i.e. Si_3N_4 & Si_3N_4 , N-SF6 & N-SF6 and Si_3N_4 & N-SF6) were simulated and compared with the corresponding real CT measurements. Whereas in (b), more extreme multi-material combinations were simulated. The polymer PEEK was paired with Al, Ti and Fe to verify the CT behaviour when measuring more extreme multi-material combinations. With these multi-material combinations, moderate, low-moderate and low attenuation coefficient ratios were obtained.

(a) Simulation of the same setups to evaluate the simulation software.

Simulation vs real CT measurements of:

- Al & Ti
- Al & Al
- Ti & Ti

(b) Simulation of a more difficult case including Fe and PEEK

- PEEK & Al
- PEEK & Ti
- PEEK & Fe

3.4 Summary and conclusion of the chapter

In this chapter an acceptance test focused on evaluating the performance of CT-based CMSs for multi-material measurements was successfully proposed. The test proposal was divided into three phases: (1) definition of test requirements, (2) conceptual development of multi-material acceptance test and (3) conceptual development of the verification of the proposed multi-material test.

In (1), the demands of the proposed multi-material test considering the specifics of multi-material measurements with CT-based CMSs were defined. An important requirement of the test is that the proposed test should follow the concepts of the ISO 10360 series of international standards. In (2), the concepts of the multi-material test were defined. Concepts from existing standards were applied and adapted to multi-material acceptance testing. Besides this, new concepts were created. A fundamental concept for multi-material performance of a CMS should evaluate the probing error and length measurement error test, to be assessed on the basis of test measurements of multi-material standards. The test measurements shall be carried out under specified rated operating conditions, considering the specifics of multi-material measurements. Specification requirements, describing rated operating conditions, which CT manufacturers should provide along with the system specifications for the multi-material characteristic of the CMS was created as well. These specification requirements consider conditions specific to multi-material measurements.

Examples would be permissible material and material thickness. (3) At the end of this chapter, multi-material standards were designed, manufactured, calibrated, and then measured and simulated with CT-based CMS to verify if the proposed test fulfils all test requirements. In other words, to check if the proposed test fulfils its intended purpose. Eight experiments using up to 12 multi-material standards were described, testing e.g. the sensibility of the multi-material length measurement error test to multi-material effects, or the influence of beam hardening on the multi-material probing error test. Two novel designs of multi-material reference standards — for *P*- and *E*-test — were presented and tested in this work.

Ultimately, an acceptance test suitable for evaluating the multi-material performance of CT-based CMSs was successfully developed.

In the next chapter, measurements and simulation results from the different experiments using the novel multi-material standard are presented and discussed.

Chapter 4: Results

The results of the experiments described in § 3.3.4 are presented in this chapter. The underlying objective of this experimental investigation was to verify whether the proposed and implemented test fulfils its requirements.

4.1 Results of multi-material sphere measurements (*P*-test)

Four experiments were carried out using the novel multi-material compound spheres. Three of them were based on real measurements performed in the PTB's metrological CT system. One experiment was based on simulations, where the software package aRTist, developed at BAM, Berlin [103], was used.

4.1.1 Results of experiment *P0*: Local multi-material performance of the CT-based CMS

The local multi-material performance of the PTB's CT-based CMS was evaluated by means of test measurements of all six compound spheres created for this thesis, see § 3.3.2. The measurement results of form and size based on the four metrological characteristics described in section 3.2.3 are presented in Fig. 4.1.

In the plots, the results of single measurements of the MoMat sphere made from Al_2O_3 & Al_2O_3 and the MuMat spheres made from Si_3N_4 & Al_2O_3 and Al_2O_3 & N-SF6 are shown. For the remaining spheres, i.e. N-SF6 & N-SF6, Si_3N_4 & Si_3N_4 and Si_3N_4 & N-SF6, the average of five repeated measurements are plotted. The repetitions served as a basis for statistical analyses carried out in the following experiments (i.e. experiments *P1* and *P2*). In the plots, bars with the same colour are the results of two HSs of the same compound sphere. To avoid double naming, the halves of the mono-material spheres are labelled as HS1 and HS2, and the halves of the multi-material spheres are labelled indicating whether the respective half is LAM or HAM. The error bars plotted on each measurement result represent the worst-case test value uncertainty estimated as described in § 3.3.4. A simplified notation of the *P*-test characteristics: $\text{PF}_{25} = P_{\text{Form.Sph.1x25::CT}}$, $\text{PF}_{95} = P_{\text{Form.Sph.D95%::CT}}$, $\text{PS}_{25} = P_{\text{Size.Sph.1x25::CT}}$, and $\text{PS}_{\text{all}} = P_{\text{Size.Sph.All::CT}}$ is used.

4.1. Results of multi-material sphere measurements (P-test)

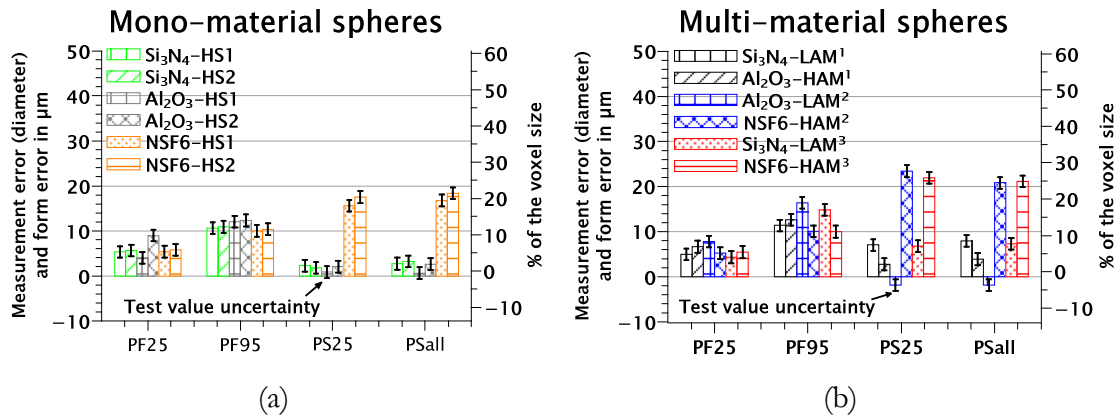


Fig. 4.1. *P*-test measurements, (a) mono-material spheres, HS = half sphere; (b) multi-material spheres. Error bars plotted on the charts, represent estimated worst-case test value uncertainty calculated for the *P*-test in § 3.3.4.

The results of measurement error of size and form deviation of all compound spheres were below a half voxel size. The HS made of the LAM (i.e. Si_3N_4 and Al_2O_3) in assemblies with moderate and low-moderate attenuation ratio (i.e. Si_3N_4 & N-SF6 and Al_2O_3 & N-SF6) suffer a degradation of the form measurements, for PF95, see Fig. 4.1-b. In other words, the HAM HS (N-SF6) impacted negatively the results of the LAM HS, since the measured form error on the LAM HS was increased approximately 1.5 times. This effect was confirmed by MoMat-sphere measurements (Fig. 4.1-a), and by the MuMat-sphere with high attenuation ratio (i.e. Si_3N_4 & Al_2O_3). In these cases, the measurements of both HSs of a single compound sphere resulted similar form errors. In form measurements using 25 patch-based representative points, no significant effect was observed, presumably due to the strong data averaging.

The multi-material effect appears to affect size measurements as well. The effect becomes clear when the results of the MuMat spheres with moderate and low-moderate attenuation coefficient ratio are compared with the MoMat spheres. In Fig. 4.1-a, the Si_3N_4 & Si_3N_4 sphere of size measurements presented measurement error of approximately 2 μm and 3 μm , for PS25 and PSall, respectively. Meanwhile for half spheres made of Si_3N_4 (LAM) when measured with a high absorbing material (i.e. NSF-6), the measurement error of size increased to approximately 7.5 μm for PS25 and PSall.

Lastly, multi-material effects were observed in the *P* test measurements. The effects were supported by the MoMat-spheres measurements, as the measurements (on each HS of a compound MoMat-sphere) presented similar results. No significant multi-material effects were observed in the multi-material combinations with high attenuation coefficient ratio (i.e. HSs made of similar attenuation coefficients). The results obtained with the high attenuation ratio MuMat-sphere (Si_3N_4 & Al_2O_3) were comparable to the results obtained with the MoMat compound spheres. In addition, the observed multi-material effects are significantly

greater than the estimated test value uncertainty. These results indicate that the test and compound sphere design are well-suited to evaluating the probing error performance of the system.

4.1.2 Results of experiment *P1*: Necessity of the multi-material *P*-test

The need for the MuMat *P*-test was confirmed by showing that multi-material effects seen in the MuMat measurements do not occur in the MoMat-sphere measurements. The multi-material influence on the size and form measurements was verified by five repeated measurements of three compound spheres (two mono- and a multi-material). The average and standard deviation of the measurements of each compound sphere are shown in Fig. 4.2. Each half sphere was measured separately. Thus, bars with the same colour are the results of two HSs of the same compound sphere.

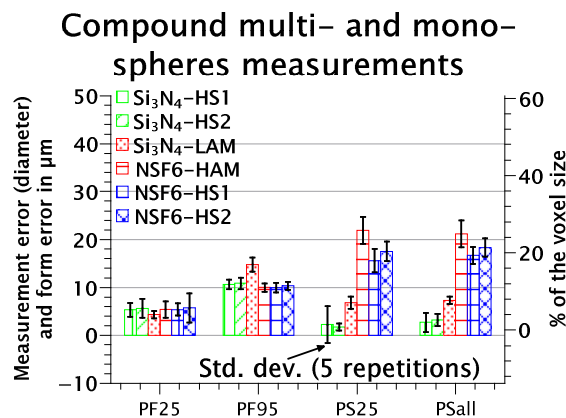


Fig. 4.2. Average (bars) and standard deviation (error bars) of five repeated measurements on two compound MoMat spheres (i.e. Si₃N₄ & Si₃N₄ and N-SF6 & N-SF6) and one MuMat sphere (i.e. Si₃N₄ & N-SF6).

The average of the repetitions was compared with each other using the statistical hypothesis (Welch's) test [106]. The hypothesis test compares the measurements of a multi-material sphere with two mono-material spheres. The LAM half of a MuMat sphere was compared with both LAM halves of a MoMat sphere. Likewise, the HAM half of a MuMat sphere was also compared with both HAM halves of a MoMat sphere. The results are shown in Fig. 4.3.

The plotted normalised deviations were calculated based on the Welch's number and the tabled t-student number according to Eq. (3.12). Interpreting the statistical tests: when the result of the normalised deviation is greater than one, the null (equivalence) hypothesis can be rejected, and the alternative (difference) hypothesis can be accepted. In other words, the hypothesis of equality of both averages can be rejected and the hypothesis of inequality can be accepted with 95% reliability.

4.1. Results of multi-material sphere measurements (P-test)

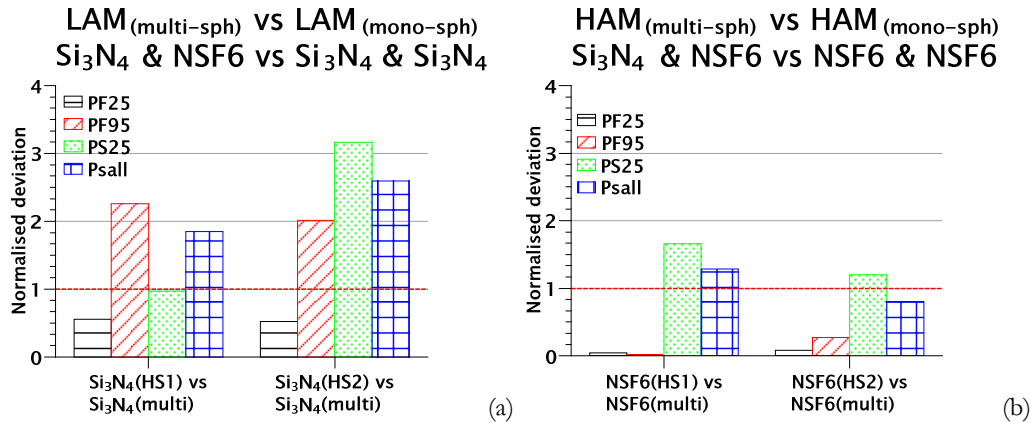


Fig. 4.3. Statistical Welch's test comparing two half spheres (made of the same material) of different compound spheres: comparison between the HS made (a) Si₃N₄ (MuMat) vs Si₃N₄ (MoMat); (b) NSF6 (MuMat) & NSF6 (MoMat).

The hypothesis test confirms the significance of the effects observed in the experiment *P0*, since the normalised deviation for PF95 measured in the halves made of LAM (i.e. Si₃N₄) is greater than one, see red bars in Fig. 4.3-a. The size measurements of the LAM halves appear to be significantly affected by the presence of the HAM (i.e. N-SF6), this was also confirmed statistically. Size measurements of the halves made of HAM in a MuMat-sphere also showed statistical difference when compared with the half made of HAM in a MoMat-sphere, see Fig. 4.3-b. This indicates that the LAM affects the size measurements of the HAM as well, but not the form.

From experiment *P1*, it can be concluded that the HAM degrades especially the form (PF95) and also, but less, the size measurements (PS25 and PSall) of the LAM and the LAM affects the size measurements of the HAM.

4.1.3 Results of experiment *P2*: Beam hardening influence on the multi-material *P*-test

The influence of a beam hardening correction method on the multi-material measurements was evaluated in experiment *P2*. A beam hardening correction method implemented in the PTB's CT system reconstruction software (CT PRO 3D Version XT 3.1.9) was applied to five repeated measurements of the sphere with the lowest attenuation coefficient ratio (i.e. Si₃N₄ & N-SF6). The average and standard deviation for form and size of the measurements with and without beam hardening correction are plotted in Fig. 4.4.

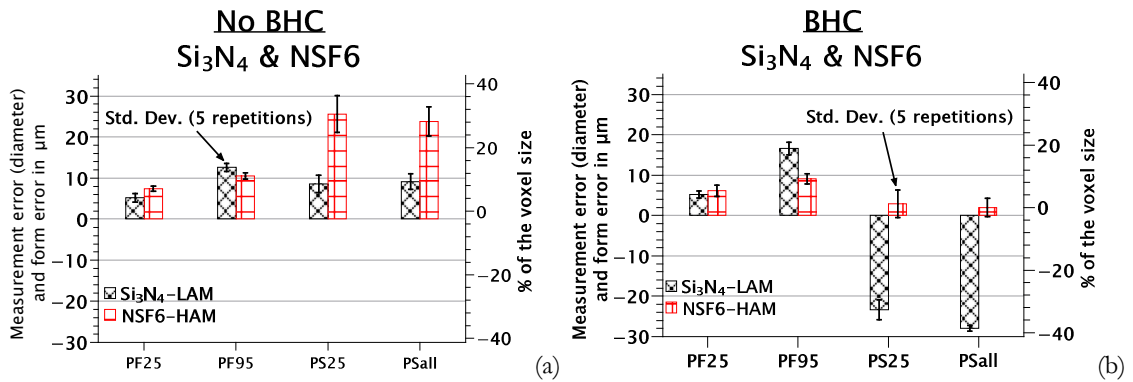


Fig. 4.4. Influence of the beam hardening correction on the P -test for size and form in the multi-material compound sphere made of Si₃N₄ & N-SF6: (a) data with no beam hardening correction and (b) data with beam hardening correction.

A significant decrease of the size measurement error was observed in the HAM (N-SF6) when applying the beam hardening correction. With no BHC the size measurement error was approximately 25 μm, while with the BHC, the measurement error in the HAM fell to below 5 μm. However, a negative impact — i.e. an overcorrection — on the size measurements in the Si₃N₄ (LAM) was observed when applying the BHC method. The measurement error before applying the BHC was approximately 9 μm, while with BHC, the error was around -24 μm.

The BHC seems to influence the form measurements of the LAM negatively as well. The absolute form error in the LAM was approximately 12 μm without BHC, while with BHC the form error increased to approximately 17 μm. No significant impact on the form measurement of the HAM was observed.

To verify these results, a statistical hypothesis test, similar to the test applied in $P1$, comparing the averages of 5 repeated measurements obtained with and without BHC was carried out. The results of the statistical test are shown in Fig. 4.5.

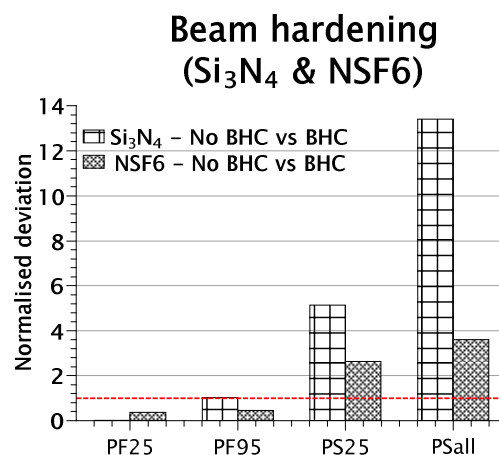


Fig. 4.5. Statistical test of the beam hardening influence in the MuMat P -test, evaluated in the MuMat compound sphere with low attenuation coefficient ratio (i.e. Si₃N₄ & N-SF6).

4.1. Results of multi-material sphere measurements (P-test)

The influence of beam hardening on the size measurements was statistically confirmed by the test, since the alternative hypothesis (of inequality of both averages) can be accepted for both LAM and HAM. It can be observed that normalised deviation of size using all data points (i.e. PSall) measured in the LAM is much larger than in the HAM. This may indicate that the negative impact of the BHC on the size measurement of the LAM outweighs the positive impact on the HAM in view of the results presented in Fig. 4.4.

For form measurements, the impact of the BHC on the measurements was not fully negligible for the LAM when using 95% of the data points (i.e. PF95), since the result of the normalised deviation was slightly above one.

As the conclusion of experiment *P2*, the results of size measurements in the HS made of HAM were significantly improved with the application of the BHC. However, a significant overcorrection of the size and a moderate increase of the form error of the HS made of the LAM were observed.

4.1.4 Results of experiment *P3*: Simulation of the more difficult multi-material combination for the *P*-test

The experiment *P3* is divided in two sections. The first part (a) focuses on the comparison between simulation and real CT data to evaluate whether the simulation delivers results in agreement with the real CT data. The second section (b) includes simulating multi-material scenarios with material combinations featuring lower attenuation coefficient ratios. The objective of this experiment is to verify whether the multi-material influence on the measurement monotonously increases. The results are presented below.

(a) Real data vs Simulation

A comparison between real CT scans and simulations based on the four metrological characteristics was carried out and the results are presented in Fig. 4.6.

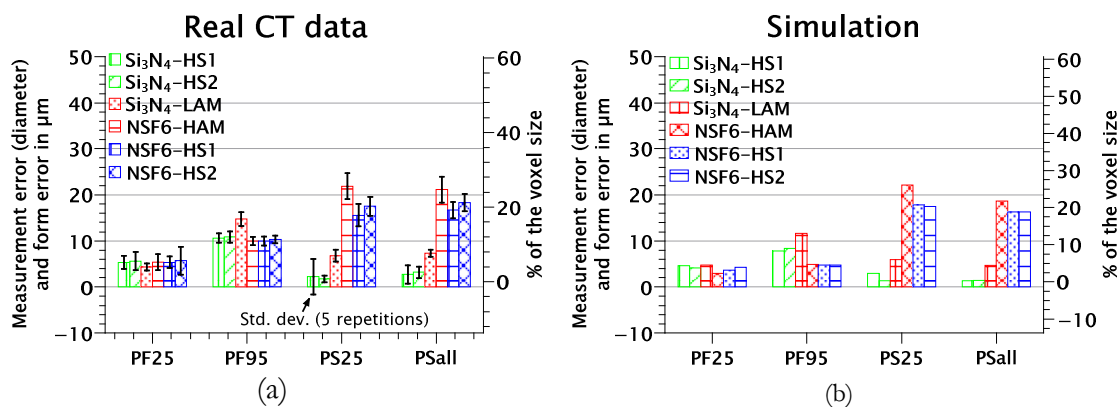


Fig. 4.6. Comparison between (a) real CT data and (b) simulation CT data for two MoMat compound spheres (i.e. made of Si_3N_4 & Si_3N_4 and N-SF6 & N-SF6) and one MuMat compound sphere made of Si_3N_4 & N-SF6.

In general, the results obtained with CT simulation were comparable to the results obtained with the real CT data, cf. Fig. 4.6-a and -b. Multi-material effects similar to those observed in the real scans were also found in the simulated data. However, a difference in the form measurements (PF95) was noticed. This difference can be explained by effects related to the detector e.g. afterglow, which were not considered in the simulation, leading to slightly better (i.e. lower) form errors. Regarding size measurements, there was a very good agreement between real data and simulation. The conclusion drawn from this experiment is that the simulation software is able to reproduce the MuMat effects observed in the real CT results.

(b) Simulation of more extreme multi-material cases

Simulations of more extreme multi-material cases (i.e. multi-material combinations with lower attenuation coefficient ratios) were carried out to verify whether the multi-material effects scale with the attenuation coefficient ratio. The results of four metrological characteristics for form and size with no beam hardening correction are presented in Fig. 4.7.

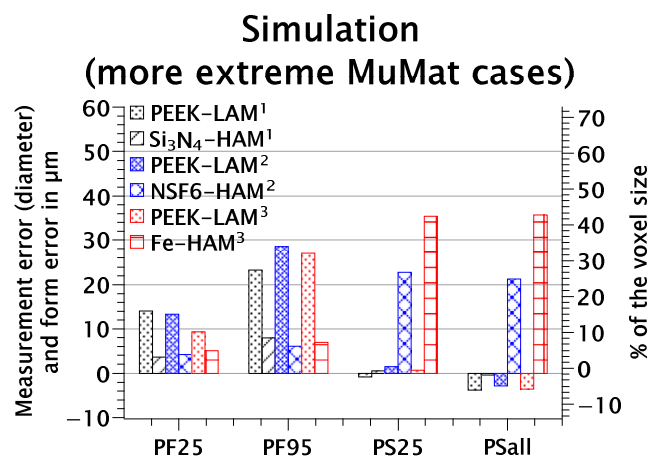


Fig. 4.7. Results of the simulation study including more extreme MuMat cases. Half sphere made of PEEK was paired with Fe, N-SF6 and Si₃N₄.

The size measurement error and absolute form error seem to increase monotonously with the decrease of the attenuation coefficient ratio. The compound sphere made of PEEK & Fe presented greater measurement error than the PEEK & N-SF6 and PEEK & Si₃N₄ spheres. A different error behaviour was observed in the form measurements. However, the HS made from LAM in the PEEK & N-SF6 sphere presented slight larger form errors than the HS made from LAM in the PEEK & Fe sphere. In contrast to this an increase of the form error in the LAM with the decrease of the attenuation coefficient ratio was to be expected. The causes of these results should be further studied.

4.2 Results of multi-material *E*-test measurements

Four experiments using the novel multi-material hole cubes were carried out. These experiments investigated different aspects of multi-material measurements and confirmed the influence of multi-material effects on length measurements with CT.

The data evaluation was based on the differences between CT and the reference measurements (calibration). Distances between holes based on centre-to-centre, bidirectional inner and outer measurements were measured. The results of the four experiments are presented in this section.

4.2.1 Results of the experiment *E0*: Multi-material influence on the length measurement error test

The evaluation of the multi-material length measurement error test was carried out in experiment *E0*. All three mono-material and three multi-material cubes were measured and analysed. The measurement error results of all cubes based on centre-to-centre measurements are presented in Fig. 4.8.

Due to the large number of lengths in each cube, a better and compact overview of the multi-material influence depending on the penetration length per material is achieved by the average, standard deviation and total range (i.e. minimum and maximum values) of the length measurement errors. In the plots, red rectangles, black thick bars and black thinner error bars represent the average, standard deviation and maximum/minimum range of all lengths measured in a height (i.e. groove), respectively. The blue error bars represent the worst-case test value uncertainty for each measurand, estimated as described in § 3.3.4.

Centre-to-centre distances

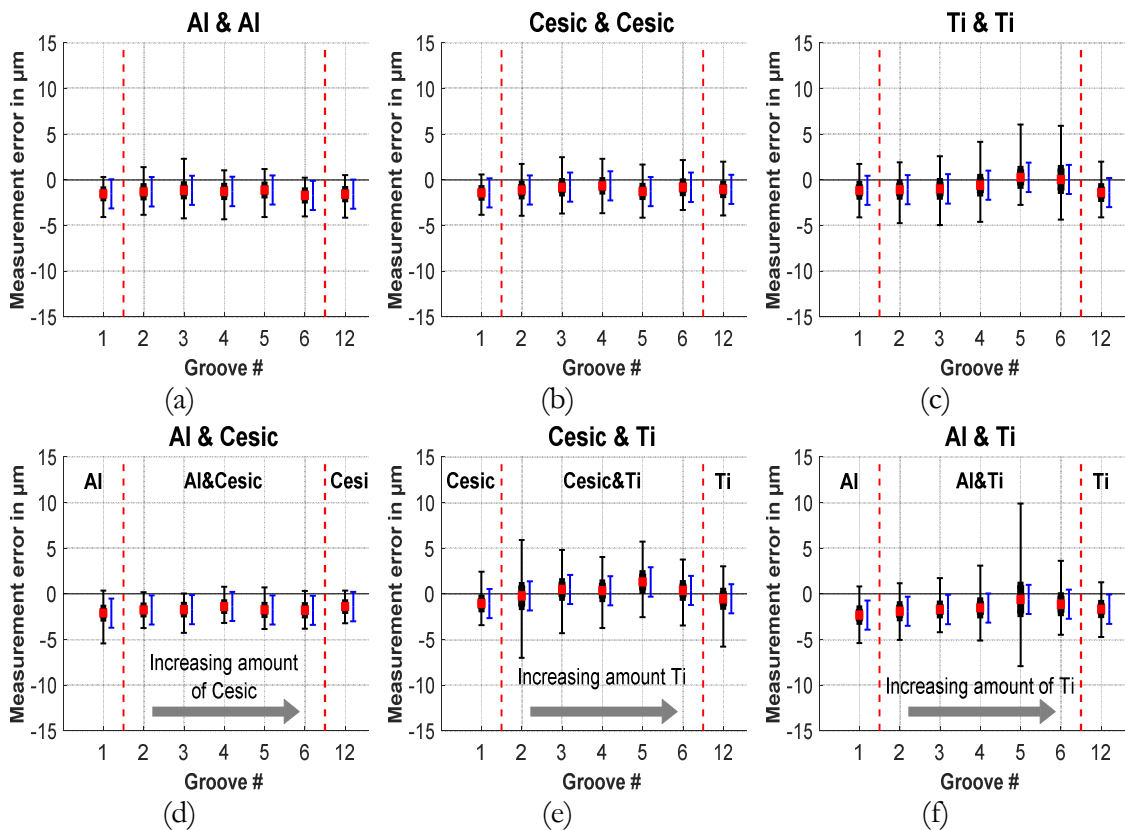


Fig. 4.8. Centre-to-centre length measurements of the hole cube reference standards: mono-material (a) Al & Al; (b) Cesium & Cesium; (c) Ti & Ti; and multi-material: (d) Al & Cesium; (e) Cesium & Ti and (f) Al & Ti.

Although the measurement errors for all cubes based on centre-to-centre lengths are below half of the voxel size (voxel size $\approx 30 \mu\text{m}$), a multi-material influence was still observed. An increase of the standard deviation and total range in the cubes with low attenuation ratios (i.e. Al & Ti and Cesium & Ti) was noticed, particularly in the grooves with a greater HAM content (i.e. Ti). The multi-material effect was confirmed by the mono-material cubes, where the results were all within $\pm 7 \mu\text{m}$, comparable to the results obtained with the cube with high attenuation ratio (i.e. Al & Cesium), while for the MuMat-HCs with low attenuation ratios the results were within $\pm 10 \mu\text{m}$.

As an example, a more detailed presentation of the length measurement errors showing the MuMat influence on local centre-to-centre measurements for the Al & Ti cube, is provided in Fig. 4.9. Here, the results of the measured distances at each groove are displayed in a colour plot. The x- and y-axes indicate the start and end point (hole) of each length, the colour scale represents the measurement error in μm . For example, the measurement error of the distance between holes H8-H14 at groove G5 was approximately $10 \mu\text{m}$, see G5 in Fig. 4.9.

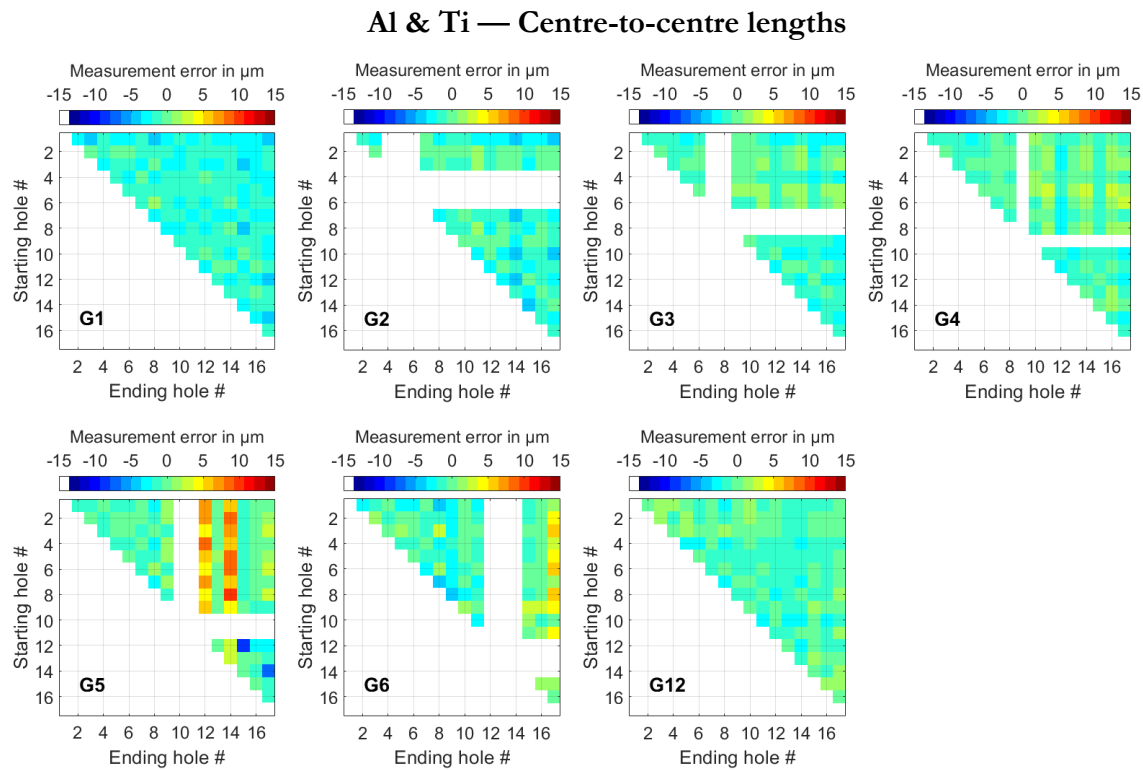


Fig. 4.9. Overview of all measured centre-to-centre distances of the Al & Ti hole cube standard. Colour scale represents the measurement error in μm , y- and x-axis represent the holes creating a distance, G refers to the groove number.

A strong influence at G5 (i.e. groove with 60% Ti and 40% Al) and holes 12 and 14 was observed. At this groove most of the affected (i.e. larger measurement error) distances were cases of inter-material measurement situations. A strong influence on in-material measurement situations was also observed. Particularly the distances between holes H12-H15 and H14-H17 resulted in the highest measurement errors. A noisier region, which impaired the surface determination, was observed in holes H12 and H14, especially in the vicinities of Ti, see Fig. 4.10-a. The noisy region is mainly caused by the brighter grey values in the reconstructed volume mainly in the vicinities of the Ti half, see Fig. 4.10-b. Current studies have shown that the detector burn-in effect might have a significant influence on the effect observed⁶. Other potential causes of this effect around Ti are: beam hardening effect [107] and detector unsharpness / resolution [108]. However, the exact cause for this effect is still unknown and further research needs to be carried out on this topic. These results indicate that the HAM impacts the measurements in general, in particular the measurements in the LAM when the material penetration length of the HAM is sufficiently large.

⁶ Personal discussion with Dr. Jens Illema, PTB, Braunschweig, Germany.

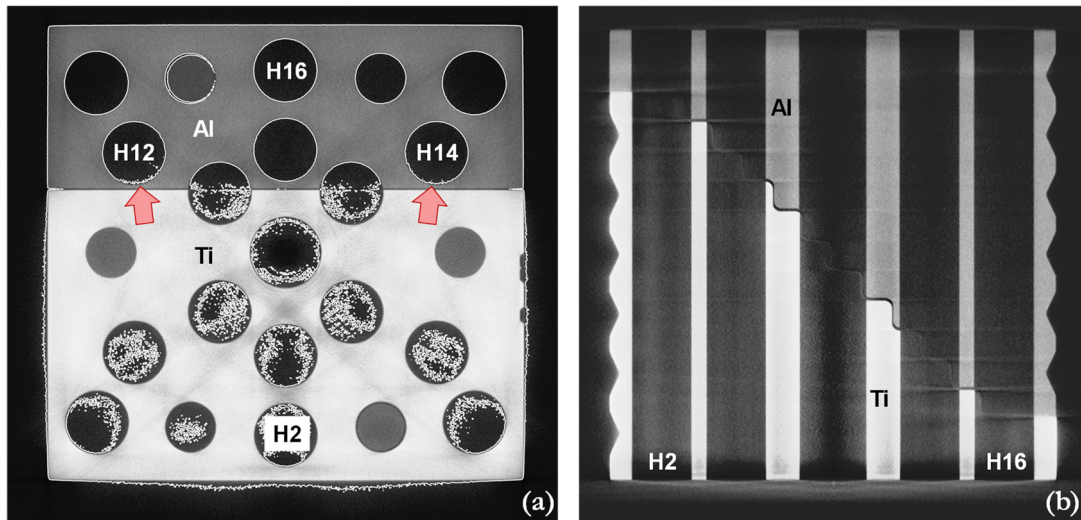


Fig. 4.10. (a) CT slice at G5 of a CT scan of the Al & Ti Cube. The white contour represents the determined surface, which in this example is optimised for the LAM (i.e. Al). Although the interface of holes H12 and H14 is only between Al and air, the determined surface in these holes is noisy, especially in the vicinities of Ti (pointed out by the red arrows); (b) CT slice of the Al & Ti cube along H2-H16 to highlight the difference in grey values in the holes in the Ti and Al areas.

White regions in the plots of Fig. 4.9 indicate that the distance — created by those respective holes — was not measured, either due to its symmetry (e.g. distance H1-H10 is equal to H10-H1) or due to the cube's design, where some holes are positioned in the interface of both halves, see Fig. 4.11. This kind of measurand was excluded from the analysis, since it characterises an atypical measurand and is too unstable to calibrate.

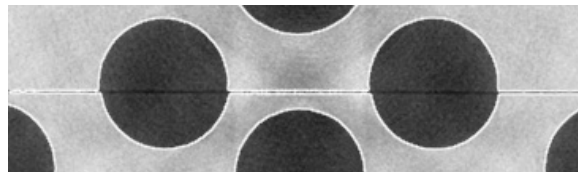


Fig. 4.11. Example holes positioned at the interface between the two half cubes.

The multi-material influence on the bidirectional measurements was also evaluated. The results of inner measurements, based on the patch operators as presented in Fig. 3.21, are shown in Fig. 4.12.

Bidirectional inner measurements

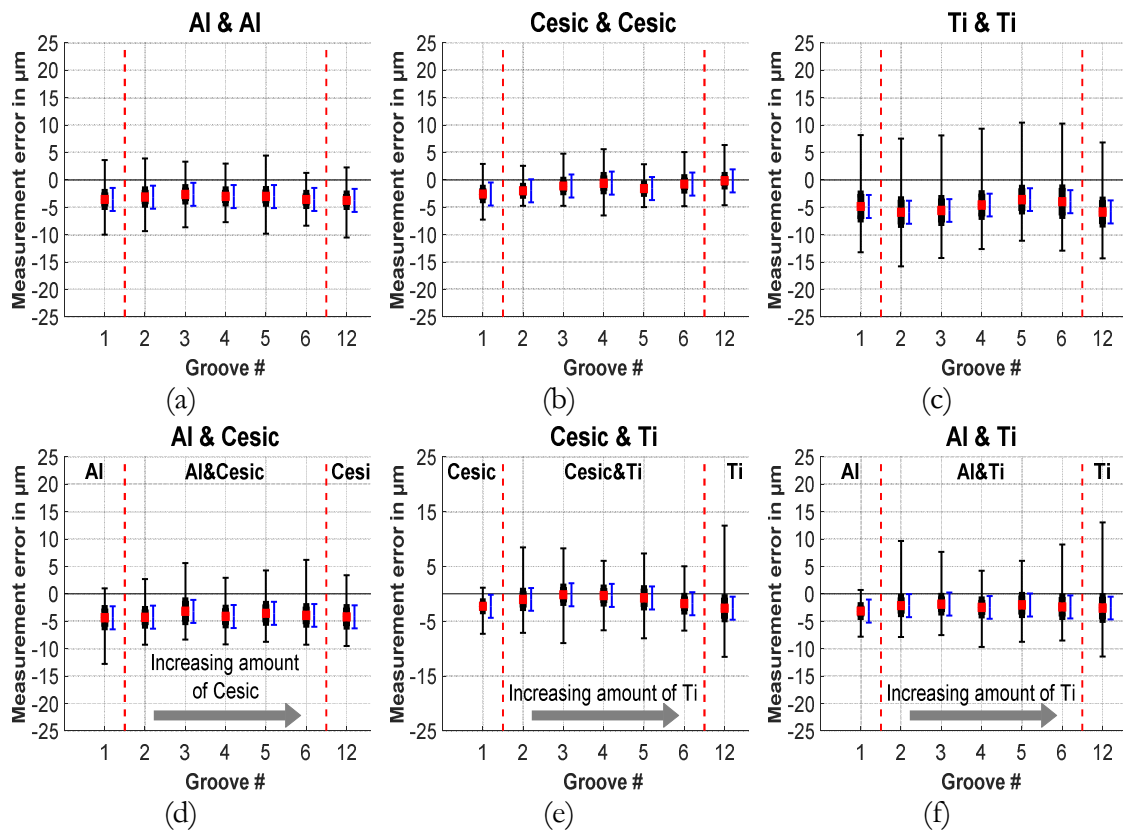


Fig. 4.12. Bidirectional inner length measurements of the hole cube reference standards: mono-material (a) Al & Al; (b) Cesium & Cesium; (c) Ti & Ti; and multi-material: (d) Al & Cesium; (e) Cesium & Ti and (f) Al & Ti.

Comparable measurement results were obtained with the MuMat and the MoMat cubes. Therefore, no substantial multi-material effect was observed in the bidirectional inner measurements.

Nevertheless, a significant multi-material influence on the bidirectional outer measurements was observed in the MuMat-HC made of Al & Ti. An increase of the measurement error range was observed in the grooves with longer Ti penetration lengths, see Fig. 4.13-f.

The colour plot used to present the centre-to-centre measurements (Fig. 4.9) was also used to plot all the bidirectional outer length results of the Al & Ti hole cube to highlight the largest measurement errors, see Fig. 4.14.

Bidirectional outer measurements

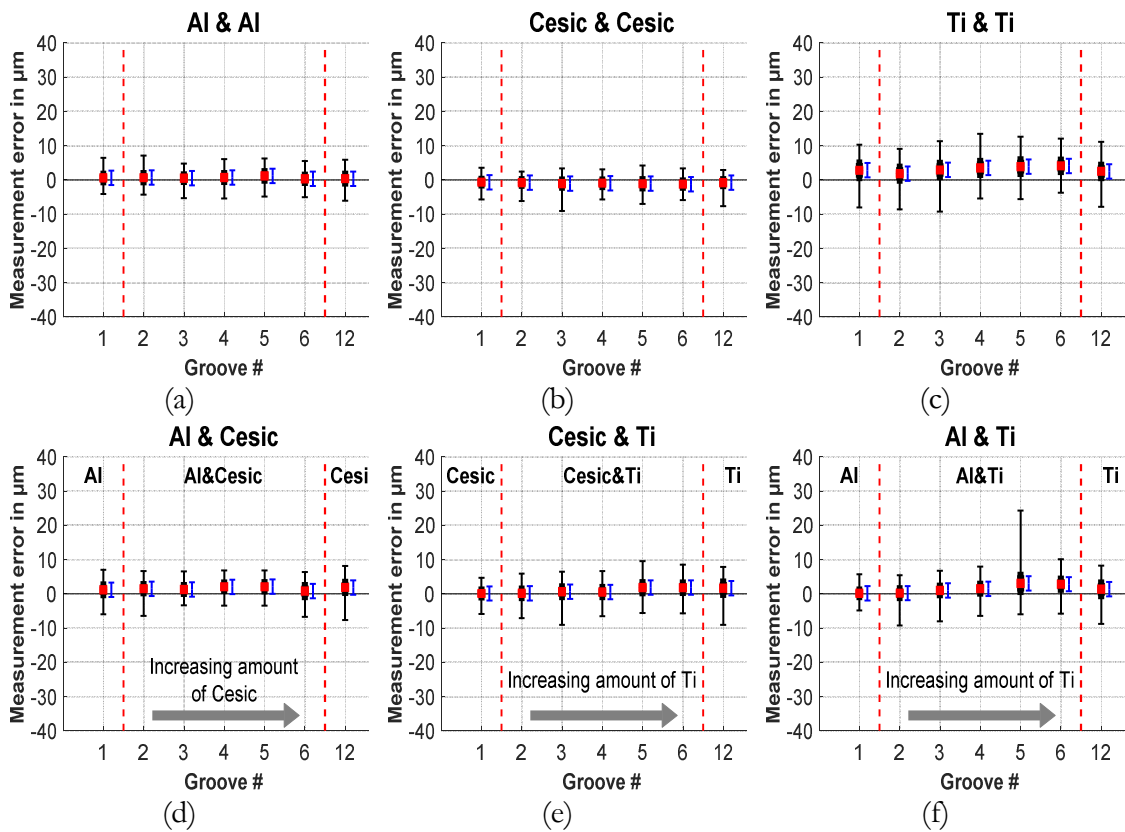


Fig. 4.13. Bidirectional outer length measurements of the hole cube reference standards: mono-material (a) Al & Al; (b) Cesium & Cesium; (c) Ti & Ti; and multi-material: (d) Al & Cesium; (e) Cesium & Ti and (f) Al & Ti.

Al & Ti – Bidirectional outer lengths

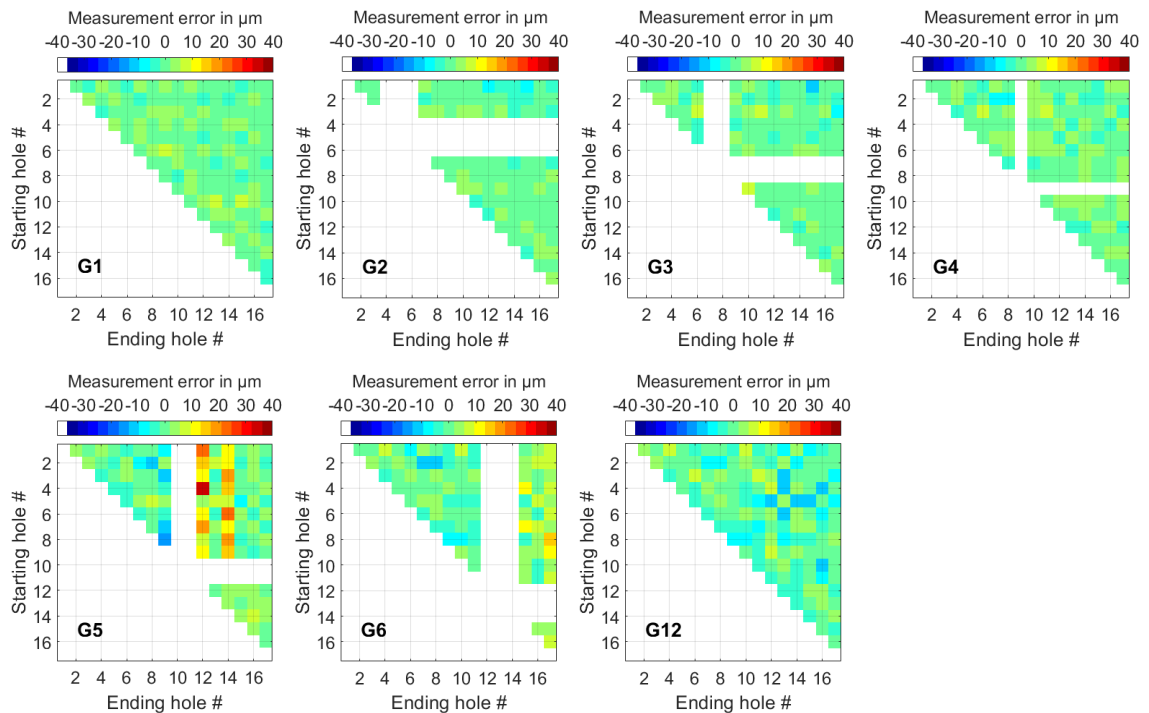


Fig. 4.14. Overview of all measured bidirectional outer distances of the Al & Ti hole cube standard. Colour scale represents the measurement error in μm , y- and x-axis represent the holes creating a distance, G refers to the groove number.

The results of the outer measurements showed a behaviour similar to the centre-to-centre measurement results. In the outer measurements, large measurement errors were observed in the distances involving holes #12 or #14.

Additionally, a statistical comparison — based on the Welch’s test — between the corresponding lengths of groove #1, an entirely mono-material situation groove, and groove “#n” within a cube was carried out. This statistical comparison served as a verification step for the hole cube standard design, by confirming statistical equivalence between groove #1 and the remaining grooves in the MoMat cubes, and statistical differences in a MuMat cube. Five repeated measurements of three cubes (i.e. Al & Al, Al & Ti and Ti & Ti) were carried out for the comparison. The normalised deviation was calculated according to Eq. (3.12) for every corresponding length and the results presented in box plots. The results of the centre-to-centre as well as bidirectional inner and outer measurements were compared and are shown in Fig. 4.15.

In the plots, the red lines represent the median of the data distribution and the blue bar represents the interquartile range (IQR) per groove. The upper and lower limits of the IQR were obtained from the 75th and 25th percentile of the sample, respectively. The black whiskers (error bars) were calculated from the 75th percentile plus $1.5 \times \text{IQR}$. This represents 99% of the sampled points, matching quite well with the common approach of $3 \times \sigma$ (i.e. 99.7%) for identification of outliers. It is considered an outlier if the value lies outside of the whisker range and is displayed, in the plots, as a red cross. Additionally, the width of the IQR bar represents the point density on that region, a thinner bar indicating a higher concentration of points [109].

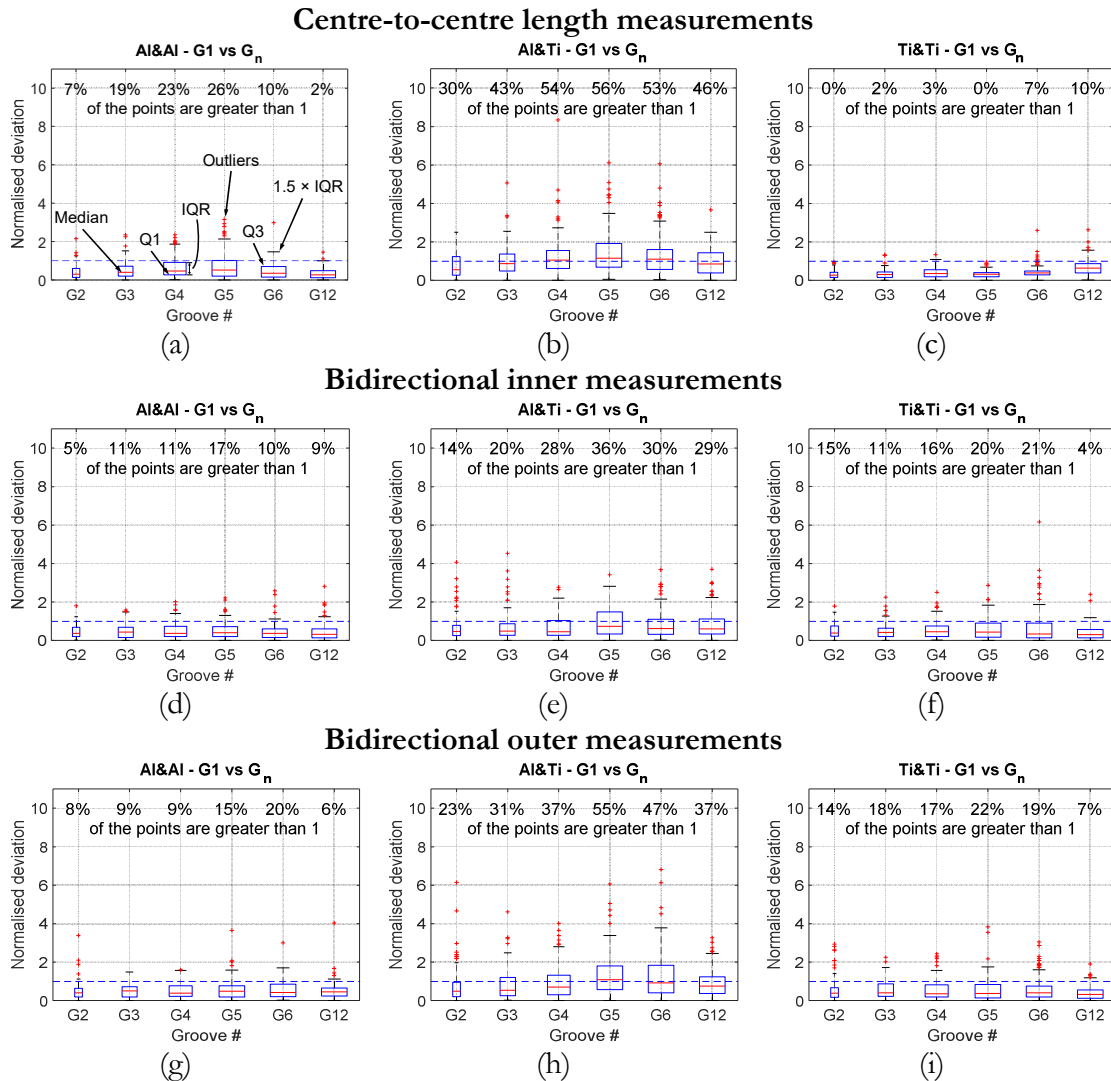


Fig. 4.15. Statistical comparison based on the Welch's test between groove one, a mono-material groove, with all the remaining grooves in a hole cube standard. The comparison was carried out for centre-to-centre, bidirectional inner and outer measurements in Al & Al (a, d, g); Al & Ti (b, e, h); and Ti & Ti (c, f, i) Ti & Ti, respectively.

Most of the results of the normalised deviation calculated in the mono-material cubes (i.e. made of Al or Ti) were below one for centre-to-centre, bidirectional inner and outer measurements. This indicates that most of the corresponding lengths, comparing two grooves G1 and G_n , are statistically equivalent with 95% reliability. The multi-material effects on the centre-to-centre and bidirectional outer length measurements were confirmed by the normalised deviation results obtained with the MuMat hole cube. Since most of the compared lengths were above one at grooves 4, 5 and 6, these results confirm that the hole cube standard design can depict multi-material effects and is indeed suitable for the multi-material acceptance test.

4.2.2 Results of experiment *E1*: Necessity of the multi-material length measurement error test

A statistical comparison between a MuMat cube (Al & Ti) and its respective MoMat cubes (i.e. Al & Al and Ti & Ti) was carried out to prove that multi-material effects — present in the MuMat cube — do not occur in the MoMat cube. The statistic used in experiment *E1* was the same as applied to experiment *E0* (i.e. based on the Welch’s test).

All corresponding lengths using centre-to-centre, bidirectional inner and outer measurands were compared. The results of the statistical comparison of the centre-to-centre measurements are presented in Fig. 4.16.

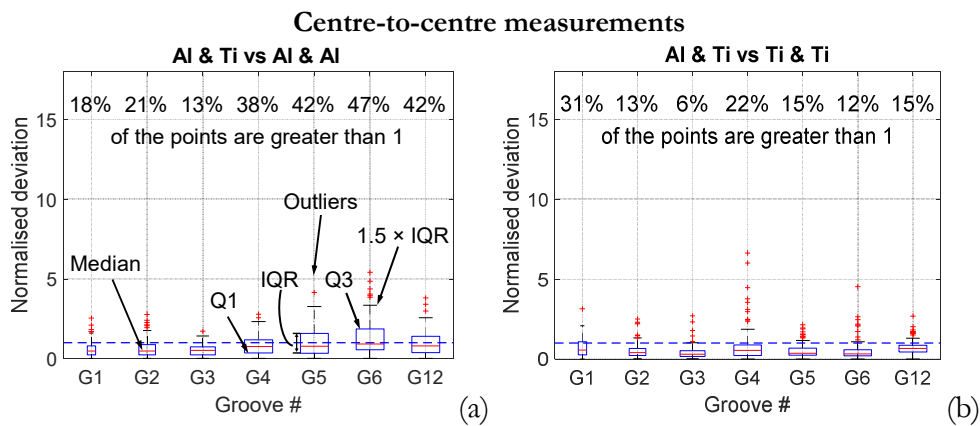


Fig. 4.16. Statistical comparison between the multi-material cube with both mono-material cubes: (a) Al & Ti versus Al & Al; and (b) Al & Ti versus Ti & Ti.

A significant difference between cubes Al & Ti and Al & Al can be observed. This confirms the presence of multi-material effects, particularly at the grooves with higher Ti content, see G5 and G6 in Fig. 4.16-a, as indicated by the increasing percentage of normalised deviations greater than one. In the comparison between Al & Ti and Ti & Ti, the multi-material was on average less visible. This can be explained by the high dispersion of results of the Ti & Ti cube, see Fig. 4.8-c.

Bidirectional inner and outer measurements were also evaluated using the same approach. The results of the statistical comparison are presented in Fig. 4.17 and Fig. 4.18.

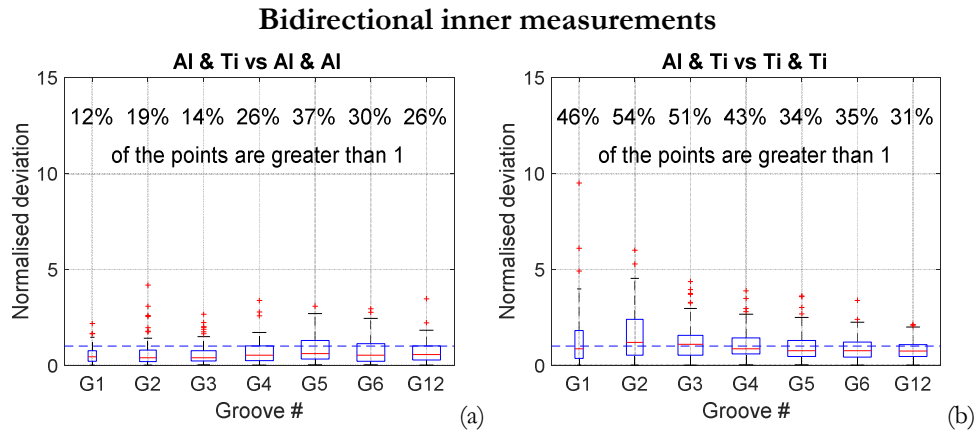


Fig. 4.17. Statistical comparison based on bidirectional inner measurements between a multi-material and two mono-material cubes: (a) Al & Ti versus Al & Al; and (b) Al & Ti versus Ti & Ti.

A minor multi-material effect was observed in the bidirectional inner measurements as well. It can also be seen in the comparison between Al & Ti and Al & Al, see Fig. 4.17-a. Although most of the normalised deviations were below one in all grooves, an increase of the percentage above one in the grooves with a higher Ti content was observed. This indicates a multi-material effect. However, an inverse error behaviour was observed in the Al & Ti versus Ti & Ti comparison, where a higher percentage of the normalised deviations above one was obtained in the grooves with a higher Al content (i.e. G2 and G3). This is probably no multi-material effect, since observations have shown that measurement errors originated from multi-material effects are mainly caused by a higher HAM content. This inverse behaviour is probably due to the large dispersion of results seen in the Ti & Ti cube.

The multi-material effect is more clearly visible in the statistical comparison based on the bidirectional outer measurement results, presented in Fig. 4.18.

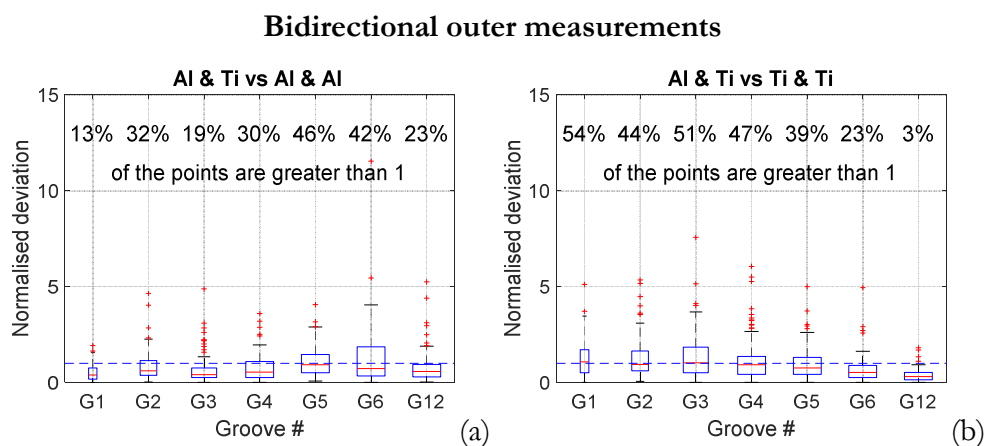


Fig. 4.18. Statistical comparison based on bidirectional outer measurements between a multi-material and two mono-material cubes: (a) Al & Ti versus Al & Al; and (b) Al & Ti versus Ti & Ti.

The higher the amount of Ti in grooves #5 and #6, the more lengths result in a statistical difference when comparing Al & Ti with Al & Al. The comparison between the

averages showed that almost half of all distances measured in grooves #5 and #6 were statistically different, for the Al & Ti versus Al & Al comparison.

On the other hand, the results of the statistical comparisons between Al & Ti and Ti & Ti showed no multi-material effects. The main reason for that is presumably the high dispersion of the results obtained with Ti & Ti cube, which can be explained by two effects. The first is the increased noise in the Ti & Ti measurements, probably caused by the high attenuation and large thickness of Ti. With this thickness (maximum thickness of approximately 35 mm), titanium absorbs the majority of the X-ray photons, decreasing the signal-to-noise-ratio (SNR) of the scan, and consequently increasing the dispersion of the measurement results. The degraded SNR can explain the high dispersion of points obtained with bidirectional measurements. The second potential source could originate from the imperfect manufacturing of the Ti & Ti cube. This would prevent an optimal assembly of Ti & Ti cube, where the half cubes are perfectly aligned with one another. Any misalignment, however, could degrade the tactile reference measurements, e.g. due to potential shaft probing or the measurements of ellipsoids instead of circles in the holes. To illustrate this, Fig. 4.19 shows a CT slice of the Ti & Ti cube assembly, where the misalignment between both halves are highlighted.

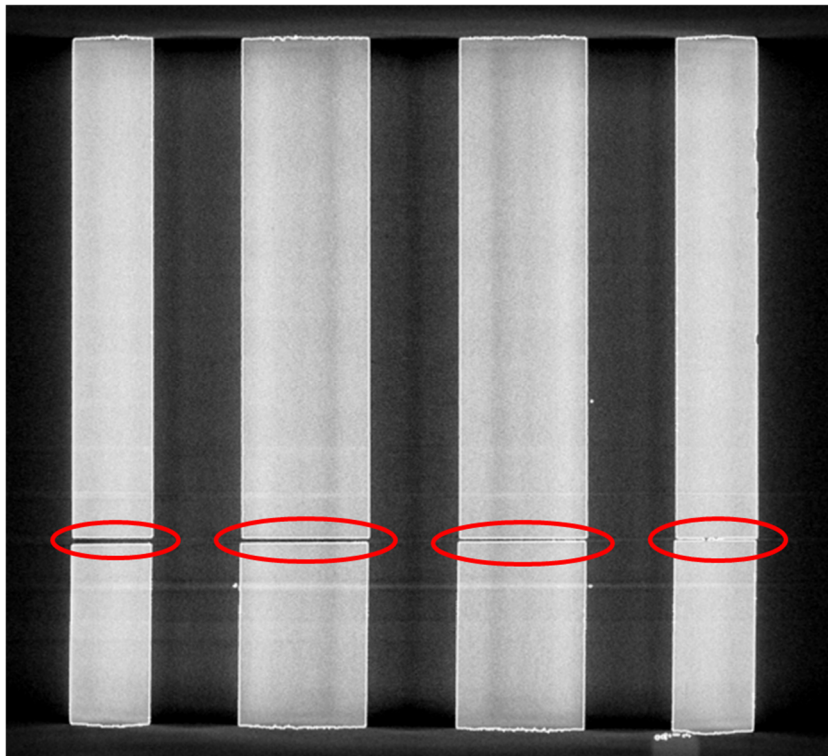


Fig. 4.19. Slice of a Ti & Ti scan to illustrate the misalignment between both half cubes.

4.2.3 Results of experiment E2: Sensibility verification of the test for the multi-material effects

The sensibility of the multi-material effect to the spectrum energy was tested in experiment E2. The cube with the lowest attenuation coefficient ratio (i.e. Al & Ti) was measured five times each using three different X-ray spectra. Centre-to-centre, bidirectional inner and outer measurements were carried out in all measurement lengths of the hole cube standard. The results of three energy spectra are presented in Fig. 4.20.

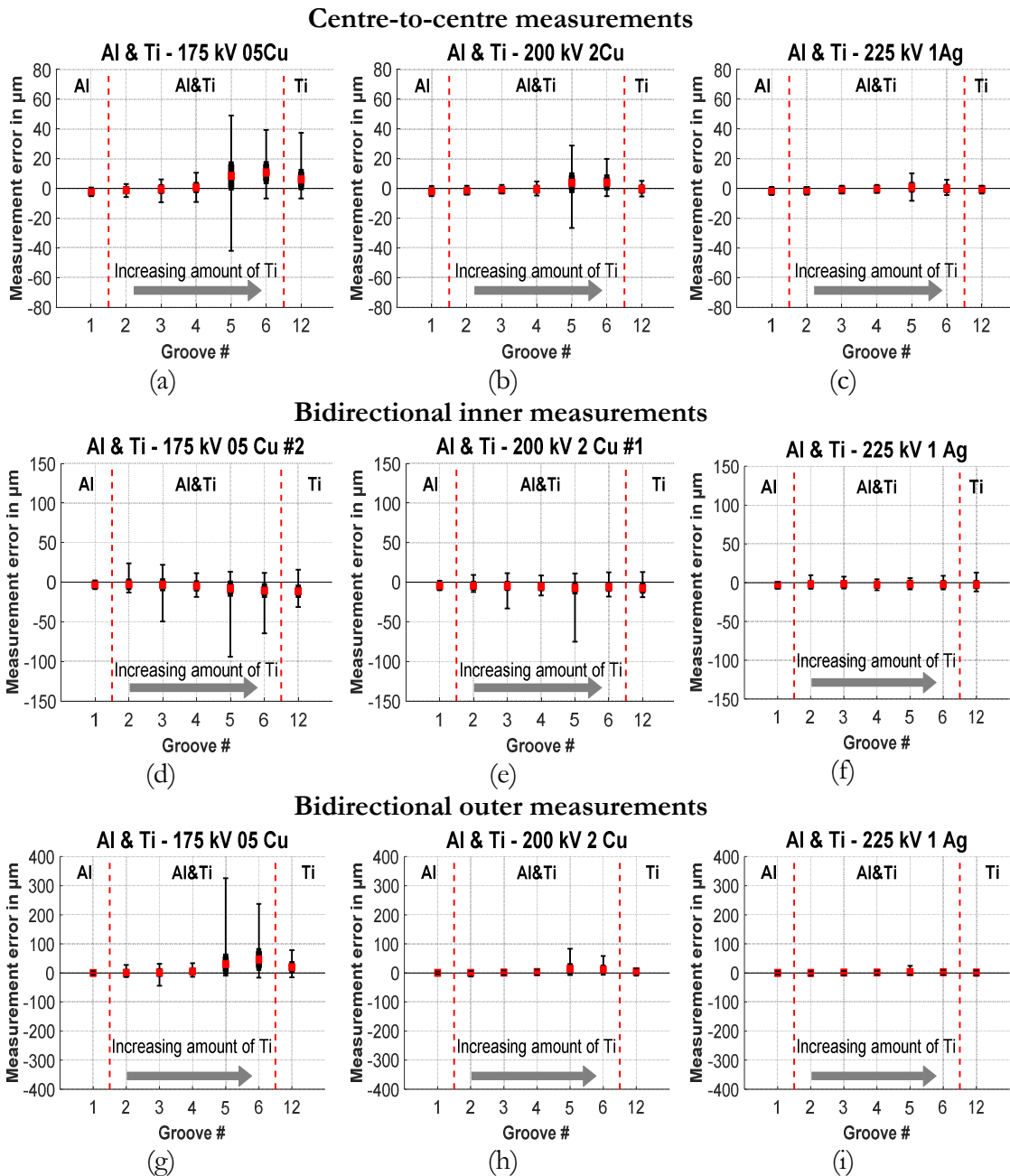


Fig. 4.20. Example centre-to-centre, bidirectional inner and outer length measurements in the Al & Ti cube standard using three different X-ray spectra with X-ray tube voltage and beam-filter of: centre-to-centre (a) 175 kV & 0.5 mm Cu; (b) 200 kV & 2 mm Cu and (c) 225 kV & 1 mm Ag; bidirectional inner measurements (a) 175 kV & 0.5 mm Cu; (b) 200 kV & 2 mm Cu and (c) 225 kV & 1 mm Ag; and bidirectional outer measurements (a) 175 kV & 0.5 mm Cu; (b) 200 kV & 2 mm Cu and (c) 225 kV & 1 mm Ag.

From the results, a strong dependence of the multi-material effects on the spectrum energy can be observed. For all measurand types, the measurement error increases with the decrease of the spectrum energy, and the measurement errors increase at grooves with a great content of Ti. This indicates that the multi-material effect strongly depends on the spectrum energy.

Similar to experiments *E1* and *E2*, a statistical hypothesis (Welch's) test was carried out to compare the measurement results of the Al & Ti cube measured with different X-ray spectra. The comparison was carried out for each measurand type, comparing the different spectra with each other. The results of these comparisons are shown in Fig. 4.21.

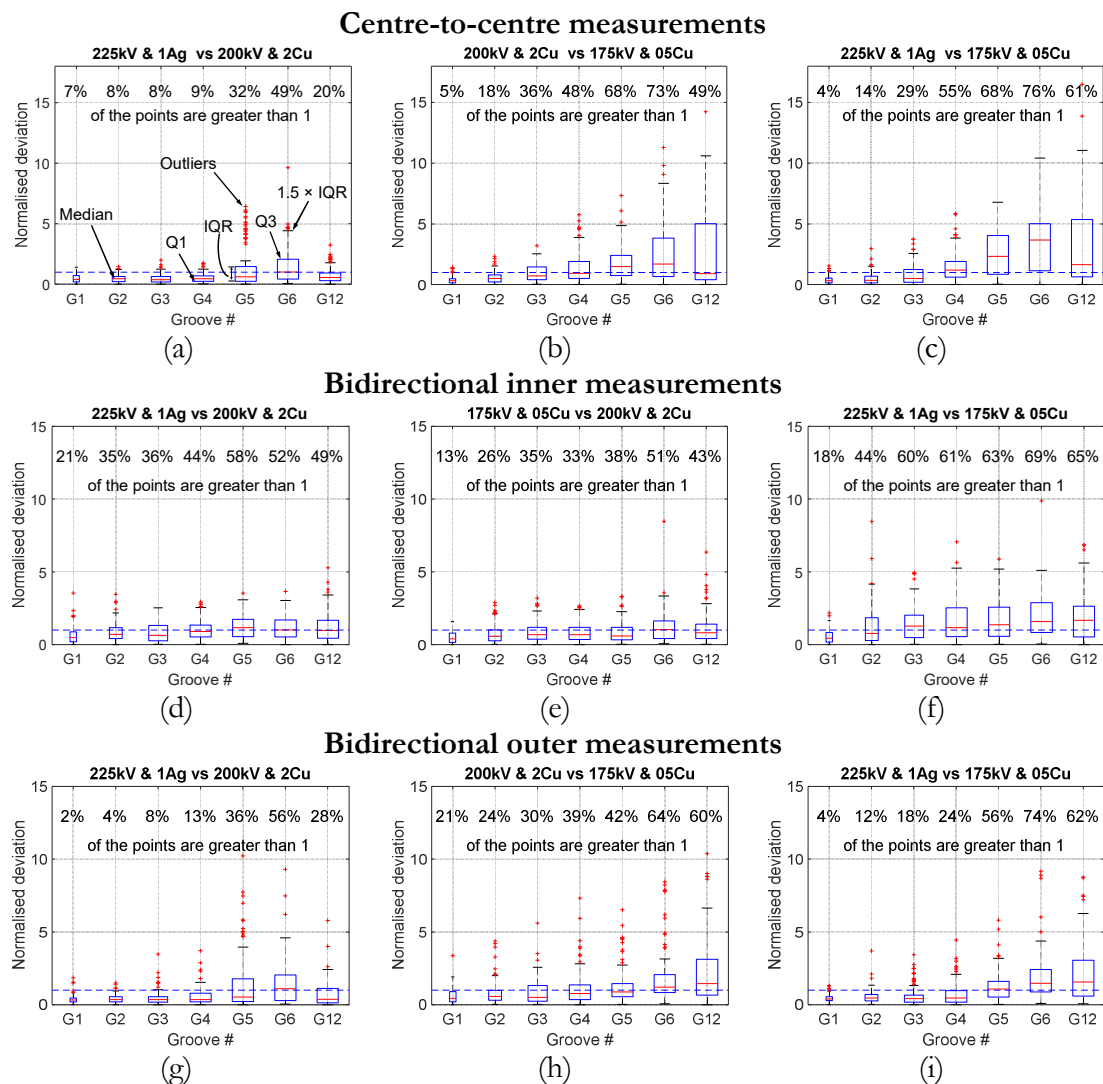


Fig. 4.21. Statistical comparison between three different X-ray spectra in a multi-material cube, comparison of centre-to-centre, bidirectional inner and outer measurements between (a), (d) and (g) 225 kV & 1 mm Ag versus 200 kV & 2 mm Cu, (b),(e) and (h) 200 kV & 2 mm Cu versus 175 kV & 0.5 mm Cu and (c) (f) and (i) 225 kV & 1 mm Ag versus 175 kV & 0.5 mm Cu.

The sensibility of the multi-material effects to the X-ray spectrum was clearly observed. The results showed a monotonous increase of the normalised deviation depending on both the difference of the spectrum energies and on the groove (i.e. amount of HAM). Grooves

with higher Ti content gave rise to higher percentages of normalised deviations greater than one. Similar results were observed in centre-to-centre, bidirectional inner and outer measurements.

4.2.4 Results of experiment *E3*: Simulation of the more difficult multi-material combination for the *E*-test

This experiment is based primarily on CT simulations and it is divided into two parts: simulation comparison with real data and simulation of more difficult multi-material combinations.

The first part was intended to verify the parametrisation of the simulation software and ensure it could reproduce the results obtained with the PTB's CT system. Thus, simulation-based measurements of two MoMat cubes (each made from Al & Al and Ti & Ti) and one MuMat cube (made of Al & Ti) were carried out re-using the scanning parameters of the real measurements. For comparison, the results obtained with simulation and real data of centre-to-centre measurements are shown in Fig. 4.22.

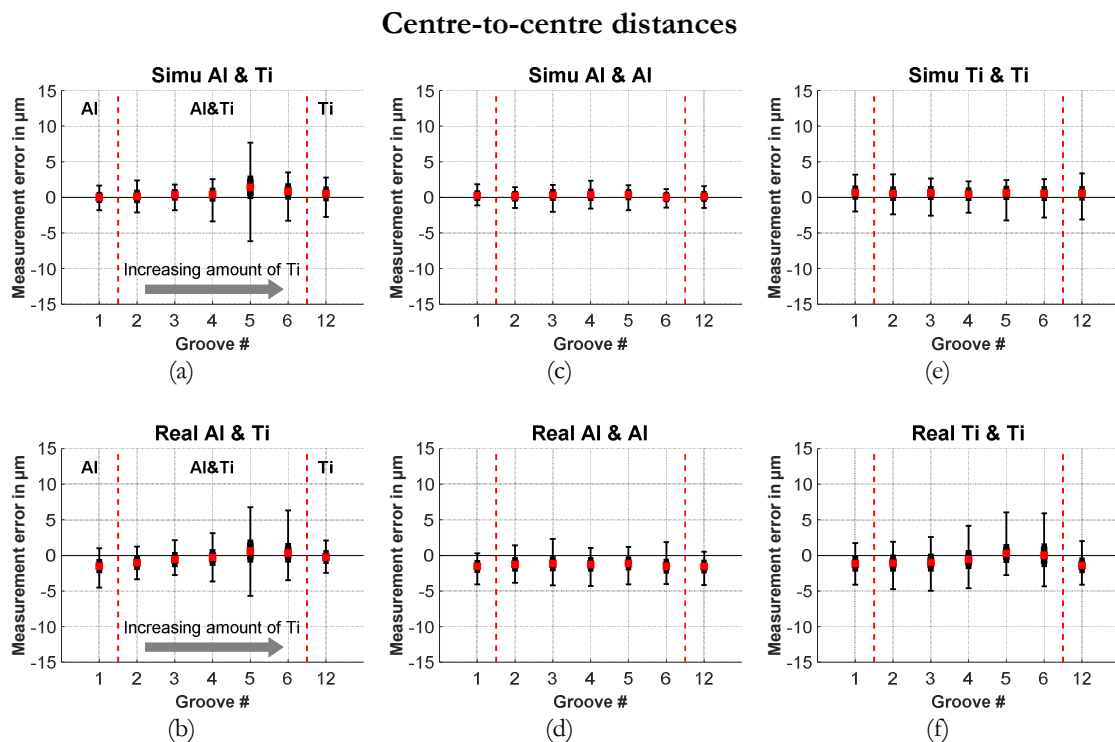


Fig. 4.22. Centre-to-centre length measurements error obtained by simulation and real data in the hole cubes: (a),(c) and (e) simulation data of the Al & Ti, Al & Al and Ti & Ti cubes, respectively; (b), (d) and (f) real data of the Al & Ti, Al & Al and Ti & Ti cubes, respectively.

In general, the results of the simulations were in good agreement with the real CT scans, indicating a satisfactory parametrisation of the simulation tool with the CT system tested in this thesis. Some small differences were observed, mainly due to the residual scaling errors

of the real scans, CT effects not yet implemented in the simulation (e.g. detector afterglow) and results with high dispersion as observed in the real CT scans of the Ti & Ti cube.

The second part (b) of experiment *E3* consisted of simulations of more difficult multi-material cases, where the attenuation coefficient ratio is decreased. The results of centre-to-centre, bidirectional inner and outer length measurements obtained using simulated data of the MuMat cubes made of Al & PEEK and Ti & PEEK are presented in Fig. 4.23.

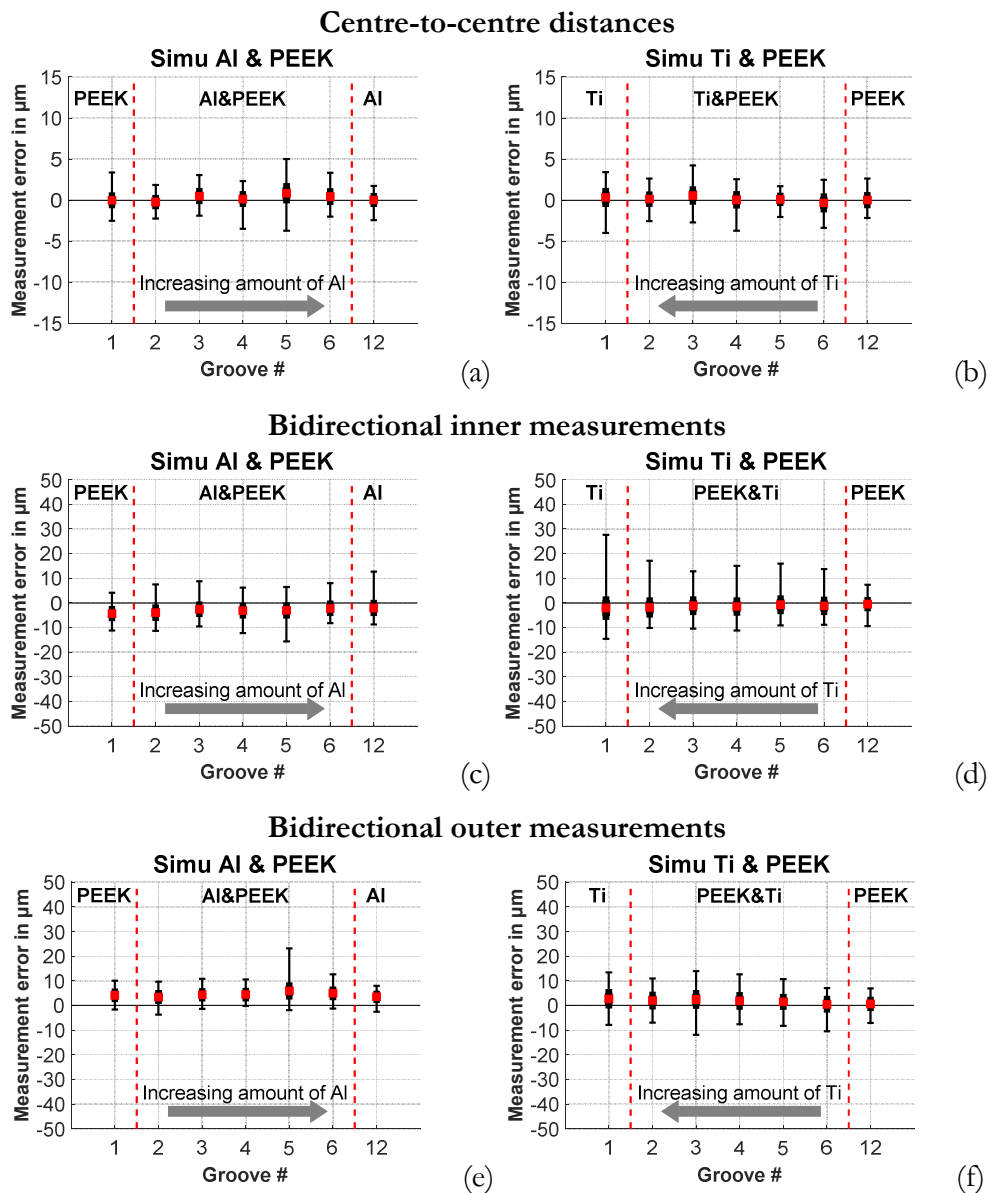


Fig. 4.23. Centre-to-centre, bidirectional inner and outer measurements obtained with simulation data of the hole cube standard made from (a), (c) and (e) Al & PEEK; and from (b), (d) and (f) Ti & PEEK.

In general, multi-material effects can be observed in the results obtained with simulation data. The measurement error of the centre-to-centre lengths for both material combinations were below $5 \mu\text{m}$ (i.e. below 15% of the voxel size). A slight increase of the max/min range in the centre-to-centre lengths was observed in the grooves with higher content of HAM, Al (in the cube Al & PEEK) and Ti (in the cube Ti & PEEK). Similar error behaviour was

observed in the bidirectional inner measurements, however the results obtained with the latter was below a voxel size (i.e. $30\ \mu\text{m}$). The multi-material effects were more clearly visible in the bidirectional outer measurements. An increased standard deviation of the measurement and max/min range was noticed in the Ti & PEEK cube when compared to the Al & PEEK cube. Also, a small increase of the measurement errors was noticed in both cubes in the grooves with a higher content of Al (in the Al & PEEK cube) and Ti (in the Ti & PEEK cube). However, a higher measurement error was expected in the cube with lower attenuation coefficient ratio (i.e. Ti & PEEK) at the grooves with higher Ti content, due to its attenuation coefficient ratio. The reason of this not fully understandable error behaviour should be further studied.

A simulation of a hole cube made from Fe & PEEK was carried out as well. However, no measurement could to be performed in the generated dataset. Severe problems were encountered when determining the surface of both materials, see Fig. 4.24. This problem probably arose from the very low attenuation coefficient ratio of the assembly.

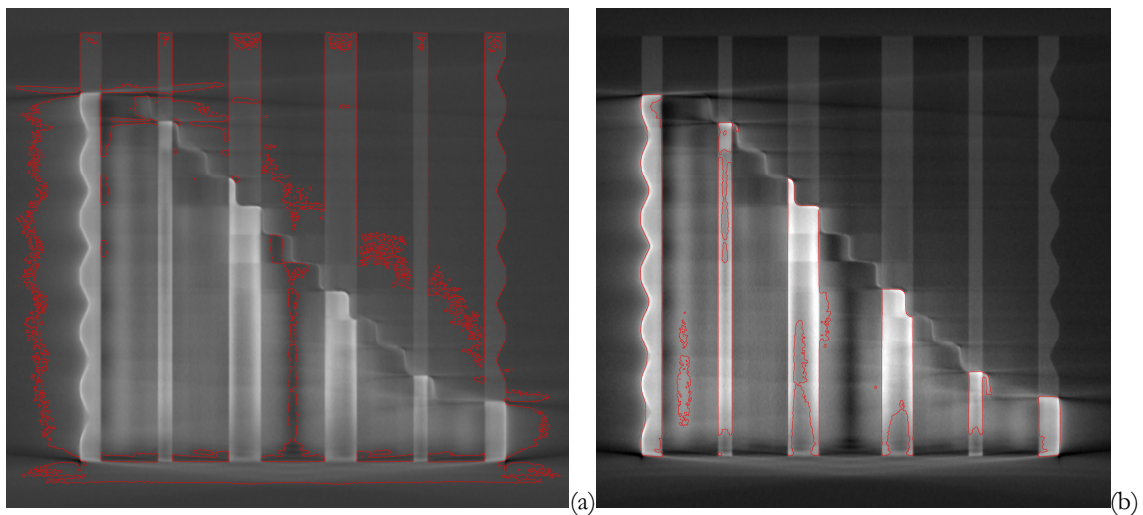


Fig. 4.24. Example slices of the Fe & PEEK hole cube simulation: (a) surface determination optimised for the LAM; and (b) surface determined based on the HAM (determined surface is represented by the red contour).

Although the results of the simulation confirmed the multi-material effects observed in real CT scans, a smaller measurement error than expected was found. Particularly in the simulations with lower attenuation coefficient ratios (e.g. Ti & PEEK). The reason for this difference is presumably an incomplete simulation of the factors affecting the response of the X-ray detector. Important effects not implemented in the simulation, e.g. the variation of the detector response curve depending on the incoming doses (see [110]) may be among the potential causes for these discrepancies. Nevertheless, further studies to achieve an even better agreement between simulation and real scans are necessary.

4.3 Summary of the chapter

The results of eight experiments using the novel multi-material reference standards proposed in this thesis were presented. The experimental investigations were carried out with the underlying objective to verify if the proposed test and reference standards met the MuMat test requirements. Additionally, several multi-material-related effects and their influence on dimensional and geometrical measurements were investigated in chapter 4.

Based on the test proposal and results obtained in the experimental investigations, it can be stated that all the test requirements were successfully met. The multi-material acceptance test proposed in this thesis was based on the ISO 10360 series of international standards. Test measurements for the probing error and length measurement error characteristics were carried out in a set of novel multi-material standards. Traceability of the test measurements was achieved by calibrating the reference standards using tactile coordinate measuring machines (CMM) and estimation of the respective test value uncertainties. The test value uncertainties associated with MuMat *P*- and *E*-tests were estimated inspired by the principles of the ISO 14253-5:2015 [88], ISO/TS 17865:2016-08 [89] and ISO/TS 23165:2006 [90] standard and technical specifications. The uncertainties were estimated taking into account all relevant factors influencing the test and they were found to be sufficiently small to allow statements related to multi-material effects. With these test uncertainty values, the test proposal has proven to be a suitable approach for verifying the performance of CT systems for multi-material measurements. To support this statement, the test value uncertainty values were compared with the standard deviation values obtained with the measurement repetitions. The uncertainty of the system appeared to be considerably greater than the uncertainty of the test, as the standard deviation of the measurements — which is only a part of the measurement uncertainty — is in the same range or greater than the test value uncertainties.

Furthermore, the utility of the MuMat acceptance testing was demonstrated using a statistical hypothesis test, comparing mono-material with multi-material measurements. The results showed that effects related to MuMat manifest a different error behaviour when compared to MoMat measurements. Furthermore, the influence of beam hardening on the size and form measurements was investigated by applying a beam hardening correction in the datasets. The results obtained with and without the beam hardening correction were compared. Based on the results, the use of a BHC has shown to have advantages and disadvantages. A significant improvement of the size measurement error of the HAM was observed when the BHC is applied. However, the measurements of form and size in the LAM was negatively impaired by the correction approach. The sensibility of the multi-

material effects on the spectrum energy was investigated using the multi-material hole cubes. In this experiment, the hole cube with the lowest attenuation coefficient ratio was measured with three different spectra. The results evidenced a multi-material influence on the length measurements depending on the spectrum energy. In general, the lower the spectrum energy the higher the measurement error and the multi-material effect.

Simulation-aided investigations were carried out using both the compound spheres and the hole cube standard designs. In both cases, the input parameters of the simulation software were confirmed by comparison between simulation with real data. In a second part of the simulation experiments, more difficult multi-material cases, including material combinations with lower attenuation coefficient ratios, were experimented. The results confirmed: the higher material attenuation coefficient difference the higher the multi-material effects and the higher the measurement errors.

Chapter 5: Conclusions, discussions and outlook

5.1 Summary and conclusions

The increasing number of multi-material workpieces and assemblies in industry have led to a likewise increased demand for the quality control of these complex parts. CT-based CMSs have shown to be an *enabler* technology for the quality control of multi-material workpieces, objects or components, even in their assembled state. An important shortcoming is the lack of standardised test procedures as well as suitable multi-material standards to verify the multi-material performance of CT-based CMS, which limits trust in the measurement results. Thus, industry, CT manufacturers and CT users share a growing interest in the development of a systematic way for testing CT-based CMSs for multi-material measurements.

To further develop trust in CT measurements, a novel multi-material acceptance test for CT was developed and characterised in this thesis. The proposed test follows the concepts of the ISO 10360 series of international standards. The development of this thesis was divided in three topics: definition of the test requirements, proposal of the novel multi-material test and verification of the test.

The test requirements defined the goals and demands to be met with the test proposal and served as starting point for the development of the test. The test proposal describes the concepts, materials and procedures to be used performing the test. The verification confirmed that the test proposal fulfils the defined test requirements.

For the conceptual phase of the test proposal, the evaluation of the local (probing error P test) and global (length measurement error E test) performance characteristics of CT-based CMSs were concepts adopted, as described in the ISO 10360 standard. Size, form and length were evaluated based on test measurements of calibrated standards. Accordingly, the test measurements should be carried out in conformance with specified rated operating conditions. However, the multi-material characteristics of CT-based CMSs are currently beyond the scope of standardisation and associated test procedures. Therefore, novel test concepts, multi-material standards and test procedures — considering the specifics of multi-material measurements — were developed in this thesis.

In the test proposal, multi-material measurement equipment, metrological characteristics, test procedures as well as the interpretation of the test results of multi-material P - and E -tests were described or adapted from existing standards. This work also

concentrated on the development of specification requirements with regard to take into consideration the multi-material nature of this test proposal. These requirements regulate (rated) conditions, which manufacturers should consider when specifying the multi-material performance of a CT-based CMS. For example, the system specification should contain information on material combinations (i.e. material attenuation coefficients) allowed to be used in the test. Another example of rated operating condition is related to the maximum material penetration length allowed in the test. This condition should consider material attenuation coefficients and X-ray spectrum used to perform the test.

In the verification phase, the proposed tests (P und E) were implemented, and respective reference standards were produced and calibrated. After that, the standards were used to verify the proposal by means of experimental investigations. As no suitable multi-material standards existed, novel multi-material sphere and hole cube designs were developed specifically for evaluating the multi-material P - and E -tests and presented in this work. The multi-material effects have been shown to depend greatly on the physical interactions between X-ray radiation and material. The material selection was mainly based on the X-ray attenuation, machinability/mechanical properties, applicability in industry and costs, aiming to present efficient solutions for the multi-material standards. In total, six materials — Si_3N_4 , Al_2O_3 and the lead-free optical glass N-SF6 for the P -, and Ti, Al and the special ceramic Cescic for E — were paired, creating multi-material combinations with both similar and fairly different attenuation coefficients. Mono-material standards using the same standard design were also created. They served as reference for the experimental study and to verify the multi-material effects as well as the design itself.

Several parameters related to multi-material effects were tested in the verification phase. The multi-material local and global performances of a CT-based CMS were tested to check if multi-material effects were visible in the test measurements, in light of the respective test value uncertainty. The test measurement results showed significant multi-material effects. The suitability of the test proposal to be used as a verification tool for the multi-material performance of CT-based CMSs was thus proven by the test results and the respective test value uncertainty. Additionally, the influence of a beam hardening correction method on the multi-material P -test measurements was investigated. The beam hardening correction (BHC) seems to have a positive impact on the HAM measurements. Conversely, it seems to have a negative impact on the P - measurements of the LAM, for the parameters used in this study. An increased noise and an overcorrection of the data leading to an increase of both form error and size measurement error were observed. Furthermore, the sensitivity of the multi-material effect to the energy spectrum was also tested by comparing length measurements

between scans with different spectrum energies. The results showed a strong multi-material influence in low energy measurements, which leads to additional measurement errors. Most of the experimental results were supported by statistical hypothesis tests, where the averages of multiple measurement results based on five repeated measurements were compared.

Experiments with extreme multi-material scenarios, including multi-material combinations with low attenuation coefficient ratios, were simulated. The results confirmed that the multi-material effect depends on the X-ray spectrum energy and attenuation coefficients of the materials. The validity of the simulation model was established by comparing results from real and simulated measurements made under similar conditions.

The main result of this thesis is the proposal for a novel multi-material acceptance test. In addition, new multi-material spheres and multi-material hole cube standards for the evaluation of the multi-material *P*- and *E*-tests were developed. Test concepts as well as multi-material standards were successfully tested based on experimental investigations and all test requirements were successfully met. Thus, the set of multi-material reference standards has shown great potential for evaluating the multi-material characteristics of CT-based CMSs, as they revealed multi-material-related effects on the measurements carried out with the PTB's CT system. The data evaluation workflow developed in this thesis allows comparability between CT and other CMSs.

Based on the test proposal and results, it can be concluded that all objectives defined in this thesis were reached and the questions raised in Chapter 1: can thus be answered:

- i. Are there relevant multi-material effects influencing dimensional and geometrical measurements by CT?

Answer: Yes. The multi-material influence was observed in both *P*- (for form error and size) and *E*-test (for centre-to-centre and bidirectional) measurements. The multi-material effects on the test measurements were supported by analysing the test value uncertainty and using statistical tools.

- ii. Are there (existing) systematic approaches for the performance evaluation of CT-based CMS for multi-material measurements?

Answer: No work has been found in the literature describing a method to verify the performance of CT-based CMSs based on the acceptance testing concepts for multi-material measurements. Only limited research on the influence of effects related multi-material on the measurements by CT exists. Some studies on the influence of correction methods specialised for multi-material-related effects were found in the literature but were also limited in number.

- iii. Should standardisation bodies consider the multi-material induced effects in the further development of standards for CT-based CMS?

Answer: Yes. The reasons are: (1) The results presented in this thesis showed significant effects present only in multi-material measurements. (2) CT manufacturers and users share a growing interest in an acceptance test for multi-material measurements. Therefore, the responsible standardisation committees should be encouraged to further develop a multi-material test, with the aim of reaching at an internationally agreed method to evaluate the performance of CT-based CMSs considering multi-material effects.

- iv. Is the proposed test suitable for evaluating the performance verification of CT-based CMSs for multi-material measurements?

Answer: Yes. Based on the estimated test value uncertainty of multi-material *P*- and *E*-tests and statistical tests carried out, it was demonstrated that multi-material effects were observed in the test measurements. Furthermore, the expanded test value uncertainty was significantly smaller than the typical measurement deviations (e.g. repeatability) of the CT system. This indicates the suitability of the proposed test for performance verification of the CT-based CMSs for multi-material measurements.

5.2 Discussions and outlook

The proposed multi-material acceptance test presented in this thesis expanded the knowledge regarding multi-material CT measurements. Apart from this, it takes an important first step towards the evaluation of CT systems for the quality control of industrial multi-material parts. However, on the path towards reliable multi-material measurements with CT, several questions and opportunities for improvements still remain open. Considering the work carried out during this thesis, topics of further development related to this proposal and performance verification of CT systems related to multi-material measurements are presented following.

5.2.1 Improvements related to the multi-material standards

Throughout the development of this thesis, several difficulties related to the development and implementation of the multi-material standards were encountered.

Although the hole cube design proved to be suitable for evaluating the multi-material performance of CT-based CMSs, a shift of one half of the hole cube relative to the other was observed. This relative displacement occurred presumably during transport and

necessitated re-calibration of the standard. Therefore, to better protect the hole cube standards from undesired shifts during transport and to maintain the standard's cleanliness, the development and manufacturing of a dedicated suitcase is recommended.

In addition, the manufacture of the Ti & Ti hole cube encountered problems. The imperfect manufacturing prevented the optimal assembly of the cube, and thus degraded the tactile and CT measurements to some extent. To further improve the experimental results of this thesis, by decreasing the measurement error of the Ti & Ti cube and highlighting even more the multi-material effects, the Ti & Ti cube should be re-calibrated to account for the misalignments, or a new one could be manufactured.

The uncertainty of the calibration is an important contributor for the test value uncertainty, thus it should be sufficiently low to further evidence multi-material effects in the test measurements. One potential approach to reduce the uncertainty of the calibration would be to minimise systematic errors of the tactile CMM, e.g. by measuring the cubes in different orientations.

5.2.2 Potential improvements related to the multi-material test proposal

This thesis has laid the groundwork for performance verification of multi-material CT measurements, but only for a limited range of multi-material combinations. To better understand multi-material effects, in different more extreme material combinations, real-data-based studies could be performed, investigating multi-material cases not yet considered e.g. plastics and more dense metals.

In future work it should also be more thoroughly verified whether the system specification related to the multi-material performance is valid throughout the entire measurement volume, as material penetration lengths vary at different angles of the X-ray beam.

5.2.3 Potential improvements related to multi-material effects

Correlation studies of observed effects and potential causes could also further expand the understanding of multi-material measurements. Correlations between, for example, material penetration lengths, beam-hardening, scattering effects and the measurement error is suggested to be further studied, perhaps assisted by simulation tools. A sufficiently good characterisation of the CT-based CMS to be modelled in the simulation environment is however required.

To a large extent, the response of the detector for multi-material measurements is not understood. The quantitative effects of the dependency of the detector response curve on

the incoming X-ray spectrum on dimensional measurements is another potential topic for future investigations.

5.2.4 Future standardisation developments

The ISO standard for mono-material CT measurements is on its way to be published. Some aspects of the standard are currently under intense discussion such as the use of representative points measured in a small area on the test sphere (patch-based point) for the evaluation of the P -test and the evaluation of the test value uncertainty. Thus, further developments of the multi-material test proposal should follow and adopt future developments of the ISO standards, where feasible.

5.2.5 Future technological developments

New technological developments that may affect the multi-material performance of CT systems should be considered and tested. An example of a recent technological development is the surface determination method of a commonly used CT evaluation software (i.e. VG Studio MAX 3.3). The latest version of this software features a newly developed surface determination method for multi-material datasets — which came out at the very end of this thesis and was therefore not analysed. As future work, it is recommended to test this new surface determination method on the multi-material standards to evaluate its performance as well as limitations.

List of figures

Fig. 2.1. Typical workflow of a CT measurement (source: [11]).	6
Fig. 2.2. Cone-beam CT system geometry with flat panel detector.	7
Fig. 2.3. Creation of X-rays, types of physical interactions between electrons and target atoms and their contribution for the X-ray spectrum.	9
Fig. 2.4. Attenuation coefficient versus photon energy for Al and Fe	10
Fig. 2.5. Signal workflow in a detection element of a detector.	12
Fig. 2.6. Reconstruction example based on the FBP reconstruction algorithm.	13
Fig. 2.7. Example workflow of a local gradient-based surface determination method.	15
Fig. 2.8. Examples of data analysis with CT.	17
Fig. 2.9. Relevant influencing quantities of CT dimensional measurements.	19
Fig. 2.10. X-ray spectra created with different anode materials.	20
Fig. 2.11. Causes of X-ray absorption by the workpiece materials.	21
Fig. 2.12. Problem of the surface determination in a multi-material assembly.	24
Fig. 2.13. Example of the search distance influence on the surface determination.	25
Fig. 2.14. Illustration of the origin of beam hardening effect.	26
Fig. 2.15. Beam hardening effect in a multi-material scenario	26
Fig. 2.16. Cupping artefact caused by beam hardening effect.	27
Fig. 2.17. Scattering radiation from the object.	28
Fig. 2.18. Scattered radiation in multi-material measurements.	29
Fig. 2.19. Photon starvation effect.	29
Fig. 2.20. Photon starvation in multi-material measurements.	30
Fig. 2.21. Dependency of the detector absorption depth on multi-material workpiece.	31
Fig. 2.22. Probing error test with a test sphere.	37
Fig. 2.23. Examples of length standards suitable for CT.	38
Fig. 2.24. Length measurement error.	39
Fig. 3.1. Workflow of the creation of the multi-material acceptance testing.	45
Fig. 3.2. Multi- and mono-material measurement situations.	51
Fig. 3.3. Specification example of maximum material thickness.	54
Fig. 3.4. Suggested pattern of the 25 patch-based representative points for the <i>P</i> -test.	60
Fig. 3.5. Illustration of conformity and nonconformity zones.	61
Fig. 3.6. Design of the multi-material test sphere used for the proposed <i>P</i> -test.	70

Fig. 3.7. Set of multi- and mono-material compound spheres.	72
Fig. 3.8. Attenuation curves of the materials selected for the multi-material <i>P</i> -test.....	73
Fig. 3.9. Calibration area of the multi-material spheres.	74
Fig. 3.10. Unwanted cutting- or mounting-related scenarios.....	75
Fig. 3.11. Problem of the standard threshold value for the multi-material sphere.....	76
Fig. 3.12. Workflow of the multi-material <i>P</i> -test data analysis.	77
Fig. 3.13. Creation of the representative points based on patches.	78
Fig. 3.14. Evolution of the multi-material length reference standard.....	79
Fig. 3.15. Multi-material hole cube (MuMat-HC) design.	80
Fig. 3.16. Hole cube standards.	84
Fig. 3.17. Attenuation curves of the materials selected for the multi-material <i>E</i> -test.....	84
Fig. 3.18. Calibration strategy of the hole cube standards.....	85
Fig. 3.19. Workflow of the CT measurement of the MuMat-HCs.	86
Fig. 3.20. Alignment procedure of the MuMat-HC	87
Fig. 3.21. Creation of the patch-based representative points for the uni- and bidirectional length measurements.	88
Fig. 3.22. PTB's Nikon Metrology MCT 225 system used for the experiments.....	89
Fig. 3.23. Schematic of experiment <i>P1</i>	94
Fig. 3.24. Comparison scheme of experiment <i>E2</i>	100
Fig. 4.1. Results of the <i>P</i> -test measurements (experiment <i>P1</i>).....	104
Fig. 4.2. Results of experiment <i>P2</i> measurements.	105
Fig. 4.3. Statistical Welch's test of the experiment <i>P2</i>	106
Fig. 4.4. Results of the influence of the beam hardening correction on the <i>P</i> -test.	107
Fig. 4.5. Statistical test of the beam hardening influence in the MuMat <i>P</i> -test.	107
Fig. 4.6. Comparison between real CT data and simulation CT data.	108
Fig. 4.7. Results of the simulation study including more extreme MuMat cases.	109
Fig. 4.8. Centre-to-centre length measurements of the hole cube reference standards.....	111
Fig. 4.9. Colour plot overview of all measured centre-to-centre distances of the Al & Ti hole cube standard.	112
Fig. 4.10. Brighter grey values in the vicinity of the Ti half.	113
Fig. 4.11. Example holes positioned at the interface between the two half cubes.	113
Fig. 4.12. Bidirectional inner length measurements of the hole cube standards.....	114
Fig. 4.13. Bidirectional outer length measurements of the hole cube standards.....	115
Fig. 4.14. Colour plot overview of all measured bidirectional outer distances of the Al & Ti hole cube standard.	115
Fig. 4.15. Statistical test between groove one with all the remaining grooves in the Al & Ti hole cube standard.	117

Fig. 4.16. Statistical comparison based on centre-to-centre measurements between the multi-material cube and two mono-material cubes.	118
Fig. 4.17. Statistical comparison based on bidirectional inner measurements between a multi-material and two mono-material cubes.	119
Fig. 4.18. Statistical comparison based on bidirectional outer measurements between a multi-material and two mono-material cubes.	119
Fig. 4.19. Slice of a Ti & Ti scan to illustrate the misalignment between both halves.	120
Fig. 4.20. Results of the measurements using three different X-ray spectra.	121
Fig. 4.21. Statistical comparison between three different X-ray spectra.	122
Fig. 4.22. Length measurements error obtained by simulation and real data.	123
Fig. 4.23. Centre-to-centre, bidirectional inner and outer measurements obtained with simulation data of the hole cube standard made from PEEK, Al and Ti.	124
Fig. 4.24. Example slices of the Fe & PEEK hole cube simulation.	125

List of tables

Table 2.1. Detected effects/errors by different length measurement methods: bi-, unidirectional and centre-to-centre.....	39
Table 2.2. Overview of the relevant influencing factors and their effects to multi-material measurements.....	43
Table 3.1. Classification of the attenuation coefficient scenarios.....	50
Table 3.2. Decision matrix for the selection of the materials for the MuMat <i>P</i> -test.....	72
Table 3.3. Material pairings used for the multi-material <i>P</i> -test realisation with their X-ray attenuation coefficient ratio and classification of the attenuation coefficient scenarios.....	73
Table 3.4. Decision matrix for the selection of the materials for the MuMat <i>E</i> -test.....	82
Table 3.5 Materials for the multi- and mono-material <i>E</i> -test and their measured attenuation coefficient ratios and classification of the attenuation coefficient scenarios.....	83
Table 3.6. Overview of the experiments carried out in this thesis.....	89
Table 3.7. CT scanning parameters used for each mounted MuMat and MoMat sphere. ...	91
Table 3.8. Test value uncertainty contributions considered in the multi-material <i>P</i> -test.....	93
Table 3.9. CT scanning parameters used for the hole cube standards in experiment <i>E0</i>	97
Table 3.10. Test value uncertainty estimation of the length measurements.....	99
Table 3.11. CT scanning parameters used for the hole cube Al & Ti measured with different X-ray spectra in experiment <i>E2</i>	100

References

- [1] W.K. Röntgen, On A New Kind of Rays, *CA: A Cancer Journal for Clinicians*. 22 (1972) 153–157. <https://doi.org/10.3322/canjclin.22.3.153>.
- [2] J. Radon, Über die Bestimmung von Funktionen durch ihre Integralwerte längs gewisser Mannigfaltigkeiten, in: *Berichte über die Verhandlungen der Königlich Sächsischen Gesellschaft der Wissenschaften zu Leipzig. Mathematisch-Physische Klasse*, B. G. Teubner, Leipzig, 1917: pp. 262–277.
- [3] A. Habermehl, H.-W. Ridder, Method and apparatus for testing material such as disease in living trees, US Patent 4283629, 1981.
- [4] J.P. Kruth, M. Bartscher, S. Carmignato, R. Schmitt, L. De Chiffre, A. Weckenmann, Computed tomography for dimensional metrology, *CIRP Annals - Manufacturing Technology*. 60 (2011) 821–842. <https://doi.org/10.1016/j.cirp.2011.05.006>.
- [5] L. De Chiffre, S. Carmignato, J.-P. Kruth, R. Schmitt, A. Weckenmann, Industrial applications of computed tomography, *CIRP Annals*. 63 (2014) 655–677. <https://doi.org/10.1016/j.cirp.2014.05.011>.
- [6] VDI/VDE 2630 Blatt 1.1:2016-11, Computertomografie in der dimensionellen Messtechnik - Grundlagen und Definitionen, (2016).
- [7] M. Bartscher, O. Sato, F. Härtig, U. Neuschaefer-Rube, Current state of standardization in the field of dimensional computed tomography, *Measurement Science and Technology*. 25 (2014) 064013. <https://doi.org/10.1088/0957-0233/25/6/064013>.
- [8] T. Pfeifer, *Fertigungsmeßtechnik*, 2nd ed., Oldenbourg Wissenschaftsverlag GmbH, München, 2001.
- [9] H. Kunzmann, T. Pfeifer, H. Schwenke, A. Weckenmann, Productive Metrology - Adding Value to Manufacture, *CIRP Annals - Manufacturing Technology*. 54 (2005) 155–168. [https://doi.org/10.1016/S0007-8506\(07\)60024-9](https://doi.org/10.1016/S0007-8506(07)60024-9).
- [10] M. Bartscher, U. Neuschaefer-Rube, F. Wäldele, Computed tomography - a highly potential tool for industrial quality control and production near measurement, in: *Proc. of 8th International Symposium on Measurement and Quality Control in Production*, Erlangen, DE, 2004: pp. 3–8.
- [11] U. Neuschaefer-Rube, M. Bartscher, F. Borges de Oliveira, J. Illeemann, T. Schönfeld, *Computertomographie für die industrielle Fertigungsmesstechnik*, Physikalisch-Technische Bundesanstalt, Braunschweig, Germany, 2016.
- [12] T.M. Buzug, *Computed Tomography*, Springer, 2008.
- [13] S. Carmignato, W. Dewulf, R. Leach (Eds.), *Industrial X-Ray Computed Tomography*, 1st ed., Springer International Publishing, 2018.
- [14] J. Illeemann, M. Bartscher, U. Neuschaefer-Rube, An efficient procedure for traceable dimensional measurements and the characterization of industrial CT systems, in:

- Digital Industrial Radiology and Computed Tomography (DIR 2015), Ghent, Belgium, 2015: p. 17.
- [15] M. Ferrucci, R.K. Leach, C. Giusca, S. Carmignato, W. Dewulf, Towards geometrical calibration of x-ray computed tomography systems—a review, *Meas. Sci. Technol.* 26 (2015) 092003. <https://doi.org/10.1088/0957-0233/26/9/092003>.
- [16] J. Hsieh, *Computed Tomography*, Wiley, 2009.
- [17] NIST, X-Ray Mass Attenuation Coefficients, NIST. (2009). <https://www.nist.gov/pml/x-ray-mass-attenuation-coefficients> (accessed December 15, 2019).
- [18] L.A. Feldkamp, L.C. Davis, J.W. Kress, Practical cone-beam algorithm, *Journal of the Optical Society of America A.* 1 (1984) 612–612. <https://doi.org/10.1364/JOSAA.1.000612>.
- [19] K. Fließner, *Computerized Tomography*, Bachelorarbeit, Karl-Franzens-Universität Graz, 2015.
- [20] K. Srinivasan, M. Mohammadi, J. Shepherd, Investigation of effect of reconstruction filters on cone-beam computed tomography image quality, *Australas Phys Eng Sci Med.* 37 (2014) 607–614. <https://doi.org/10.1007/s13246-014-0291-8>.
- [21] V. Camargo Nardelli, *Melhoria do desempenho metrológico da tomografia computadorizada por raios X por meio da seleção sistemática dos parâmetros de configuração*, PhD Thesis, Universidade Federal de Santa Catarina, 2012. <http://repositorio.ufsc.br/xmlui/handle/123456789/100861>.
- [22] J. Hiller, *Abschätzung von Unsicherheiten beim dimensionellen Messen mit industrieller Röntgen-Computertomographie durch Simulation*, PhD Thesis, Universität Freiburg, 2011.
- [23] B. Kratz, F. Herold, The influence of reconstruction methods on measurements in CT-volumes, (n.d.) 4.
- [24] C. Heinzl, *Analysis and Visualization of Industrial CT Data*, PhD Thesis, TU Wien, 2008. <http://pub-inf.tuwien.ac.at/showentry.php?ID=170137> (accessed November 11, 2013).
- [25] Y. Tan, W. Dewulf, K. Kiekens, Material Dependent Thresholding for Dimensional X-ray Computed Tomography, (n.d.) 8.
- [26] H. Lettenbauer, A. Lotze, S. Kunzmann, Method and Device for Identifying Material Boundaries of a Test Object, US Patent 8045806 B2, 2011. <http://www.google.com/patents/US8045806> (accessed December 14, 2015).
- [27] H. Steinbeiß, Verfahren und Vorrichtung zur Konturfeinermittlung eines Objekts bei bildgebenden Untersuchungsverfahren, European Patent 1861822B1, 2011. <https://patents.google.com/patent/EP1861822B1/de?q=Verfahren+und+Vorrichtung+zur+Konturfeinermittlung+eines+Objekts+bei+bildgebenden+Untersuchungsverfahren> (accessed December 15, 2019).
- [28] C. Reinhart, Industrial Computer Tomography - a Universal Inspection Tool, in: 17th World Conference on Nondestructive Testing, Shanghai, China, 2008: p. 10.
- [29] M. Pavan, T. Craeghs, R. Verhelst, O. Ducatteuw, J.-P. Kruth, W. Dewulf, CT-based quality control of Laser Sintering of Polymers | Elsevier Enhanced Reader, *Case Studies in Nondestructive Testing and Evaluation.* 6 (2016) 62–68. <https://doi.org/10.1016/j.csndt.2016.04.004>.

- [30] A. Thompson, I. Maskery, R.K. Leach, X-ray computed tomography for additive manufacturing: a review, *Measurement Science and Technology*. 27 (2016) 072001. <https://doi.org/10.1088/0957-0233/27/7/072001>.
- [31] M. Bartscher, U. Hilpert, J. Goebbels, G. Weidemann, Enhancement and Proof of Accuracy of Industrial Computed Tomography (CT) Measurements, *CIRP Annals - Manufacturing Technology*. 56 (2007) 495–498. <https://doi.org/10.1016/j.cirp.2007.05.118>.
- [32] J. Kastner, B. Plank, D. Salaberger, J. Sekelja, Defect and porosity determination of fibre reinforced polymers by X-ray computed tomography, in: *2nd International Symposium on NDT in Aerospace, 2010*: pp. 1–12. <http://www.ndt-aerospace.com/Portals/aerospace2010/BB/we1a2.pdf> (accessed April 8, 2016).
- [33] J. Weissenböck, M. Arikan, D. Salaberger, C. Heinzl, J. Kastner, Quantitative Messung und Visualisierung von Faserorientierungs- und Faserlängenverteilung von Glas-, Kohle- und Zellulosefaserverstärkten Kunststoffen mittels μ -Röntgen-Computertomografie, in: *DGZfP-Jahrestagung 2014, Potsdam, Germany, 2014*: p. 8.
- [34] P. Hermanek, S. Carmignato, Reference object for evaluating the accuracy of porosity measurements by X-ray computed tomography, *Case Studies in Nondestructive Testing and Evaluation*. 6 (2016) 122–127. <https://doi.org/10.1016/j.csndt.2016.05.003>.
- [35] L. Schild, M. Fülling, B. Häfner, G. Lanza, Uncertainty Evaluation of Pore Analysis for Additively Manufactured Parts using Cross Sections, in: *9th Conference on Industrial Computed Tomography, Padova, Italy, 2019*: p. 8.
- [36] F. Zanini, G. Gerardi, J. Weissenböck, C. Heinzl, J. Kastner, S. Carmignato, Experimental investigation on the accuracy of XCT measurement of fiber length in fiber reinforced polymers, in: *9th Conference on Industrial Computed Tomography, Padova, Italy, 2019*: p. 7.
- [37] BIPM, *Evaluation of Measurement Data—Guide to the expression of uncertainty in measurement*, 1995.
- [38] VDI/VDE 2630 Blatt 1.2:2018-06 *Computertomografie in der dimensionellen Messtechnik - Einflussgrößen auf das Messergebnis und Empfehlungen für dimensionelle Computertomografie-Messungen*, (n.d.). Verein Deutscher Ingenieure.
- [39] ISO 15530-3:2011, *Geometrical product specifications (GPS) — Coordinate measuring machines (CMM): Technique for determining the uncertainty of measurement — Part 3: Use of calibrated workpieces or measurement standards*, (2011).
- [40] H. Villarraga-Gómez, S.T. Smith, Uncertainty for uncorrected measurement results in X-ray computed tomography, in: *9th Conference on Industrial Computed Tomography, Padova, Italy, 2019*: p. 7.
- [41] VDI/VDE 2630 Blatt 2.1:2015-06, *Computertomografie in der dimensionellen Messtechnik - Bestimmung der Messunsicherheit und der Prüfprozesseignung von Koordinatenmessgeräten mit CT-Sensoren*, (2015).
- [42] ISO/TS 15530-4:2008, *Geometrical Product Specifications (GPS) — Coordinate measuring machines (CMM): Technique for determining the uncertainty of measurement — Part 4: Evaluating task-specific measurement uncertainty using simulation*, (2008).
- [43] C. Bellon, G.-R. Jaenisch, aRTist—analytical RT inspection simulation tool, in: *Proceedings in Int. Symposium on Digital Industrial Radiology and Computed*

- Tomography, Lyon, France, 2007: pp. 25–27. <http://ndt.net/article/dir2007/papers/s1.pdf> (accessed May 5, 2015).
- [44] M. Reiter, M. Erler, C. Kuhn, C. Gusenbauer, J. Kastner, SimCT: a simulation tool for X-ray imaging, in: Proc. 6th Conference on Industrial Computed Tomography (ICT), Wels, Austria, 2016: p. 7.
- [45] P. Wenig, S. Kasperl, Examination of the measurement uncertainty on dimensional measurements by X-ray computed tomography, in: Proc. of 9th European Conference on NDT, Berlin, Germany, 2006.
- [46] Durchstrahlungssimulation für die Messunsicherheitsbestimmung beim Messen geometrischer Merkmale mittels Röntgen-Computertomographie › Wipano - CTSimU, CTSimU Projekt. (n.d.). <https://www.ctsimu.forschung.fau.de/> (accessed December 16, 2019).
- [47] M. Flower, Webb’s Physics of Medical Imaging, Second Edition, 2nd ed., Hoboken: CRC Press, 2012., 2012.
- [48] M. Katic, D. Markucic, G. Barsic, Multi-spectral (W, Mo, Cu, and Ag) XCT measurements, in: 8th Conference on Industrial Computed Tomography, Wels, Austria, 2018: p. 5.
- [49] M. Reiter, F. Borges de Oliveira, M. Bartscher, C. Gusenbauer, J. Kastner, Case Study of Empirical Beam Hardening Correction Methods for Dimensional X-ray Computed Tomography Using a Dedicated Multi-material Reference Standard, Journal of Nondestructive Evaluation. 38 (2019). <https://doi.org/10.1007/s10921-018-0548-3>.
- [50] J. Illemann, M. Bartscher, X-ray spectrum dependence of the magnification of cone-beam CT, in: 7th Conference on Industrial Computed Tomography (ICT), Leuven, Belgium, 2017: p. 12.
- [51] J. Illemann, U. Neuschaefer-Rube, M. Bartscher, D. Bate, Determining spectrum-dependent source and detector positions in cone-beam CT, in: 8th Conference on Industrial Computed Tomography (ICT), Wels, Austria, 2018: p. 8.
- [52] F. Borges de Oliveira, M. Bartscher, U. Neuschaefer-Rube, R. Tutsch, J. Hiller, Multi-material Acceptance Testing for CT-Based Coordinate Measurement Systems, in: In: Majstorovic V., Durakbasa N. (Eds), Proceedings of the 12th International Conference on Measurement and Quality Control - Cyber Physical Issue. IMEKOTC14 2019. IMEKOTC14 2019, Springer, Cham, Belgrad, Serbia, 2019. https://doi.org/10.1007/978-3-030-18177-2_14.
- [53] J.J. Lifton, A.A. Malcolm, J.W. McBride, An experimental study on the influence of scatter and beam hardening in x-ray CT for dimensional metrology, Meas. Sci. Technol. 27 (2016) 015007. <https://doi.org/10.1088/0957-0233/27/1/015007>.
- [54] J.J. Lifton, S. Carmignato, Simulating the influence of scatter and beam hardening in dimensional computed tomography, Measurement Science and Technology. 28 (2017) 104001. <https://doi.org/10.1088/1361-6501/aa80b2>.
- [55] M. Bartscher, J. Illemann, U. Neuschaefer-Rube, ISO test survey on material influence in dimensional computed tomography, Case Studies in Nondestructive Testing and Evaluation. 6 (2016) 79–92. <https://doi.org/10.1016/j.csnadt.2016.04.001>.
- [56] F. Borges de Oliveira, A. Stolfi, M. Bartscher, M. Neugebauer, Creating a Multi-material Probing Error Test for the Acceptance Testing of Dimensional Computed Tomography Systems, in: 7th Conference on Industrial Computed Tomography (ICT), Leuven, Belgium, 2017: p. 8.

- [57] F. Borges de Oliveira, M. Bartscher, U. Neuschaefer-Rube, R. Tutsch, J. Hiller, Creating a Multi-Material Length Measurement Error Test for the Acceptance Testing of Dimensional Computed Tomography Systems, in: 7th Conference on Industrial Computed Tomography (ICT), Leuven, Belgium, 2017: p. 12.
- [58] W. Cao, R. Pauwels, G. Fardell, B. Price, W. Dewulf, Influencing factors in x-ray spectral estimation of industrial CT using transmission measurements, in: ICT 2019, Padova, Italy, 2019: p. 7.
- [59] A. Jansson, J. Ekengren, A.-R. Zekavat, L. Pejryd, Effects of X-ray Penetration Depth on Multi Material Computed Tomography Measurements, in: Proc. of 6th Conference on Industrial Computed Tomography (ICT) 2016, Wels, Austria, 2016: p. 8.
- [60] R. Schmitt, A. Buratti, N. Grozmani, C. Voigtmann, M. Peterek, Model-based optimisation of CT imaging parameters for dimensional measurements on multimaterial workpieces, *CIRP Annals - Manufacturing Technology*. 67 (2018) 527–530. <https://doi.org/10.1016/j.cirp.2018.04.003>.
- [61] C. Heinzl, J. Kastner, T. Möller, E. Gröller, Statistical analysis of Multi-Material Components using Dual Energy CT, in: Proceedings of Vision, Modeling and Visualization, 2008. <http://www.cg.tuwien.ac.at/research/publications/2008/heinzl-2008-sam/>.
- [62] M. Krumm, S. Kasperl, M. Franz, Beam Hardening Correction of Multi-Material Objects, in: Proc. of 10th European Conference on Non-Destructive Testing, Moscow, Russia, 2010: p. 7.
- [63] A. Amirkhanov, M. Reiter, J. Kastner, E. Gröller, C. Heinzl, Evaluation of Projection-Based Metal-Artifact Reduction for Multi-Material Components, in: 4th Conference on Industrial Computed Tomography (ICT), Wels, Austria, 2012: p. 9.
- [64] B. Kratz, F. Herold, M. Kurfiß, T.M. Buzug, Metal Artifact Reduction for Multi-Material Objects, in: Proc. of 5th Conference on Industrial Computed Tomography (ICT) 2014, Wels, Austria, 2014: p. 8.
- [65] J.J. Lifton, Multi-material linearization beam hardening correction for computed tomography, *XST*. 25 (2017) 629–640. <https://doi.org/10.3233/XST-16197>.
- [66] G. Herl, S. Rettenberger, J. Hiller, T. Sauer, Metal artifact reduction by fusion of CT-scans from different positions using the unfiltered backprojection, in: 8th Conference on Industrial Computed Tomography (ICT) 2018, Wels, Austria, 2018: p. 8.
- [67] F. Borges de Oliveira, A. Stolfi, M. Bartscher, L. De Chiffre, U. Neuschaefer-Rube, Experimental investigation of surface determination process on multi-material components for dimensional computed tomography, *Case Studies in Nondestructive Testing and Evaluation*. 6 (2016) 93–103. <https://doi.org/10.1016/j.csndt.2016.04.003>.
- [68] C. Heinzl, J. Kastner, B. Georgi, H. Lettenbauer, Comparison of surface detection methods to evaluate cone beam computed tomography data for three dimensional metrology, in: 2007: pp. 25–27. <http://www.ndt.net/article/dir2007/papers/p4.pdf> (accessed July 3, 2014).
- [69] C. Heinzl, J. Kastner, E. Gröller, Surface Extraction from Multi-Material Components for Metrology using Dual Energy CT, *IEEE Transactions on Visualization and Computer Graphics*. 13 (2007) 1520–1527. <https://doi.org/10.1109/TVCG.2007.70598>.
- [70] T. Fujimori, H. Suzuki, Surface Extraction from Multi-material CT Data, in: Ninth International Conference on Computer Aided Design and Computer Graphics (CAD-

- CG'05), IEEE, Hong Kong, China, 2005: pp. 319–324. <https://doi.org/10.1109/CAD-CG.2005.79>.
- [71] M. Haitham Shammaa, Y. Ohtake, H. Suzuki, Segmentation of multi-material CT data of mechanical parts for extracting boundary surfaces, *Computer-Aided Design*. 42 (2010) 118–128. <https://doi.org/10.1016/j.cad.2009.08.003>.
- [72] ISO 10360-2:2009, Geometrical product specifications (GPS) — Acceptance and reverification tests for coordinate measuring machines (CMM) — Part 2: CMMs used for measuring linear dimensions, (2009).
- [73] ISO 10360-8:2013, Geometrical product specifications (GPS) -- Acceptance and reverification tests for coordinate measuring systems (CMS) -- Part 8: CMMs with optical distance sensors, (2013).
- [74] ISO 10360-10:2016, Geometrical product specifications (GPS) — Acceptance and reverification tests for coordinate measuring systems (CMS) — Part 10: Laser trackers for measuring point-to-point distances, (2016).
- [75] J. Illeemann, M. Bartscher, O. Jusko, F. Härtig, U. Neuschaefer-Rube, K. Wendt, Procedure and reference standard to determine the structural resolution in coordinate metrology, *Measurement Science and Technology*. 25 (2014) 064015. <https://doi.org/10.1088/0957-0233/25/6/064015>.
- [76] F.A. Arenhart, V.C. Nardelli, G.D. Donatelli, Characterization of the Metrological Structural Resolution of CT Systems using a Multi-Wave Standard, in: *Proc. of XXI IMEKO World Congress*, 2015.
- [77] M. Fleßner, N. Vujaklija, E. Helmecke, T. Hausotte, Determination of metrological structural resolution of a CT system using the frequency response on surface structures, in: *MacroScale*, Vienna, Austria, 2014.
- [78] S. Carmignato, A. Pierobon, P. Rampazzo, M. Parisatto, E. Savio, CT for Industrial Metrology – Accuracy and Structural Resolution of CT Dimensional Measurements, in: *Conf. on Industrial Computed Tomography (ICT 2012)*, 2012.
- [79] F. Zanini, S. Carmignato, Two-spheres method for evaluating the metrological structural resolution in dimensional computed tomography, *Measurement Science and Technology*. 28 (2017) 114002. <https://doi.org/10.1088/1361-6501/aa85b7>.
- [80] VDI/VDE 2630 Blatt 1.3, VDI/VDE 2617 Blatt 13: Genauigkeit von Koordinatenmessgeräten - Kenngrößen und deren Prüfung - Leitfaden zur Anwendung von DIN EN ISO 10360 für Koordinatenmessgeräte mit CT-Sensoren; VDI/VDE 2630 Blatt 1.3: Computertomografie in der dimensionellen Messtechnik - Leitfaden zur Anwendung von DIN EN ISO 10360 für Koordinatenmessgeräte mit CT-Sensoren, (2011).
- [81] F. Borges de Oliveira, M. Bartscher, U. Neuschaefer-Rube, Analysis of Combined Probing Measurement Error and Length Measurement Error Test for Acceptance Testing in Dimensional Computed Tomography, in: *Proc. of Digital Industrial Radiology and Computed Tomography (DIR 2015)*, Ghent, Belgium, 2015: p. 12.
- [82] Trapet Precision Engineering, Ball rail, (n.d.). <https://trapet.de/> (accessed January 28, 2020).
- [83] M. Neugebauer, U. Hilpert, M. Bartscher, N. Gerwien, S. Kunz, F. Neumann, J. Goebels, G. Weidemann, Ein geometrisches Normal zur Prüfung von Röntgen-Mikro-Computertomografiemesssystemen (A Geometrical Standard for Testing of X-Ray Computer Tomography), *tm - Technisches Messen*. 74 (2007). <https://doi.org/10.1524/teme.2007.74.11.565>.

- [84] P. Müller, J. Hiller, A. Cantatore, G. Tosello, New reference object for metrological performance testing of industrial CT systems, in: 12th Euspen International Conference, Stockholm, 2012: p. 4.
- [85] A. Cantatore, J.L. Andreasen, S. Carmignato, P. Müller, Verification of a CT scanner using a miniature step gauge, in: 11th International Conference of the European Society For Precision Engineering & Nano Technology Euspen, Como, IT, 2011: p. 4.
- [86] M. Bartscher, M. Neukamm, M. Krystek, Method for a Traceable Geometry Assessment of Arbitrarily Shaped Sculptured Surfaces, in: 10th International Symposium on Measurement and Quality Control, 2010.
- [87] S. Carmignato, D. Dreossi, L. Mancini, F. Marinello, G. Tromba, E. Savio, Testing of x-ray microtomography systems using a traceable geometrical standard, *Measurement Science and Technology*. 20 (2009) 084021. <https://doi.org/10.1088/0957-0233/20/8/084021>.
- [88] J. Angel, L. De Chiffre, J.P. Kruth, Y. Tan, W. Dewulf, Performance evaluation of CT measurements made on step gauges using statistical methodologies, *CIRP Journal of Manufacturing Science and Technology*. 11 (2015) 68–72. <https://doi.org/10.1016/j.cirpj.2015.08.002>.
- [89] F. Léonard, S.B. Brown, P.J. Withers, P.M. Mummery, M.B. McCarthy, A new method of performance verification for x-ray computed tomography measurements, *Measurement Science and Technology*. 25 (2014) 065401. <https://doi.org/10.1088/0957-0233/25/6/065401>.
- [90] J. Hiller, S. Kasperl, T. Schön, S. Schröpfer, D. Weiss, Comparison of Probing Error in Dimensional Measurement by Means of 3D Computed Tomography with Circular and Helical Sampling, in: 2nd International Symposium on NDT in Aerospace 2010, Hamburg, Germany, 2010: p. 7.
- [91] Y. Shi, S. Gao, X. Song, D. Li, W. Li, Q. Li, S. Li, S. Chen, The assessment of industrial CT's probing error, in: *Optical Metrology and Inspection for Industrial Applications III*, International Society for Optics and Photonics, 2014: p. 92760T. <https://doi.org/10.1117/12.2071795>.
- [92] J.L. Andreasen, F. Montanari, L. De Chiffre, On the impact of probing form error on form measurement in Computed Tomography, in: *Proc. of 9th Conference on Industrial Computed Tomography (ICT) 2019*, Padova, Italy, 2019: p. 6.
- [93] ISO 14253-1:2017, Geometrical product specifications (GPS) — Inspection by measurement of workpieces and measuring equipment — Part 1: Decision rules for verifying conformity or nonconformity with specifications, (2017).
- [94] ISO 14253-5:2015, Geometrical product specifications (GPS) — Inspection by measurement of workpieces and measuring equipment — Part 5: Uncertainty in verification testing of indicating measuring instruments, (2015).
- [95] ISO/TS 17865:2016, Geometrical product specifications (GPS) — Guidelines for the evaluation of coordinate measuring machine (CMM) test uncertainty for CMMs using single and multiple stylus contacting probing systems, (2016).
- [96] ISO/TS 23165:2006, Geometrical product specifications (GPS) — Guidelines for the evaluation of coordinate measuring machine (CMM) test uncertainty, (2006).
- [97] ISO 10360-5:2010, Geometrical product specifications (GPS) — Acceptance and reverification tests for coordinate measuring machines (CMM) — Part 5: CMMs using single and multiple stylus contacting probing systems, (2010).

- [98] Optisches Glas, Wikipedia. (2019). https://de.wikipedia.org/w/index.php?title=Optisches_Glas&oldid=186285579 (accessed November 11, 2019).
- [99] AMCO Metall-Service GmbH, Technisches Datenblatt EN AW-5083 (AlMg4,4Mn), (n.d.).
- [100] VSMPO-AVISMA Corporation, Inspection certification of Ti6Al4V, (2007).
- [101] Ingenieur-Unternehmen für Energie- und Umwelttechnik, Cestic Datenblatt - Typ HB, (2016).
- [102] GOM Inspect | 3D-Messdaten Auswertesoftware | GOM, (n.d.). <https://www.gom.com/de/3d-software/gom-inspect.html> (accessed January 20, 2020).
- [103] C. Bellon, A. Deresch, C. Gollwitzer, G.-R. Jaenisch, Radiographic Simulator aRTist: Version 2, in: Proc. of 18th World Conference on Nondestructive Testing, Durban, South Africa, 2012. http://www.ndt.net/article/wcndt2012/papers/333_wcndtfinal00333.pdf (accessed June 16, 2015).
- [104] VDI/VDE/DGQ 2618 Blatt 1.2:2003-12, Prüfmittelüberwachung - Anweisungen zur Überwachung von Messmitteln für geometrische Größen - Messunsicherheit, (2003).
- [105] M. Krystek, Berechnung der Messunsicherheit: Grundlagen und Anleitung für die praktische Anwendung, 1. Aufl, Beuth, Berlin, 2012.
- [106] B.L. Welch, The Generalization of 'Student's' Problem when Several Different Population Variances are Involved, Biometrika. 34 (1947) 28–35. <https://doi.org/10.2307/2332510>.
- [107] F.E. Boas, D. Fleischmann, CT artifacts: causes and reduction techniques, Imaging in Medicine. 4 (2012) 229–240.
- [108] U. Zscherpel, K. Osterloh, U. Ewert, Unsharpness characteristics of digital detectors for industrial radiographic imaging, in: Proceedings BB 84-CD, Mainz, Germany, 2003: p. 11.
- [109] MathWorks, Box plots, MATLAB. (n.d.). https://www.mathworks.com/help/stats/box-plots.html?searchHighlight=box%20plots&cs_tid=doc_srchtile (accessed January 19, 2020).
- [110] J. Starman, Lag correction in amorphous silicon flat-panel X-ray computed tomography, PhD Thesis, STANFORD UNIVERSITY, 2010.

Contributions

Book chapter

- [1] S. Carmignato, W. Dewulf, R. Leach, Industrial X-Ray Computed Tomography, 1st ed., Springer International Publishing, 2018.

Poster

- [2] U. Neuschaefer-Rube, M. Bartscher, F. Borges de Oliveira, J. Illemann, T. Schönfeld, Computertomographie für die industrielle Fertigungsmesstechnik, Physikalisch-Technische Bundesanstalt, Braunschweig, Germany, 2016.
- [3] J. Wilbig, F. Borges de Oliveira, M. Schwentenwein, J. Günster, Quality Aspects of Additively Manufactured Medical Implants - Defect Detection in Lattice Parts, yCAM Forum, Mons, Belgium, 2019.

Conference papers with talk

- [4] F. Borges de Oliveira (speaker), M. Bartscher, U. Neuschaefer-Rube, R. Tutsch, J. Hiller, Multi-material Acceptance Testing for CT-Based Coordinate Measurement Systems, in: In: Majstorovic V., Durakbasa N. (Eds), Proceedings of the 12th International Conference on Measurement and Quality Control - Cyber Physical Issue. IMEKOTC14 2019. IMEKOTC14 2019, Springer, Cham, Belgrad, Serbia, 2019. https://doi.org/10.1007/978-3-030-18177-2_14.
- [5] F. Borges de Oliveira (speaker), A. Stolfi, M. Bartscher, M. Neugebauer, Creating a Multi-material Probing Error Test for the Acceptance Testing of Dimensional Computed Tomography Systems, in: Proc. 7th Conference on Industrial Computed Tomography (iCT) 2017, Belgium, 2017: p. 8.
- [6] F. Borges de Oliveira (speaker), M. Bartscher, U. Neuschaefer-Rube, Analysis of Combined Probing Measurement Error and Length Measurement Error Test for Acceptance Testing in Dimensional Computed Tomography, in: DIR 2015, Ghent, Belgium, 2015: p. 12.
- [7] Hermanek, Petr (speaker); Borges de Oliveira, Fabrício; Carmignato, Simone; Bartscher, Markus; Savio, Enrico: Experimental investigation on multi-material gap measurements by computed tomography using a dedicated reference standard.; Conference Proceedings euspen's 17th International Conference & Exhibition, Hannover, 29, May - 02, June, 2017
- [8] Hermanek, Petr (speaker); Borges de Oliveira, Fabrício; Carmignato, Simone; Bartscher, Markus: Experimental investigation of new multi-material gap reference standard for testing computed tomography systems. Proc. 7th Conference on Industrial Computed Tomography (iCT) 2017 Leuven, Belgium, 2017

Conference paper with poster

- [9] F. Borges de Oliveira, M. Bartscher, U. Neuschaefer-Rube, R. Tutsch, J. Hiller, Creating a Multi-Material Length Measurement Error Test for the Acceptance Testing of Dimensional Computed Tomography Systems, in: Proc. 7th Conference on Industrial Computed Tomography (iCT) 2017 Leuven, Belgium, 2017: p. 12.

Conference papers in Journal with conference talk

- [10] F. Borges de Oliveira (speaker), A. Stolfi, M. Bartscher, L. De Chiffre, U. Neuschaefer-Rube, Experimental investigation of surface determination process on multi-material components for dimensional computed tomography, Case Studies in Nondestructive Testing and Evaluation. 6 (2016) 93–103. <https://doi.org/10.1016/j.csndt.2016.04.003>. Talk in the iCT 2016, Wels, Austria
- [11] M. Reiter (speaker), F. Borges de Oliveira, M. Bartscher, C. Gusenbauer, J. Kastner, Case Study of Empirical Beam Hardening Correction Methods for Dimensional X-ray Computed Tomography Using a Dedicated Multi-material Reference Standard, Journal of Nondestructive Evaluation. 38 (2019). <https://doi.org/10.1007/s10921-018-0548-3>. 8th Conference on Industrial Computed Tomography, iCT Conference 2018, Wels, 06-09, February 2018, Austria
- [12] F. Borges de Oliveira, de Campos Porath M (speaker), Camargo Nardelli V, Arenhart FA, Donatelli GD (2014) Characterization and Correction of Geometric Errors Induced by Thermal Drift in CT Measurements. Key Engineering Materials 613:327–334.

Invited talks

- [13] F. Borges de Oliveira (speaker), M. Bartscher, U. Neuschaefer-Rube, R. Tutsch, J. Hiller, Multi-material Acceptance Testing for Computed Tomography-based Coordinate Measurement systems. 7th CIA-CT Conference on “Industrial Applications of Computed Tomography”, 13, June 2019, Denmark.
- [14] M. Bartscher (speaker), F. Borges de Oliveira, Towards accepted acceptance testing for dimensional CT. 5th CIA-CT Conference on “Industrial Applications of Computed Tomography”, 18, June 2015, Denmark.
- [15] U. Neuschaefer-Rube (speaker), M. Bartscher, J. Illeemann, F. Borges de Oliveira, Challenges of full 3D measurement of AM parts applying computed tomography (CT), Keynote talk in Euspen Special Interest Group Meeting: Additive Manufacturing, 10-11, October 2017, Leuven Belgium.

Scientific newsletter

- [16] F. Borges de Oliveira, U. Neuschaefer-Rube, Are implants made of 3D printer good enough? PTB News 3/2019, English edition, Issue Dezember 2019, ISSN 1611-163X

Acronyms

2D	Two-dimensional
3D	Three-dimensional
ART	Algebraic reconstruction techniques
ASTM	American society for testing and materials
BAM	Bundesanstalt für Materialforschung und - prüfung
BHC	Beam hardening correction
CAD	Computer-aided design
Cesic	Carbon fibre reinforced silicon carbide
CFRP	Carbon fibre reinforced polymer
CMM	coordinate measuring machine
CMM	coordinate measuring machine
CMS	Coordinate measurement system
CT	X-ray computed tomography
CT-based CMS	Computed tomography-based coordinate measurement system
CTE	Coefficient of thermal expansion
DQE	Detector's quantum efficiency
EDM	electrical discharge machining
<i>E-test</i>	Length measurement error
FBP	Filtered back-projection
FDK	Reconstruction algorithm: Feldkamp Davis and Kress
GUM	Guide to expression of uncertainty in measurement
HAM	High absorbing material
HS	Half sphere
IQR	Inter-quartile range
ISO	TC213 WG 10 International organisation for standardisation, technical committee 213 working group 10
ISO	International organisation for standardisation
ISO/TS	Technical specification
KMS	Koordinatenmesssystem
LAM	Low absorbing material
LSC	Least-squares method
MoMat	Mono-material
MPE	Maximum permissible error
MuMat	Multi-material
MuMat-HC	Multi-material hole cube standard
NDT	Non-destructive testing
PTB	Physikalisch-Technische Bundesanstalt
<i>P-test</i>	Probing error test
Q	Quartile

ROI	Region of interest
SDD	Source-detector distance
SI-unit	International system of units
SNR	Signal-to-noise-ratio
SRD	Source-rotary axis distance
THz	Terahertz
THz-CT	Terahertz computed tomography
VDI/VDE	Verein Deutscher Ingenieure
Voxel	Volumetric pixel
WP	Workpiece

List of symbols

§	Section, chapter or sub-chapter
η	Small length of the spatially varying attenuation representing material non-homogeneity
μ	X-ray attenuation coefficient
Ag	Silver
Al	Aluminium
Al₂O₃	Aluminium oxide
Al₂O₃:Cr	Ruby
CsI	caesium iodide
Cu	Copper
Dr_x	Misalignment of the detector around x-axis
Dr_y	Misalignment of the detector around y-axis
Dr_z	Misalignment of the detector around z-axis
e	Euler's number
E	X-ray energy
e^-	Electrons
$E_{Bi::CT}$	Bidirectional length measurement error
$E_{Bi:MuMa::CT}$	Multi-material bidirectional length measurement error
E_{max}	Maximum spectral energy
$E_{MuMa::CT}$	Measured multi-material length measurement error
$E_{MuMa::CT,MPE}$	Multi-material length measurement maximum permissible error
$E_{MVol::CT}$	Volumetric length measurement error
$E_{MVol:MuMa:Avg::CT}$	Multi-material volumetric length measurement error
$E_{Uni::CT}$	Unidirectional length measurement error
Fe	Iron
Gd₂O₂S	gadolinium oxysulphide
I	Transmitted intensity
I_0	Incident intensity
k	Coverage factor
$L_A + L_B$	Maximum total thickness
Mo	Molybdenum
mx, my and mz	Surface normal vector
N_I	Number of repetitions of sample 1
\emptyset	Diameter
PEEK	Polyether ether ketone
PF25	Simplification of $P_{Form.Sph.1x25::CT}$
PF95	Simplification of $P_{Form.MuMa.Sph.D95%::CT}$
$P_{Form.MuMa.Sph.1x25::CT}$	Multi-material probing form error
$P_{Form.MuMa.Sph.D95%::CT}$	Multi-material probing dispersion error

$P_{\text{Form.Sph.1x25::CT}}$	Probing error form
$P_{\text{Form.Sph.D95%::CT}}$	Probing dispersion error
$P_{\text{MuMa::CT}}$	Measured multi-material probing error
$P_{\text{MuMa::CT,MPE}}$	Multi-material probing error maximum permissible error
PS25	Simplification of $P_{\text{Size.MuMa.Sph.1x25::CT}}$
Psall	Simplification of $P_{\text{Size.MuMa.Sph.All::CT}}$
$P_{\text{Size.MuMa.Sph.1x25::CT}}$	Multi-material probing size error
$P_{\text{Size.MuMa.Sph.All::CT}}$	Multi-material probing size error All
$P_{\text{Size.Sph.1x25::CT}}$	Probing size error
$P_{\text{Size.Sph.All::CT}}$	Probing error size All
R	Thickness ratio
Rrx	Rotation axis around x-axis
Rry	Rotation axis around y-axis
Rrz	Rotation axis around z-axis
s_1	Standard deviation of sample 1
Si₃N₄	Silicon nitride
Ti	Titanium
t_W	Welch's number
U	Expanded measurement uncertainty
U_{Test}	Test value uncertainty
v	Degrees of freedom
W	Tungsten
Z	atomic number
ZrO₂	Zirconia oxide
α	Reliability factor
$\Delta I/I$	Change in intensity between incoming and transmitted beam
Δx	Variation of the material thickness
λ	Wavelength
ρ	Material density
x	Material thickness
Θ	Sphericity
$R_{\mu A/\mu B}$	Attenuation coefficient ratio between materials B and A
$\bar{\mu}_{\mu A \& \mu B}$	Attenuation coefficient average between materials A and B
\bar{X}_1	Statistical average of sample 1

Acknowledgements

This work was carried out during my time as research associate at the department 5.3 Coordinate Metrology of the *Physikalisch-Technische Bundesanstalt* (PTB), Braunschweig, Germany. Also, this work was reviewed and accepted as doctorate thesis for obtaining the title of *Doktor-Ingenieur* (Dr.-Ing.) in the Faculty of Mechanical Engineering of the *Technische Universität Carolo-Wilhelmina zu Braunschweig* (TUBS), Germany.

Throughout the development of this thesis, I was lucky enough to be surrounded by supportive as well as knowledgeable people to whom I would like to express my genuine gratitude. First, I would like to thank Prof. Dr.-Ing. Rainer Tutsch, head of the *Institut für Produktionsmesstechnik* (IPROM) of TUBS, for accepting to be my doctorate supervisor and for providing guidance as well as valuable input for the development of this thesis.

Likewise, my sincere appreciation goes to Prof. Dr.-Ing. Jochen Hiller, leader of the *Anwendungszentrum CT in der Messtechnik* of the *Entwicklungszentrum Röntgentechnik* (EZRT) part of the Fraunhofer group and Professor in the Faculty of Mechanical Engineering and Mechatronics of the *Technische Hochschule Deggendorf*, Deggendorf, Germany, for accepting to accompany me as second supervisor, for the willingness to travel several times to meet and for providing technical guidance and support.

Very special thanks go to Dr.-Ing. Habil. Ulrich Neuschaefer-Rube, leader of the Working Group 5.34 Multisensor Metrology of PTB, and Dr. Markus Bartscher, senior researcher in the same Working Group, for the mentoring, revision of this monography and for all the years of support and guidance.

I would like to express my acknowledgement to all the colleagues from department 5.3 Coordinate Metrology of PTB, who directly or indirectly contributed for the finalization of this work, for the extraordinary teamwork and assistance throughout these years. Specially, my sincere appreciation goes to Helge Reimann for the tactile measurements of the cubes; Dr. Michael Neugebauer for the discussions about measurements on the standards and for the measurements on the spheres; Dieter Schulz for the assistance with the standards and willingness to help; Astrid Linkogel for the optical measurements of the standards; Karsten Kusch for gluing the half spheres; René Laquai for taking over part of my project activities, towards the end of this thesis, so that I could spend more time writing it; Olga Kazankova and Dr. Christian Rothleitner, with whom I shared office for a long time, I would like to thank for the work-related discussions as well as distraction moments.

I would like to express my gratitude to Josef Frese for taking the time to revise and provide valuable linguistic as well as technical feedback to this work.

Special thanks also go to Dr. Jens Illemann for the discussions throughout the development of this work.

I would like to thank Dr. -Ing. Karin Kniel, head of the department 5.3 of PTB, for taking the time for discussions and for the support specially in crucial phases.

Many thanks to the colleagues from Department 5.5 Scientific Instrumentation of PTB, Dr. -Ing. Rudolf Meeß and Christian Wolpert for the discussions and manufacturing of the multi-material standards.

I would like also to thank my dear friend Francisco Arenhart for the important input specially in the writing phase of this thesis.

Last, but not least, I would like to thank my life partner for the patience and for holding my back during this time; and my dear family, whose unconditional support and love crosses not only borders but an entire ocean.



Herausgeber:

Physikalisch-Technische Bundesanstalt
ISNI: 0000 0001 2186 1887

Presse und Öffentlichkeitsarbeit

Bundesallee 100
38116 Braunschweig

Telefon: (05 31) 592-93 21
Telefax: (05 31) 592-92 92
www.ptb.de

Vertrieb:

Fachverlag NW in der
Carl Schünemann Verlag GmbH

Zweite Schlachtpforte 7
28195 Bremen

Telefon: (04 21) 369 03-0
Telefax: (04 21) 369 03-63
www.schuenemann-verlag.de